# MICRO-SCALE TURBOPUMP BLADE CAVITATION

by

SUMITA PENNATHUR

B.S. Aerospace and Aeronautics
Massachusetts Institute of Technology, 2000

Submitted to the Department of Aeronautics and Astronautics
in partial fulfillment of the requirements for the degree of

**MASTER OF SCIENCE IN AERONAUTICS AND ASTRONAUTICS**

at the

**MASSACHUSETTS INSTITUTE OF TECHNOLOGY**

June 2001



Author: _____

Sumita Pennathur
Department of Aeronautics and Astronautics
June 1, 2001

Certified by: _____

Professor Alan H. Epstein
R.C. Maclaurin Professor of Aeronautics and Astronautics
Thesis Supervisor

Accepted by: _____

Professor Wallace E. Vander Velde
Professor of Aeronautics and Astronautics
Chair, Committee on Graduate Students

# MICRO-SCALE TURBOPUMP BLADE CAVITATION

by

Sumita Pennathur

Submitted to the Department of Aeronautics and Astronautics
on May 14, 2001 in Partial Fulfillment of the
Requirements for the Degree of Master of Science in
Aeronautics and Astronautics

## ABSTRACT

The possibility of a silicon micro-fabricated turbopump for the use in a micro-fabricated bipropellant liquid rocket engine is of interest. Such a pump might have airfoils on the order of 1mm chord and 0.2mm span and operate at a Reynolds number of 6000. Cavitation is a major technical issue in such a pump, but there is little work in the literature at this length scale. This work documents analytical and experimental investigations of cavitation on millimeter long pump blading. Cavitation inception and bubble growth are analyzed on a micro-scale and deviations from macro-scale theory are discussed. The analysis suggests that residence time, surface roughness, surface tension, and passage area constraints are significant factors in cavitation inception and growth.

A non-rotating microfabricated cascade has been designed, fabricated, and tested to quantify the behavior of micro-scale cavitation. An experimental rig has been constructed, and 18 micro-cascades have been tested. Visual observations confirm the existence of cavitation, and illustrate the phenomena of hysteresis and time lag. Comparisons of test results with analysis indicate that cavitation inception is adequately modeled by macro-scale theory. Test repeatability is established and the experimental data is found to be in agreement with 3D numerical results. Performance impacts of cavitation on micro-scale bade rows are discussed and several useful correlations are included. No apparent surface damage has been observed in these experiments.

The experimental and analytical results are compiled in the form of design criteria for micro-scale turbopumps, and are used to evaluate the performance impacts due to cavitation. It is estimated that for a micro-turbopump operating at the most severe expected cavitating conditions, the performance loss in terms of pressure recovery is not greater than 20%.

Thesis Supervisor: Professor Alan H. Epstein
Title: R.C. Maclaurin Professor of Aeronautics and Astronautics

# ACKNOWLEDGEMENTS

I would first like to thank my thesis advisor, Professor Alan Epstein, for his leadership, guidance, support, and encouragement throughout my academic career which was invaluable to my learning experience. Prof. J. L. Kerrrebrock's discussions and guidance were also very helpful. I admire their dedication not only to my research work, but also to furthering my education and well-being.

Dr. Yoav Peles and Arturo Ayon were integral in making my experimental cascades. Thanks especially to Yoav for teaching me so much about microfabrication during the second build and keeping me company during those long clean room hours. Thanks to the rest of the microfabrication people, especially Tom Takas, Xin Zhang and Dennis Ward for their knowledge and good humor at the MTL. James Letendre and Viktor Dubrowski deserve a huge amount of credit for building the experimental apparatus and machining the packaging for my experiment. Also thanks to Bill Ames, Diana Park, Paul Warren, and Holly Anderson for dealing with all the little details I would come to them with. And a special thanks to Lori Martinez, who always listened to my personal problems, no matter how insignificant, and for making sure I ate well enough to remain on this planet!

Adam London and Chris Protz helped me stay afloat when I was first started the project, and I would like to thank them for their constant advice and assistance during my work on this project. I am also grateful to the remainder of the microrocket research team, Antoine Deux, Laurent Jamonet, Carole Joppin, and Erin Noonan. Thanks especially to Antoine and Laurent, without whom I would have never learned so much French!

I would like to thank the students at the GTL who I had a great time working with while I was here. I would especially like to thank Spad, Dan, Beilene, Tony, and Raffi for all the great times we had, and all the help and support they gave me the last year.

I would like to thank all the friends I made at MIT, and also all my friends at home in Foxboro for all the outside support and not forgetting about me when I went into hibernation to work.

Most of all I would like to thank my entire family. I am so proud to be a member of such a strong, loving family who has given me so much love and support throughout my lifetime. Thanks to Mom and Dad and Satishanna especially, I owe them many of my accomplishments.

An NDSEG Fellowship from the US Army, DARPA and the Army Research Office supported this work. Their support is gratefully acknowledged.

# TABLE OF CONTENTS

# LIST OF TABLES

# LIST OF FIGURES

# NOMENCLATURE

**ROMAN:**

| | |
|---|---|
| c | Chord |
| $c_p$ | Specific heat at constant pressure |
| D | Diameter |
| ds | Differential length along curve |
| L | Length |
| M | Mach number |
| $\dot{m}$ | Mass flow rate |
| P | Pressure |
| R | Universal Gas Constant |
| r | Radius |
| T | Temperature |
| t | Time |
| $U$ | Velocity |
| $u$ | Time average x component of velocity |

**PARAMETERS:**

| | |
|---|---|
| Re | Reynolds Number, $\rho uA/\mu$ |
| $\sigma$ | Cavitation number, $2(p-p_v)/(\rho U^2)$ |
| $C_p$ | Coefficient of Pressure, $2(p-p_\infty)/(\rho U^2)$ |

**GREEK:**

| | |
|---|---|
| $\beta$ | Flow Angle |
| $\Delta$ | Change in a quantity |
| $\mu$ | Coefficient of thermal viscosity |
| $\pi$ | Pressure Ratio |
| $\rho$ | Density |
| $\tau$ | Characteristic time scale |
| $\omega r$ | Tangential velocity of rotor |

**SUBSCRIPTS:**

| | |
|---|---|
| max | Maximum |
| min | Minimum |
| o | Stagnation |
| r | Radial |
| T | Total |
| t | tangential |
| x | In x-direction |
| y | In y-direction |
| z | In z-direction |

**ACRONYMS:**

| | |
|---|---|
| MEMS | Micro-Electro-Mechanical Systems |
| DRIE | Deep Reactive Ion Etching |
| STS | Surface Technology Systems |
| TMDE | Time-Multiplexed Deep Etching |
| SEM | Scanning Electron Microscope |

# 1 INTRODUCTION

## 1.1 BACKGROUND AND MOTIVATION

Micro-fabricated gas turbine engines have been under development at MIT during the past 5 years [12] for propulsion and electric power applications. Recent efforts to develop a microturbocharger and microcompressor have produced small silicon structures, approximately 20mm square by 4mm deep, which have the potential to produce about 10-50W of useful power. The existence of these structures suggests the potential of liquid high-pressure microturbopumps applicable to small liquid propellant rocket engines.

The use of a microrocket engine with integrated microturbopumps would eliminate the need for high pressure tanks that current small rocket thrusters use to feed the propellants into the combustion chamber. Low pressure propellant tanks reduce structural tank mass which would benefit satellite buses by providing greater payload capacity or an equivalent increase in propellant mass for a longer life in orbit. Additionally, the turbopumps should be capable of producing higher chamber pressures, so that microrocket engines may be made smaller for a given thrust level.

The complete microrocket engine would be able to deliver a thrust to weight ratio that surpasses current rocket engines by up to two orders of magnitude, since as the size is reduced the thrust of the engine decreases with the area of the nozzle exit (characteristic length squared), while the mass of the engine decreases with volume (characteristic length cubed)[1]. Increasing this ratio leads to a decrease in overall system weight, which means that more payload can be delivered at the same cost of propellants and overall mass. Also, because of their low engine weight, microrocket engines can be used redundantly and lead to more reliability, since vehicle control can be maintained even with one engine failure. The use of silicon microfabrication techniques for the rocket engines also may lead to

[1] See [7] for more details.

a decrease in cost of production, since several engines can be produced at once without a proportional increase in cost.

The main applications investigated for these devices include both satellite attitude control and orbital maneuvers [13] and very small launch vehicles [14]. The significant weight savings of the microrocket engine should allow them to be useful for impulsive orbit maintenance and control, such as orbit transfer, since transfer times would be significantly less than those envisioned for electric propulsion. Microrocket engines are also being investigated as the sole propulsion system for very small launch vehicles, since they can provide the high performance and low mass necessary for orbital insertion at this small scale.

## 1.2 MICROROCKET ENGINE CONCEPT

The complete microrocket engine system consists of three primary components: valves, turbopumps, and the cooled thrust chamber, which are combined in an expander cycle as shown Figure 1.1. Propellants first enter the device through valves at low pressure and are then pressurized by the turbopump to the required pressure at the inlet to the cooling passages. The propellants cool the thrust chamber walls in the cooling jacket to an allowable structural temperature while heating propellants in the process. A portion of the heated propellant then enters the turbine in a supercritical state to drive the pump. More specifically, the pump is driven by the enthalpy rise that occurs in the cooling jacket through heat transfer. Finally, the propellants are injected into the combustion chamber where they mix and react to produce high temperature combustion products that are expanded though the exhaust nozzle to produce thrust. A brief summary of the baseline microrocket performance specifications is provided in Table 1.1[15].

**Table 1.1 Baseline Microrocket Engine Performance Specifications [15]**

| Performance Specifications | |
|---|---|
| Thrust | 15N |
| Mass Flow | 5 g/s |
| Propellants | LOX\Ethanol |
| Pump Power | ~75 W each |
| Chamber Pressure | 125 atm |
| Material | Silicon |
| Thrust: Weight | ~ 1000:1 |

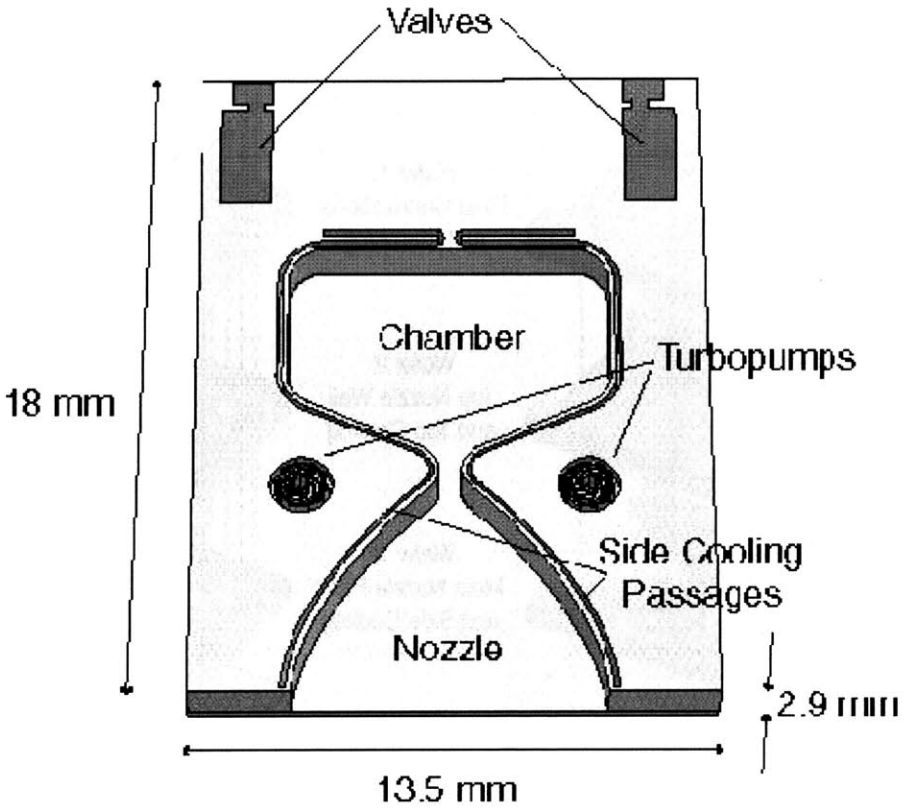


**Figure 1.1 Schematic of Microrocket Layout**

## 1.3 FABRICATION CONCEPT

The engine will be microfabricated by means of silicon MEMS (microelectrical and mechanical systems) technology, with the future possibility of using silicon carbide [20]. MEMS fabrication techniques involve the selective removal of material from silicon wafer substrates through a deep reactive ion etching process. The nature of the chemical etching allows complex planar geometries. Since all features must be two-dimensional shapes, the engines are fabricated as separate planar layers, then stacked and bonded together to create a three dimensional device as depicted in Figure 1.2. The number of layers necessary depends on the complexity and design height. The current microrocket thrust chamber in Figure 1.2 is made of six wafers bonded together.

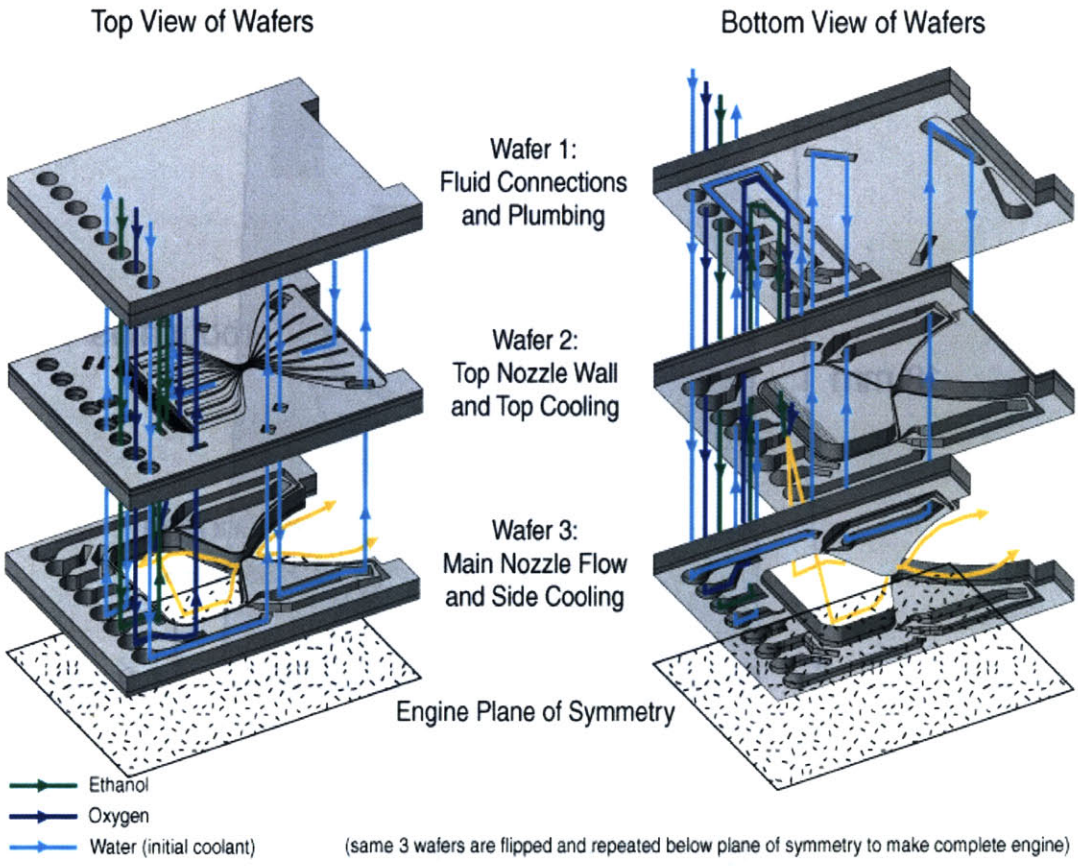


**Figure 1.2 Microrocket Engine Fabrication Assembly**

## 1.4 MICROTURBOPUMP CONCEPT

The turbopump is similar to the microturbocharger and microengine, except that it will have an impeller pumping liquid rather than a compressor pumping air. The turbomachine is a single shaft-less rotor radially supported by a gas journal bearing at its periphery. The large density difference between the liquid in the pump and the gas in the turbine makes it possible to design a rotor with the pump and turbine blades on the same side. This single wafer rotor is advantageous since it provides less fabrication complexity, eliminates misalignment problems, and provides an open inlet for improved fluid dynamics. An annular wall separates the pump and turbine and also serves as a gas thrust bearing pad. A 3D development of this design is presented in Figure 1.3 [27].

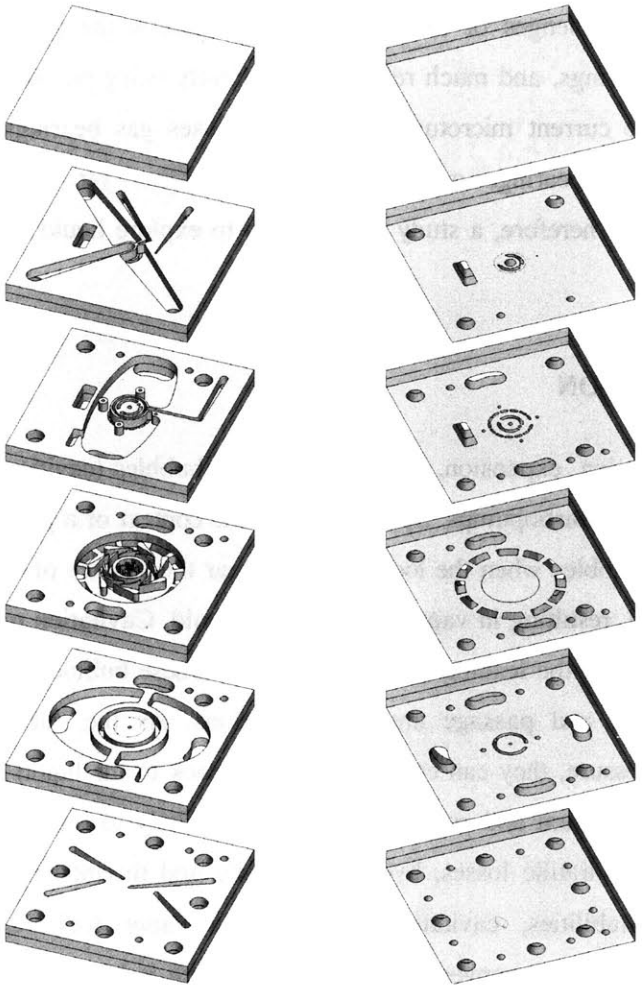

**Figure 1.3 Extruded Turbopump Geometry [27]**

The microrocket engine is designed for a pressure rise of 300atm with a corresponding rotor tip speed of 170 $ms^{-1}$ to ensure the high thrust to weight ratio and to enable regenerative cooling of the microfabricated thrust chamber. The performance of the turbopump, such as pumping efficiency and pressure loss is impacted by fabrication constraints. The constraints include no out of plane blade twist, right angle turns, and high aspect ratio channels. Calculations show that the pressure losses are less significant in the pump than for the turbine, where high Mach numbers are required due to the low-density fluid. Partial compensation for these losses resulted in raising the required pressure head of the pump to 300atm.

### 1.4.1 BEARINGS

One of the greatest challenges of the microengine project is the performance of hydrostatic and hydrodynamic gas bearings, and much research is currently being pursued to characterize bearings at this small scale. The current microturbopump design uses gas bearings to support the rotor. The performance of liquid bearings on a micro-scale has not yet been theoretically modeled or experimentally tested. Therefore, a study is underway to explore liquid bearing issue in further detail [27].

### 1.4.2 CAVITATION

Cavitation is the creation, expansion, and/or collapse of bubbles (cavities) in a liquid, and can cause performance decrease in turbopumps. Specifically, in the context of a pump, cavitation can be defined as the formation of bubbles when the local pressure near the surface of a blade falls below the vapor pressure of the liquid, resulting in vaporization of the liquid. Cavitation usually occurs on the suction side of the airfoil behind the leading edge of the blade. These bubbles grow at a rate determined by inertial, heat transfer, and passage area considerations. As the bubbles travel downstream and experience higher pressure, they can collapse violently back to the liquid state and can cause damage to the pump. This formation and collapse of bubbles is likely to limit the performance of the pump since it can lead to hydraulic losses, hydrodynamically and thermodynamically induced surge, flow and combustion instabilities, cavitation erosion, and vapor lock. Cavitation is a fairly well characterized phenomenon at conventional scales, although it has never been explored on a micro-scale where residence times are on the order of 400 microseconds. The bubbles may not have enough time to grow sufficiently large to cause catastrophic damage at this scale. Therefore, the effects of

cavitation on a micro-scale must be examined to determine the impact of this potentially serious issue on the microturbopump.

## 1.5 PRIOR WORK

As mentioned previously, work has been done to investigate the feasibility of a microrocket engine. This work concluded that a microrocket engine would be a useful device for applications such as micro launch vehicles and attitude control on satellites[13]. A preliminary design of a liquid bipropellant microfabricated rocket engine was performed [15], with major components characterized and evaluated for micro-scale operation. Propellants were investigated and characterized at micro-scales to determine their properties in the supercritical state. Finally, a liquid-cooled rocket thrust chamber was designed, developed, fabricated and tested with an external pressurization scheme [1].

To complete the pressure-fed microrocket system, a microturbopump is needed. Most recently, there has been an effort to fabricate and test a demonstration microturbopump. The device will first run on water due to its benign properties. The demonstration pump has two flow paths (one for the turbine and one for the pump) and have externally pressurized air bearings. The demonstration pump is designed to pump to a lower pressure. Also, a preliminary main pump blade geometry has been designed with a pressure rise of 250atm. The main pump has an inlet pressure of 34.5 atm, to ensure that cavitation will not occur. Preliminary inlet design specifications of these two pumps are briefly listed in Table 1.2.

**Table 1.2 Design Inlet Values for Microturbopumps**

| | Inlet Static Pressue | Inlet Mass Flow |
|---|---|---|
| Main Turbopump | 30atm | 2.5 g/s |
| Demonstration Boost Pump | 2.5atm | 2.5 g/s |

## 1.6 OBJECTIVES

The success of the microrocket engine depends on the ability to build turbopumps for the engine using current microfabrication techniques. Therefore one objective is to fabricate and test a functional micro-turbopump. In order to achieve this goal, the major technical issues regarding the fabrication of a turbopump must be addressed and overcome. This thesis investigates the cavitation phenomena by examining the effects of cavitation on a micro-scale. Once cavitation can be fully characterized on a

micro-scale, the potential effects of cavitation on a microturbopump will be defined and design criteria will be developed to avoid potential damage to the pump. Since the first functional turbopump will utilize water and ethanol as working fluids, the initial cavitation experiments will also be performed using these fluids.

## 1.7 APPROACH AND THESIS SUMMARY

This thesis investigates the effects of cavitation in micro-scale in order to establish the impact of cavitation on a microturbopump. First, a theoretical investigation of the cavitation issue is documented in Chapter 2. The pump blade geometries of the demonstration boost turbopump and the main turbopump are the designs used or the theoretical cavitation study. Theoretical cavitation inception curves and other cavitation effects are determined for these designs using theory derived from macro-scale phenomenon. The cavitation bubble growth phenomenon is then studied, to predict whether bubbles will have enough time to form at micro-scale. The accuracy of these theories on a micro-scale cannot be assessed without experimental data.

Therefore, to validate the theories presented in Chapter 2, a micro-scale cascade experiment was preformed to study cavitation. The experiment was microfabricated using MEMS technology and operating conditions similar to the envisioned microturbopump were simulated. The experimental design and fabrication of the device is described in Chapter 3. Chapter 4 explains the packaging, the experimental apparatus, and the test procedure used.

Chapter 5 presents the results of the experiments. There have been over 1000 tests run to date, each provided data useful to the understanding of cavitation on the micro-scale.

Computation fluid dynamics simulations on the cavitation device geometries used to validate the experimental results are also presented in Chapter 5, along with additional analysis and discussion. With cavitation characteristics on a micro-scale established, the performance of a microturbopump in cavitating conditions was estimated. Finally, the thesis ends with a summary of the work and thoughts for future work in Chapter 6.

# 2 MICRO-BLADE CAVITATION THEORY

This chapter theoretically investigates the formation, effects, and consequences of cavitation in relation to micro-scale pump blading. The cavitation phenomenon is defined, and research on effects of cavitation on macro-scale pumps is summarized. Theoretical cavitation inception curves are determined for a microturbopump using standard theory, and then deviations from the theory that may exist on a micro-scale are discussed. A theory is presented which utilizes bubble growth phenomenon to predict the size and extent of bubble growth on a micro-scale blading given blade lengths of 1mm and residence times on the order of 400 microseconds. Qualitative results and nominal solutions are presented, however, since much of cavitation theory is based on empirically derived constants, these theories need experimental data to more accurately predict the effect of micro-scale cavitation.

## 2.1 CAVITATION DEFINED

Before an examination of cavitation in a microturbopump can ensue, cavitation must be defined and the general concepts explained. This section defines cavitation as it relates to centrifugal pumps and explains important terms used to characterizing cavitation.

Cavitation is the creation, expansion, and/or collapse of bubbles in a liquid. These bubbles may be suspended in the liquid or trapped in tiny cracks, either in the liquid's boundary surface or in solid particles suspended in the liquid. Cavitation can occur in many different forms, including the optical, acoustic, and hydrodynamic realms. Cavitation associated with turbopumps is hydrodynamic cavitation. In this flowing system, the liquid velocity varies locally and, at the points of highest velocity, low pressures occur causing the liquid to vaporize. Vaporization most commonly occurs behind the leading edge of the blade on the suction side of the airfoil, since here the pressure drop is greatest. The extent and nature of the vaporization gives rise to three kinds of hydrodynamic

cavitation- here in termed traveling, fixed, and vortex[2]. *Traveling cavitation* occurs when cavities or bubbles form in the liquid, then travel with the liquid as they expand and subsequently collapse, as depicted in Figure 2.1. This cavitation is a transient phenomenon, making the fluid field relatively stable. In a more severe type of cavitation termed *fixed*, the bubbles grow much larger and the number of bubbles increases to form a fixed cavity. In *fixed cavitation,* a cavity or pocket is attached to the rigid boundary of an immersed body or a flow passage forms and remains fixed in position. The flow field fluctuates heavily in this kind of cavitation and, therefore, is highly unsteady. In both *traveling cavitation* and *fixed cavitation* voids form in order to relieve the tension that has developed in the liquid at the upstream end of the cavitation zone. *Vortex cavitation* is another common form of hydrodynamic cavitation which occurs in the cores of vortices which form in regions of high shear and often occurs on the blade tips of propellers or pumps. The shear is mostly caused by the 3D extruded geometry of the impeller, and thus this type of cavitation may not be a major issue in the 2D planar microturbopump. Other forms of cavitation that occur in a macro-scale pump, such as air-ingestion, internal recirculation and flow turbulence are not relevant to the microturbopump due to its innovative 2D planar design and therefore will not be discussed further.

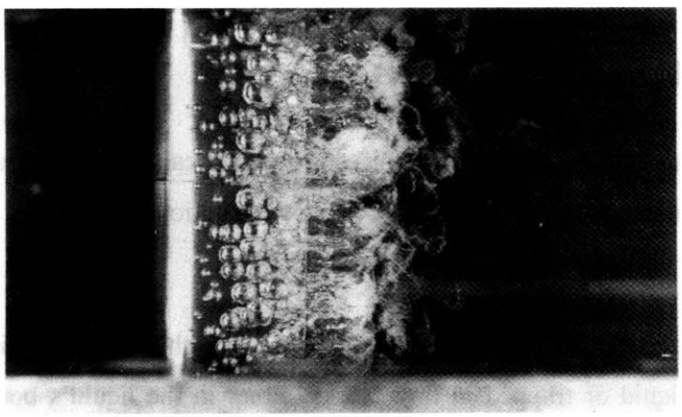

**Figure 2.1 Example of traveling cavitation bubbles forming on a hydrofoil [2]**

In addressing hydrofoils of turbopumps and other rotating machinery, *partial* cavitation is defined as a small attached cavity closes on the suction surface of the foil. This cavitation is most commonly observed in propellers and pumps [2]. When the cavitation bubble does not close until downstream of

[2] These names are arbitrarily chosen since there are no standard terms in the cavitation literature [3].

the hydrofoil, the hydrofoil is undergoing *super cavitation*. Here the fixed cavity is roughly the length of the foil, the flow becomes unstable, and the size of the cavity fluctuates violently. These two forms of cavitation are shown in the cartoon of Figure 2.2.

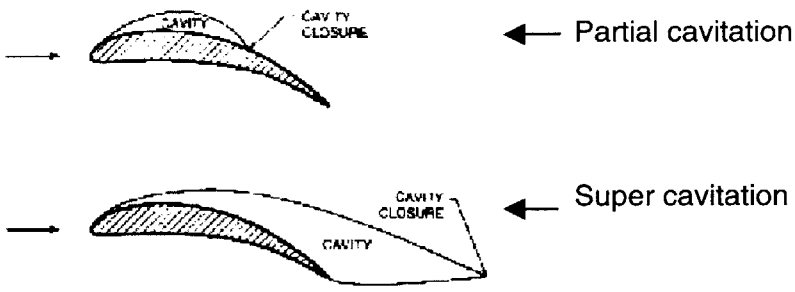


**Figure 2.2 Cartoon of super and partial cavitation on a hydrofoil**

Cavitation can exhibit hysteretic behavior. Modeling techniques, such as the one used in this chapter, predict *incipient* cavitation, the term used to describe the type and stage of cavitation that is just detectable as the cavitation appears. However, *desinent* cavitation is the term used to describe cavitation just before it disappears. Test results predict this phenomenon much more accurately than incipient cavitation. These conditions that mark the threshold between cavitation free and detectable cavitation are not always identical, because of hysteresis effects. For example, the pressure at disappearance of cavitation has been generally found to be greater, and less variable, than the pressure at appearance [3]. In some cases, liquid tensions of more than 1 atm were sustained for several seconds. Such instabilities can lead to flow oscillations and are important in liquid turbopumps [16]. Therefore, models must take hysteresis effects into account.

## 2.2 POTENTIAL CONSEQUENCES OF CAVITATION

The effects of hydrodynamic cavitation can either be those that modify the hydrodynamics of the flow of the liquid, or those that produce damage on the solid-boundary surfaces of the flow, or those that cause vibration and noise. In a pump, cavitation bubbles grow at a rate set by inertial, heat transfer, and passage area considerations. As the bubbles travel downstream and experience higher pressure, they collapse violently back to the liquid state and can cause damage. In cavitating macro-scale

centrifugal pumps damaging effects include: lower capacity, lower head, lower efficiency, hydraulic losses, hydrodynamically and thermodynamically induced surge, flow and combustion instabilities, cavitation erosion, or vapor lock. The collapse of the cavities or bubbles as they pass into the higher regions of pressure causes noise, vibration, and damage. However, cavitation on a micro-scale has never been explored, and the scaling laws that pertain to macro-scale cavitation may not apply here since the residence time for micro-scale cavitation is on the order of 400 microseconds, compared to 4 seconds for macro-pumps. Thus consequences of cavitation on a micro-scale cannot be well defined without proper modeling or experiments. The following section describes potential consequences of cavitation relevant to the microturbopump, extrapolating from macro-scale pump experience.

### 2.2.1 HYDRODYNAMIC EFFECTS

Hydrodynamic effects of cavitation in turbopumps are due to the interruption in the continuity of the liquid phase of the flow as gas cavities appear. As gas cavity volume displaces liquid, the flow pattern is modified and the dynamic interaction between the liquid and its boundaries is altered. The presence of cavitation in most cases increases the overall resistance to flow, and this limits or lessens the force that can be applied to the liquid by the boundary layer surface. Thus the angular deflection of the flow produced by a turning vane will be less when cavitation is present. Usually, the two hydrodynamic effects of overall resistance to flow and reduced turning combine to lower the performance of the turbopump. Performance losses in pumps are generally defined by loss of generated head in the impeller, where head is defined as:

$$\Delta H = \frac{\Delta P}{\rho g} \tag{2.1}$$

and $\Delta H$ is the generated head, $\Delta P$ is the pressure rise in the impeller, $\rho$ is the density of the liquid, and $g$ the gravitational constant. Hence, as cavitation develops, there is a decrease in both head and efficiency. For a microturbopump, another hydrodynamic effect is that the size of the cavitation bubbles could potentially grow large enough to block bearing passageways and thus generate rotor dynamic problems.

### 2.2.2 CAVITATION EROSION

The most widely recognized effect of cavitation is erosion, caused by long exposure to cavitation. This can affect the flow in two ways. It increases the surface roughness of the walls and can thus increase the hydraulic loss due to skin friction. Also, if the damage occurs in a critical region on the guiding surface, it can change the direction of the flow. Cavitation is known to damages many materials including metals, rubber, plastic, glass, quartz, concrete, and other nonmetallic solids. The collapse of bubbles in micro-passageways could influence the structural integrity of the pump. However, there is no documentation on the effects of cavitation on silicon since it has never previously been used in the production of hydraulic equipment. Single crystal silicon is a hard, strong, material, and therefore may not exhibit the same behavior as other materials.

### 2.2.3 EXTRANEOUS EFFECTS

Two of the most common effects of cavitation that do not involve alteration of the fluid flow or damage to the solid surfaces are noise and vibration. It has been found experimentally that considerable noise is produced by the collapse of the cavities [3]. The importance of cavitation noise depends largely on the application. In the case of the microrocket, cavitation noise from the microturbopump will hardly be recognized due to the high combustion and jet noise levels.

The cavitation process is inherently unsteady and may involve large fluctuating forces. Vibration may result if one of the frequency components of these fluctuations matches a natural frequency of a portion of the equipment. The vibration is usually of high frequency, ranging from several hundred to several thousand cycles per second. Another important effect is that cavitation can lead to system instabilities. Also, when enough cavitation bubbles exist, a catastrophic reduction in head occurs and leads to immediate termination of the pump flow, which is termed vapor lock.

## 2.3 MICROTURBOPUMP CAVITATION INCEPTION MODELING

In order to determine the extent of cavitation damage that will be produced on a micro-scale, cavitation inception and growth must be accurately predicted. The inception of cavitation occurs due to three factors: impurities in the liquid which give rise to the bubble nuclei, the physical and thermodynamic properties of the liquid, and the hydrodynamic characteristics of the flow (that is, the pressure and velocity of the liquid and physical size of the walls). To predict cavitation inception,

similarity relations are described in terms of a parameter that includes the major variables characterizing cavitation. Next, other factors and their effects of scaling are discussed. Finally, these principles are applied to a design geometry of a micro-turbopump, to determine the cavitation inception points along the pump's operating range. Cavitation growth is then modeled using a theoretical bubble dynamic model, and finally potential effects of cavitation on a micro-scale are characterized.

### 2.3.1 CAVITATION PARAMETER

To characterize cavitation in the microturbopump, it is useful to find a similarity parameter for of dynamically similar cavitating conditions, so that microturbopump cavitation inception can be inferred from macro-scale data. Although many variables affect the inception and subsequent character of cavitation in flowing liquids, the main variables include the boundary geometry, the flow variables of absolute pressure and velocity, and the critical pressure $p_{crit}$ at which a bubble can be formed or a cavity maintained [3]. Other factors such as viscosity, surface tension, temperature of the fluid, vaporization characteristics, and contaminants in the fluid cause significant departure from this classic theory; and their potential effects on a micro-scale will be discussed in Section 2.3.3.

To incorporate the main variables into a similarity parameter, a cavitation number has been defined, and to first approximation, this parameter has served well in macro-scale scaling operations[18]. This *cavitation parameter*, $\sigma$, is defined as:

$$\sigma = \frac{p_0 - p_v}{\frac{1}{2}\rho V^2} \tag{2.2}$$

where $\rho$ is density of the liquid, $V$ is the velocity upstream of the blade, $p_0$ is the upstream static pressure, and $p_v$ is the vapor pressure of the fluid. As $\sigma$ is reduced, the value of $\sigma$ at which nucleation will first occur is called the incipient cavitation number, $\sigma_i$. To first order, $\sigma_i$ determines when the pumps will cavitate. The lower $\sigma_i$, the lower the system pressure can drop before cavitation commences. Reduction in $\sigma$ below $\sigma_i$ causes an increase in either the number or extent of vapor bubbles.

In pumps, a relative flow between two blades results in a pressure variation along the blade surface. The difference between the local pressure the upstream pressure is proportional to the square of the relative velocity, using Bernoulli's equation for incompressible flow. Common practice is to denote this pressure distribution in terms of a negative a pressure coefficient distribution, $C_p$, which is defined as:

$$-C_p(s) = \frac{p_0 - p(s)}{\frac{1}{2}\rho V^2} \tag{2.3}$$

Therefore, as a first approximation, vapor bubbles appear instantaneously when $p$ reaches $p_v$, and so it follows that

$$\sigma_i = C_{p\,\min} \tag{2.4}$$

Thus the conditions at which pump cavitation inception will occur can be found by equating $-C_{pmin}$ from the pressure distribution along the blades to the cavitation number $\sigma$.

### 2.3.2 MODELING CAVITATION INCEPTION IN A MICROTURBOPUMP

Youngren has designed pump blade geometries for the demonstration boost turbopump and the main turbopump, using a 2D integral momentum boundary layer flow solver, MISES[3] [19]. For these geometries a *Cp* vs. *s* distribution can be extracted, defining

$$C_p = \frac{p_{wall} - p_{instatic1}}{q_{in1}}$$

$$ds = \sqrt{(dx^2 + dy^2)}$$

---

[3] More about MISES in Appendix A.

where $s$ is the parameterized distance along the blade. $C_p$ vs. $s$ curves for the main and boost turbopumps are shown in Figure 2.3 along with schematics of the blade and the flow over the blade. Both $p_{in1static}$ and the dynamic head $q_{in1}$ is fixed at the design values. Design inlet are listed in Table 2.1.

**Table 2.1 Design Inlet Values for Microturbopumps**

| | Inlet Static Pressue | Inlet Mass Flow |
|---|---|---|
| Main Turbopump | 30atm | 2.5 g/s |
| Demonstration Boost Pump | 2.5atm | 2.5 g/s |

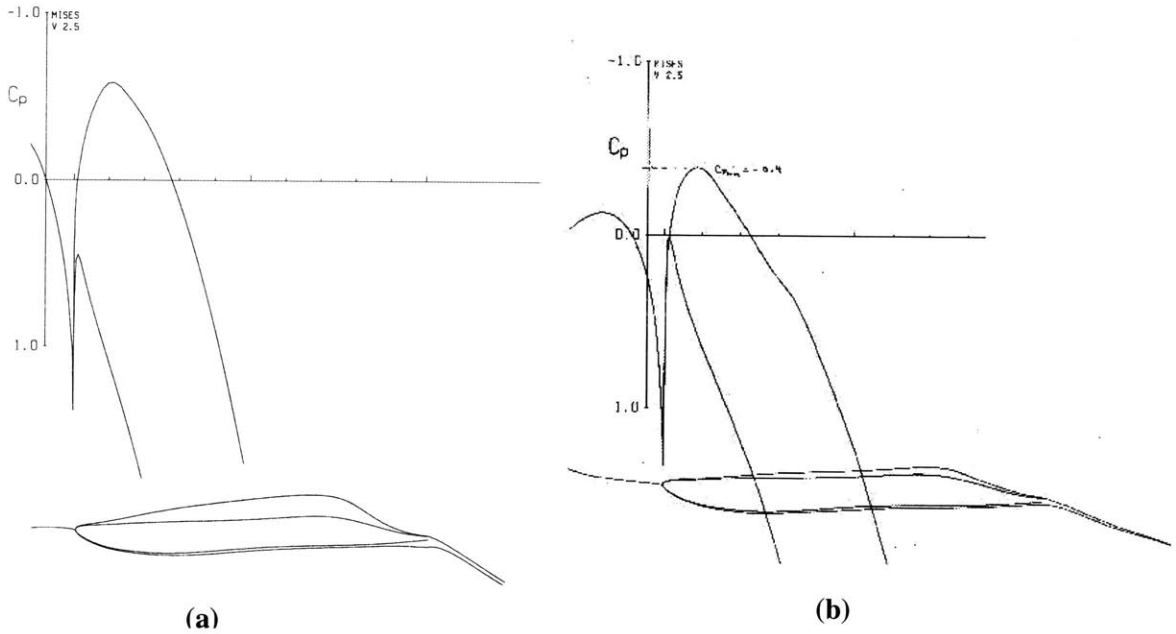


**Figure 2.3 $C_p$ distribution for (a) demonstration boost pump and (b) main microturbopump blades in a distorted geometry space**

Calculations for cavitation inception are carried out with these designs, using water and ethanol as working fluids.

Given the blade $C_p$ distribution, the theory predicts that cavitation occurs when $\sigma_i = C_{p\min}$. the blade pressure distribution is set by inlet static pressure and mass flow only. Using continuity and velocity triangle analysis:

$$\dot{m} = \rho A u_{xb} \qquad (2.5)$$

$$V_b = \frac{u_{xb}}{\cos\left(\tan^{-1}\left[\frac{\omega r}{u_{xb}}\right]\right)} \qquad (2.6)$$

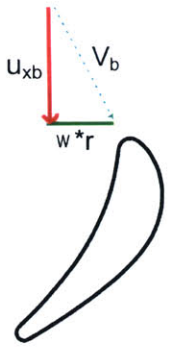


where $A$ is the inlet cross-sectional area, ρ is the density of the fluid, $u_{xb}$ is the axial velocity into the pump, ωr is the rotational velocity, and $V_b$ is the inlet velocity. Cavitation inception curves so calculated for the demonstration boost turbopump and main turbopump are shown in Figure 2.4 and Figure 2.5 respectively. Figure 2.6 plots both pump calculations and design points on the same graph. The flow should not cavitate at a pressure above the lines shown.

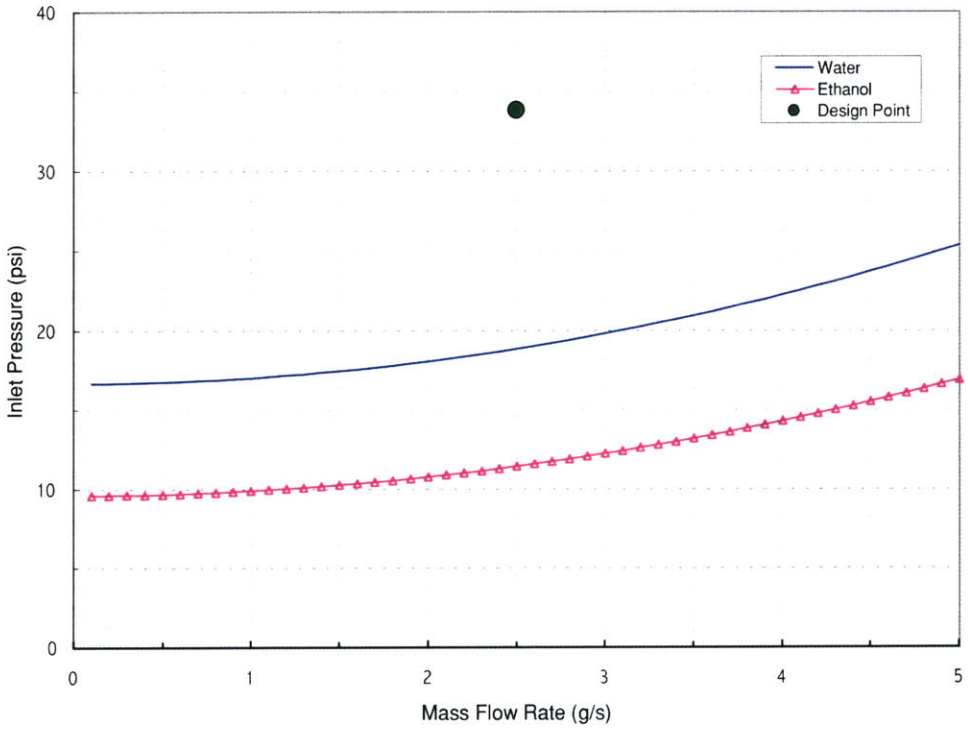


**Figure 2.4 Theoretical cavitation inception curves for the demonstration boost pump, with water and ethanol**

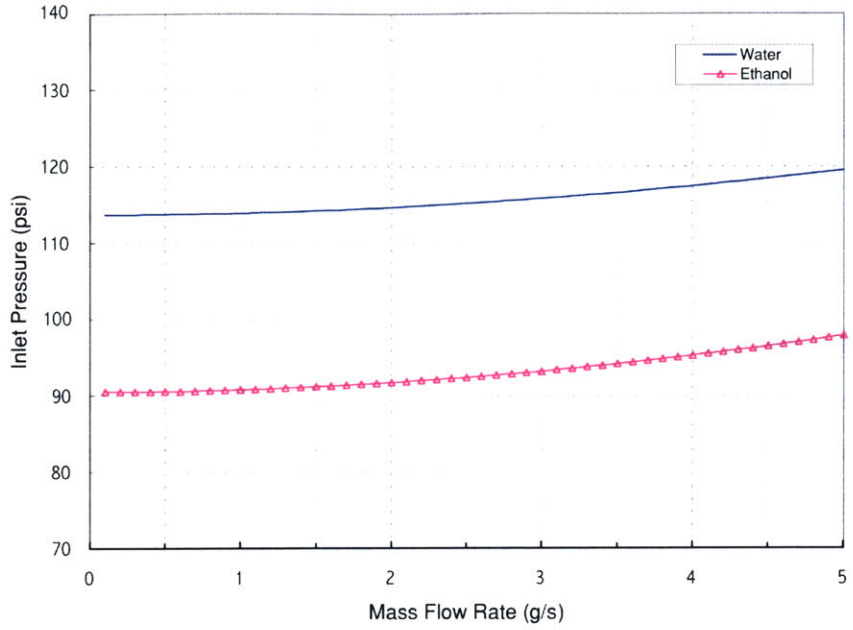


**Figure 2.5 Theoretical cavitation inception curves for the main pump blade designs with water and ethanol**

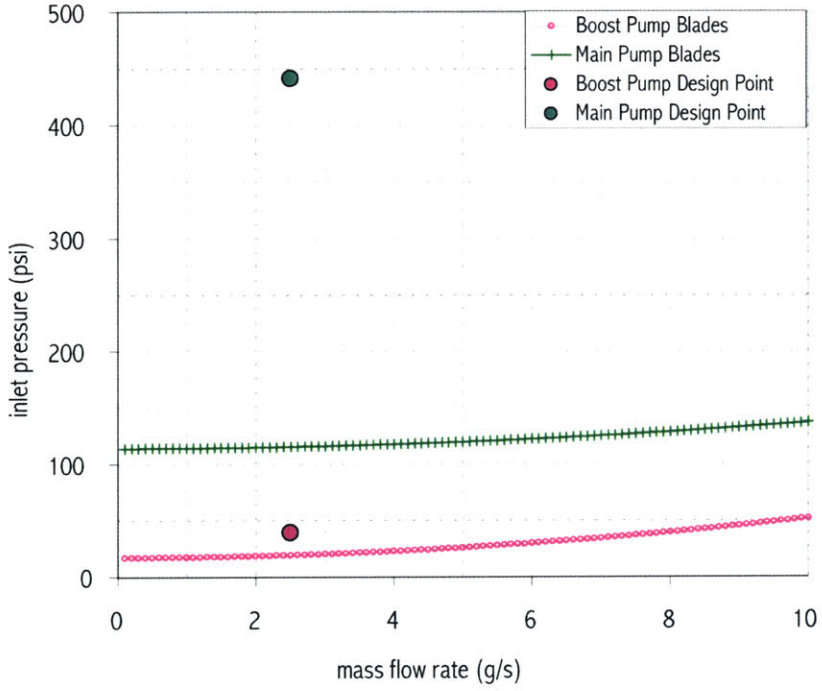


**Figure 2.6 Theoretical cavitation curves for both microturbopumps, showing relative design points with water**

For both the main and boost pumps, the design point is well above the cavitating regime to avoid cavitation. However, once cavitation on a micro-scale is characterized, these operating points could be made less conservative. Table 2.2 lists the cavitation inception points for the pumps at the design mass flow rate. From this table, it is evident that the demonstration pump cannot be started from atmospheric pressure without the presence of cavitation if the working fluid is water, but may be able to operate without cavitation using ethanol.

**Table 2.2 Cavitation inception points for turbopumps at a design mass flow rate of 2.5 g/s**

| Pump Type | Liquid | Cavitation Inception Point |
|---|---|---|
| Demonstration Boost Pump | Water | 18.8 psi |
| | Ethanol | 11.4 psi |
| Main Turbopump | Water | 115.1 psi |
| | Ethanol | 92.3 psi |

In conclusion, the above figures show to first order where cavitation *should* occur for a given inlet pressure and mass flow rate. However, cavitation inception also depends on many other influences including containment gas amounts, viscous effects, surface roughness, residence time and turbulence. These effects will subsequently be addressed in the next section.

### 2.3.3 SCALE EFFECTS ON CAVITATION

Although the similarity parameter predicts cavitation well at a macro-scale, it deals only with inviscid, ideal, steady flows. Viscosity, gravity, surface tension, thermodynamic properties, contaminants and conditions at the boundary can give rise to deviations from the classic similarity rule. Scale effects can be categorized into three groups for simplicity; hydrodynamic scale effects, thermodynamic scale effects, and molecular and other microscopic scale effects (such as surface tension.) Hydrodynamic scaling affect the flow outside of cavitation voids which therefore influence the minimum pressure in the liquid flow, irrespective of the presence or absence of cavitation. Thermodynamic scaling changes the cavitation process, which may cause the pressure at cavitation voids to depart from equilibrium vapor pressure at the bulk temperature of the liquid, and may cause temperature and time effects. This section examines these effects in reference to cavitation inception point and their relevance to cavitation inception predictions at a micro-scale.

### 2.3.3.1 HYDRODYNAMIC EFFECTS

There are 4 major hydrodynamic effects that make flow depart from the ideal; viscosity, gravity, turbulent and laminar separation, and relative surface roughness. In general, viscosity causes $C_p$ to have a dependence on Reynolds number, which thus causes $\sigma_i$ to be a function of Re. Given Reynolds number:

$$\mathrm{Re} = \frac{\rho V L}{\mu} \tag{2.7}$$

Where $\rho$ is the density of the fluid, $V$ is the velocity of the fluid, $L$ is a characteristic length, and $\mu$ is the kinematic viscosity. To keep the same Reynolds number for the same fluid properties, $V*L$ must remain constant, which means that $\sigma_i$ will increase with $V*L$. Vertical differences in the flow may change the cavitation inception point due to the change of the force and pressure field around the vertical body. Therefore, cavitation inception will have a dependence on the Froude number, which is defined as

$$F_L = \frac{V}{\sqrt{gL}} \tag{2.8}$$

Where $g$ is the gravitational force constant. Therefore, it can be seen that vertical differences in cavitation decreases with increasing $V/\sqrt{L}$. In the micro-scale, length scales are on the order of microns, in order to scale macro-scale data a very low velocity flow field must be found.

Turbulence can increase the cavitation inception point, since the transition point of a blade can trip the cavitation nuclei into growth [2]. Transition occurs at the laminar separation point, which provides a small recirculation zone in which a bubble can form. Therefore, even if the freestream residence time is short enough so that a bubble will not form, the recirculation eddies at the separation point may provide the gas nuclei with sufficient time to form a bubble.

The onset of cavitation for a flow with a surface irregularity is dependant on the relative height of the roughness, the boundary-layer shape parameter, $H$, and the roughness Reynolds number. Small surface irregularities are significant in local pressure reductions. The similarity relation for relative roughness has been defined as $h/L$, where $h$ is the height of the roughness and $L$ is the characteristic length of the flow field. Table 2.3 details the hydrodynamic cavitation inception scale effects.

**Table 2.3 Hydrodynamic Scale Effects of Cavitation Inception**

| Characteristic | Similarity Requirements | Effects on $\sigma_i$ |
|---|---|---|
| Viscosity Effects | Re= constant | $\sigma_i$ increases with $V^*L$ |
| Gravitational Effects | Fr=constant | N/A |
| Turbulence Effects | N/A | $\sigma_i$ increases with increasing turbulence effects |
| Effects of Surface Irregularities | h/L= constant | $\sigma_i$ increases with h/L<br>($\sigma_i$ decreases with increasing L if h increases slower than L) |

### 2.3.3.2 THERMODYNAMIC SCALE EFFECTS

Thermodynamic scale effects change cavitation properties and growth of the cavitation voids more than the inception point itself, and therefore will be discussed in further detail in Section 2.4.5. However, there are two effects that may cause a departure from the classic cavitation inception theory. These are the change in vapor pressure due to change in local temperature, and the effect of vaporization and heat transfer. If the vapor pressure of the fluid is increased, then the cavitation inception point will decrease correspondingly, and the presence of vaporization gases decrease $\sigma_i$ further. Assuming the velocity of the cavitation vapor bubbles is proportional to flow velocity $V$ and that the entire heat transfer takes place by turbulent convection only, then the Peclet number can characterize heat vaporization effects

$$P_e = \frac{C_{pl}}{v_l K} \cdot V \cdot L \tag{2.9}$$

Where $C_{pl}$ is the specific heat of the liquid, $v_l$ is the specific volume of the liquid, $K$ is the coefficient of heat conduction. A detailed discussion of this effect is not relevant at this early stage of development of micro-scale cavitation theory (further details can be found in [18]).

#### 2.3.3.3 MOLECULAR AND OTHER MICRO-SCALE EFFECTS

The most important concern for cavitation inception is the molecular and micro-scale effects that may change the cavitation inception point. These effects include surface tension, number of nuclei, contaminants in the flow, and residence time. At larger length scales, these effects have relatively little consequence on cavitation characteristics.

As surface tension of the fluid increases, there is a corresponding reduction in $\sigma_i$ so that the free stream pressure must drop below a previously observed inception point before a cavity forms. This hysteresis can also be associated with the population and characteristics of the undissolved gas nuclei entrained in the fluid and trapped in solid surfaces. In macro-scale data, it has been found that the difference of incipient and desident cavitation decreases as velocity and model size increase. Experimental data have also shown that $\sigma_i$ increases with velocity if the gas content is low and constant. However, with increased gas supply a larger number of nuclei become available, which decreases the inception point. Contaminants in the flow decrease the cavitation inception point for a fluid, since they provides surfaces for bubbles to start. The specific effect depends on the number and size of contaminants [2].

The most important scaling factor in a micro-scale is residence time. Residence time of liquids in micro-turbopumps are on the order of 400 microseconds, which imply that the bubbles may not have enough time to form, given the time lag hysteresis discussed previously. Since there has been no data taken at these time-scales, the scaling effect is uncertain. The role of residence time is important in determining the size and growth of the bubbles and thus will be addressed when examining bubble growth in Section 2.4.

#### 2.3.3.4 DISCUSSION

Although the scaling effects were presented individually, they interact. For example, changing the size of the device will alter both the residence time and the Reynolds number. Furthermore, the nuclei will now be a different relative size. Changing the speed to maintain Reynolds number may only confuse the issue by further altering the residence time. Moreover, changing the speed will also change the cavitation number. To recover the modeled condition now, one must change the pressure level, which can change the nuclei content. Therefore, experimental testing is vital.

### 2.3.4 CAVITATION INCEPTION MODELING CONCLUSIONS

Cavitation inception was modeled for the operating regime of the microturbopump blades based on macro-scale experience. Scaling factors were discussed which may cause departure from this model at a micro-scale. Contributors to this departure include the effects of surface roughness, surface tension, residence time, and containments of the flow. An analysis of bubble growth including these effects will be preformed in the following section. The analysis will be able to predict whether cavitation bubbles have enough time to form on a micro-scale and the effects of surface tension, surface roughness, and containments of the flow.

## 2.4 MODELING OF CAVITATION DYNAMICS

Once cavitation starts, the number and size of cavitation bubbles that form are vital to the understanding of the cavitation phenomena. Pressure forces influencing the bubble growth include surface tension, viscosity, heat transfer, and continuity. The pressure force effects will be presented in the next section. Models will be presented which determine the size of bubbles that can theoretically form in the microturbopump, and can subsequently be used to determine the extent of cavitation.

### 2.4.1 ASSUMPTIONS

Before a numerical analysis can be performed on the growth of cavitation bubbles in a microturbopump, several modeling assumptions will be made. These include:

- the working fluid is an incompressible fluid
- the passage is subjected to uniform pressure and temperature
- the cavity and surrounding flow field are spherically symmetrical
- mass lost by vaporization from the liquid into the cavities is negligible
- body forces are zero

### 2.4.2 THE RALEIGH-PLESSET EQUATION

The dynamics of a single bubble expanding and collapsing in a fluid are derived from the Raleigh-Plesset equation, which equates the kinetic energy acquired by the bubble expanding in the fluid to the work done by the expanding spherical boundary [3].

$$\frac{1}{2}\int \rho_L (4\pi R^2)\left[\frac{dR}{dt}\right]^2 dR = \left[\frac{4\pi r^3}{3} - \frac{4\pi r_0^3}{3}\right] P_l \tag{2.10}$$

By continuity, the velocity at any radius $R$ is inversely proportional to the surface area and thus inversely proportional to $R^2$. Using this relation, integrating, simplifying, and rearranging, the equation becomes the familiar form of the Raleigh-Plesset equation:

$$r\frac{d^2r}{dt^2} + \frac{3}{2}\left(\frac{dr}{dt}\right)^2 = \frac{1}{\rho_L}[P_l] \tag{2.11}$$

where $r$ is the radius of the bubble at time $t$, $\rho_L$ is the density of the liquid, and $P_L$ are the pressure forces acting against the liquid.

The pressure forces acting on the liquid in a micro-turbopump could be attributed to surface tension (inertial) forces, viscosity factors, thermal and heat transfer forces, forces due to a restricted passage area, and from the initial pressure inside the vapor bubble. Therefore, the Raleigh-Plesset equation can be written in our case as:

$$r\frac{d^2r}{dt^2} + \frac{3}{2}\left(\frac{dr}{dt}\right)^2 = \frac{1}{\rho_L}[p_x - p_{st} - p_v - p_{th} + p_d] \tag{2.12}$$

where $p_x$ is the pressure initially inside the cavity, $p_{st}$ is the pressure due to surface tension, $p_v$ is the pressure due to viscosity factors, $p_{th}$ is the pressure due to heat transfer and thermal considerations, and $p_d$ is the pressure due to the restrictive passage area. The following sections details each of these.

### 2.4.3 SURFACE TENSION

In a spherical cavity held in equilibrium by surface tension the excess of internal pressure over surrounding liquid pressure is given by

$$p_{st} = \frac{2\sigma}{r} \tag{2.13}$$

where $\sigma$ is the surface tension of the fluid. This term dominates when the bubble is small, since the pressure varies inversely with the radius of the bubble. In the numerical analysis of cavitation bubble formation within the microturbopump, the change of vapor pressure with surface tension was not taken into account. Since the pressure due to surface tension term works against bubble expansion, it is denoted by a negative sign in the Raleigh-Plesset equation, and retards the growth rate when the bubble is small. The effect of surface tension can be seen in Figure 2.7, which are curves adapted from Poritsky's study of viscosity and surface tension for dimensionless times and radii [29]. It can be seen that surface tension ($\sigma$=0.25) inhibits the growth of the bubble by almost 30%.

### 2.4.4 EFFECT OF VISCOSITY

Viscosity produces damping during the growth and collapse process. Consequently, increases in viscosity will decrease the maximum cavity size and rates of growth and collapse. For liquids with low viscosity, such as water, the effects of viscosity on cavitation are relatively negligible. To find the energy lost due to viscosity, assume that at the cavity wall pressure $p$ in the liquid, and (if the surface tension is absent) the resultant principal pressure $p_1$ must equal the pressure $p_i$ exerted in the cavity wall by any interior gas or vapor. Then

$$p - p_i = -4\mu \frac{dR/dt}{R} - \frac{2}{3}\mu \frac{\partial e}{\partial t}$$

(2.14)

For an incompressible fluid, $\partial e/\partial t = 0$, and thus the pressure due to viscosity becomes:

$$p_v = -4\mu \frac{dR/dt}{R}$$

(2.15)

Thus, viscosity always appears in the pressure boundary condition. Viscosity appears as an equivalent change in the internal cavity pressure. It can be seen from the preceding equations that the viscous effect is highest in the early stages of growth and near collapse when *dR/dt* may be very high. This can be seen in Figure 2.7, which shows a significant lag in time with the addition of viscosity.

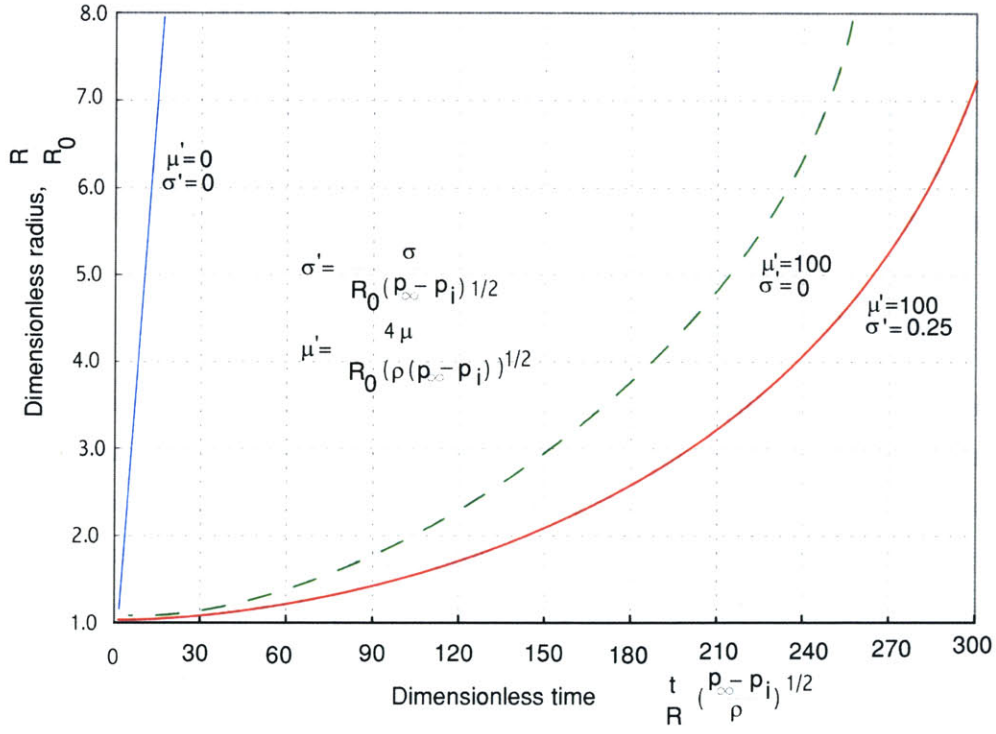


**Figure 2.7 Growth of a spherical bubble in an incompressible liquid with and without viscosity and surface tension. [Adapted from Poritsky [29]]**

### 2.4.5 HEAT TRANSFER

If conduction was restricted to an envelope of liquid which had a thickness of the thermal diffusion length and then given a temperature difference, the heat flow into the cavity must be balanced by vaporization[4]. This statement assumes that the aggregated surface area of spherical cavities passing any given point is directly proportional to the heat transfer surface area controlling the growth of cavities.

The heat flow into the cavity is given by:

$$\frac{(4\pi r^3)k_l(T-T_r)}{L} \tag{2.16}$$

where $k_L$ is the thermal conductivity, $T$ is the temperature, and $L$ is the thermal diffusion length. The heat flow to cause vaporization can be expressed as:

$$T-T_r = \frac{L\lambda}{3r^2k_l}\cdot\frac{d}{dt}\left[\frac{r^3}{V_v}\right]\frac{dr}{dt} = \frac{L\lambda}{k_lV_v}\frac{dr}{dt} \tag{2.17}$$

where $\lambda$ is the latent heat of vaporization, and $V_v$ is the volume of the vapor. By Clapeyron [3],

$$\frac{\lambda}{R_0T^2}(T-T_r) \approx \frac{p_{vap}-p_x}{p_{vap}} \tag{2.18}$$

and taking $V_v$ to equal the saturation value corresponding to $T$ so that $V=R_0T_lP_{vap}^{-1}$ then (2.17) and (2.18) can be rewritten as:

$$p_{th} = \left[\frac{3K}{\pi}\right]^{\frac{1}{2}} \cdot \frac{p_{vap}^2 \lambda^2}{k_l R_0^{\ 2} T^3} \tag{2.19}$$

where $L = \sqrt{\frac{3Kt}{\pi}}$ is the thermal diffusion length [4] solved by Plesset.

The inclusion of this term into the Raleigh-Plesset equation assumes that heat transfer to the bubble controls cavity growth and collapse. The pressure term inhibits bubble expansion, but has little effect at small scales, as shown in Figure 2.8. Latent heat of vaporization, thermal conductivity, thermal diffusivity, and vaporization pressure were taken to be constant at 25° C for water and ethanol[4].

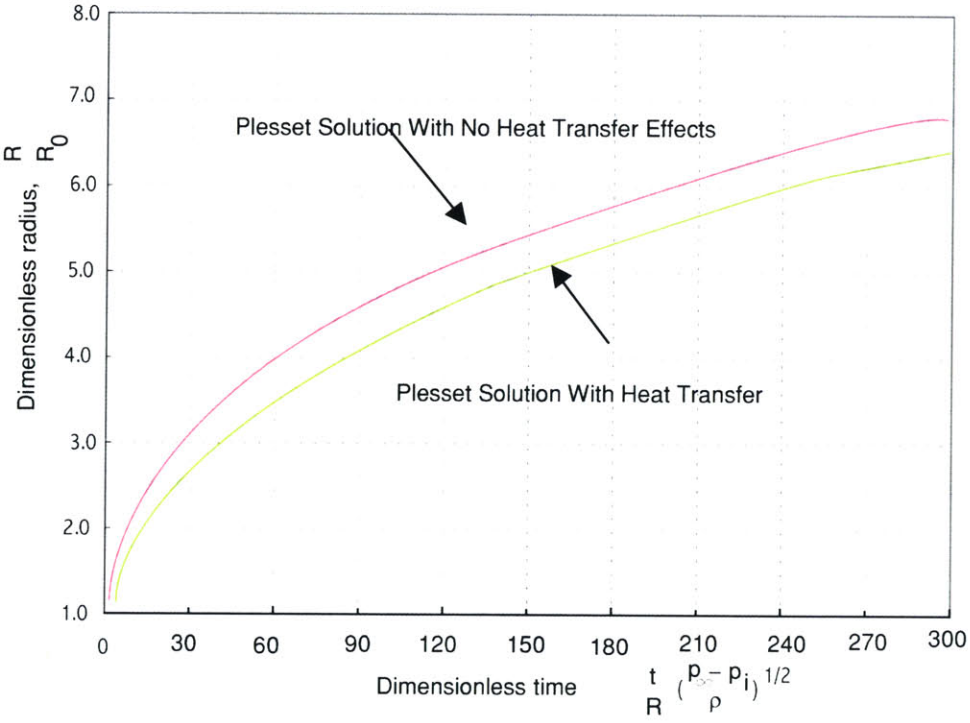


**Figure 2.8 The effect of adding heat transfer terms to the Plesset solution of bubble growth for water (2.19)(2.12)**

### 2.4.6 PASSAGE AREA CONSTRAINT

When flow is constrained by a duct, an additional pressure term arises that stimulates bubble growth. From continuity, velocity increases as flow area drops due to either walla constraints or bubble growth. The higher velocity decreases pressure in those areas (Bernoulli's equation). As local pressure drops, cavities grow. Therefore, a term $q_{vap}$ equaling the vapor flow rate is introduced:

$$q_{vap} = \frac{z_C 4\pi r^3}{3} \tag{2.20}$$

where $z_c$ is the number of cavities flowing through the passage per second per unit volume. The duct pressure can then be calculated by applying the Bernoulli equation and continuity to give:

$$p_d = \frac{Q_{bep}\rho_L(2Q_{bep}q_{vap} + q_{vap}^2)}{2A^2(Q_{bep} + q_{vap})} \tag{2.21}$$

where $Q_{bep}$ is the volume flow rate at the best efficiency point. $Q_{bep}$ has been assumed to be $1.5 \times 10^{-6}$ $m^3/s$ for the micro-turbopump.

The cavities' flow rate is estimated from data on industrial centrifugal pumps which show size and number distribution of bubbles ranging from 1mm to 15mm [4]. Figure 2.9 shows the variation of the rate of bubble growth due to different values of a non-dimensionalized $z'$, taking $z_c$ to equal the number or cavities interpolated from macro-scale data charts.

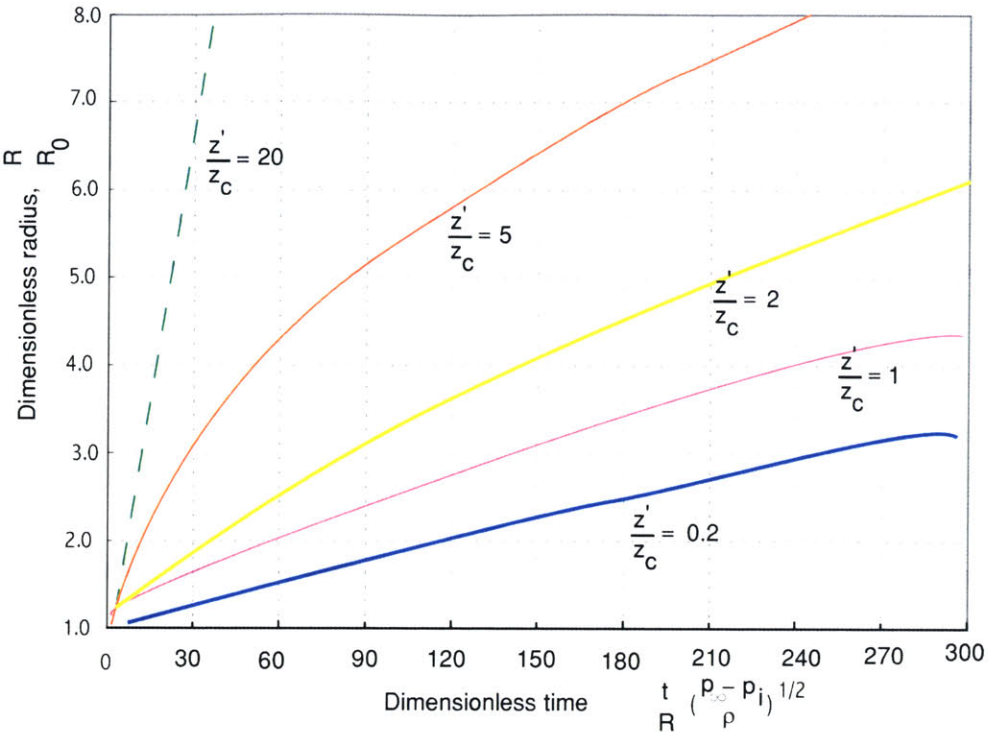


**Figure 2.9 Effect of Nuclei density on bubble growth (2.12)(2.21)**

From the figure, it is apparent that the vapor cavity density is important in determining the size of the bubbles that will grow during a specified residence time. Therefore, experimental data is needed to verify the numerical results.

### 2.4.7 NUMERICAL RESULTS

In order to complete the analysis, a pump geometry and working fluid must be specified, from which a residence time can be calculated. The residence time through the pump can be calculated as:

$$t = \frac{V\rho}{\dot{m}} \tag{2.22}$$

Where $V$ is the volume of the fluid through the pump, $\rho$ is the density of the fluid, and $\dot{m}$ is the mass flow rate through the flow passageways of the pump.

For the purpose of this analysis, the demonstration turbopump blade geometry was chosen [27]. A schematic of the wheel geometry is shown in Figure 2.10. In this design, the working fluid is water. For a mass flow of 2.5 g/s, the residence time through the pump has been calculated to be 440 microseconds. Furthermore, given the blade geometry and static pressure profile from MISES[19], the region that the flow would cavitate using the conventional approximation for cavitation inception at $C_{pmin}$ was calculated for each blade geometry. The results of these calculations are plotted in Figure 2.11 for both water and ethanol. Table 2.4 summarizes this calculation for the design mass flow rate of 2.5 g/s and a working fluid of water.

**Table 2.4 Residence Time calculation at design mass flow rate of 2.5 g/s**

| | Boost Pump | Main Pump | |
|---|---|---|---|
| Residence Time Total | 440 | 440 | Microseconds |
| Residence Time Cavitating | 150 | 110 | Microseconds |

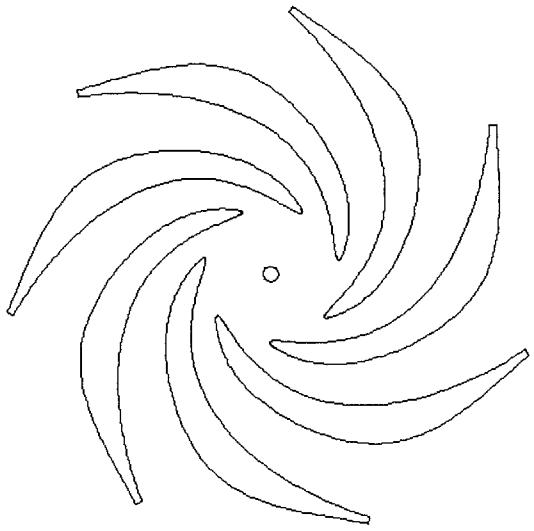

**Figure 2.10 A schematic of the pump wheel geometry used for residence time calculation [27]**

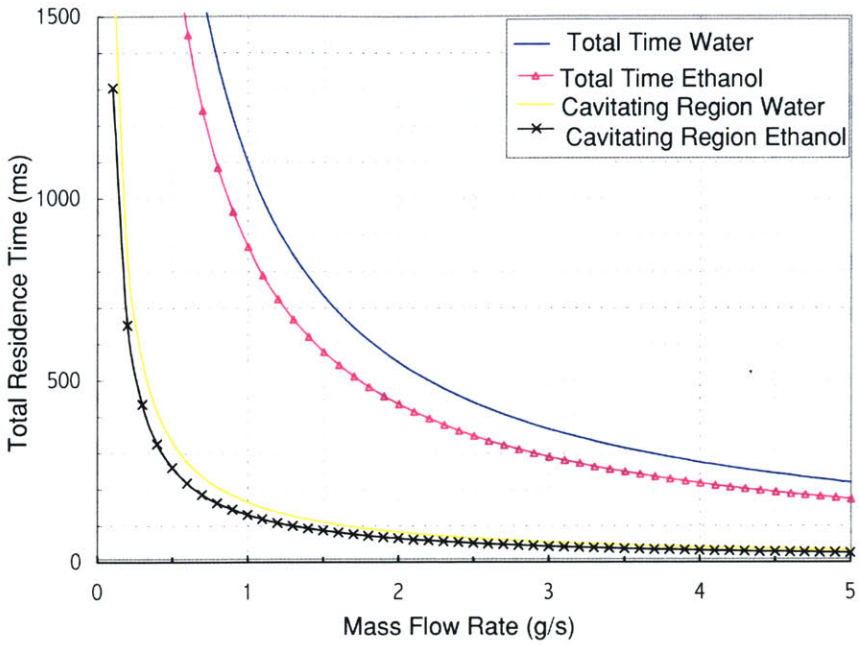


**Figure 2.11 Residence time calculations over the entire operating regime for different fluid mediums**

After the residence time is calculated, the initial conditions must be established. Since current filtering technology exists down to 0.3um [12], this value was assumed for the maximum initial bubble nucleus in the turbopump flow. The initial rate of bubble growth was assumed to be 0. (dR/dt=0)

Equation (2.12) was solved by a numerically using incremental time steps, specifically,

$$\dot{R} = \frac{R_{j+1} - R_j}{\Delta t} \tag{2.23}$$

$$\ddot{R} = \frac{R_{j+1} - 2R_j + R_{j-1}}{\Delta t^2} \tag{2.24}$$

with a time interval of 1 nanosecond. Using interpolated values for empirical constants described in the preceding sections, Figure 2.12 shows the variation of bubble size with mass flow rates in the cavitating regions of the microturbopumps. However, the accuracy of the figure is subject to estimates of the empirical values. For example, different estimates of $z_c$, can change the maximum bubble size by ±250.

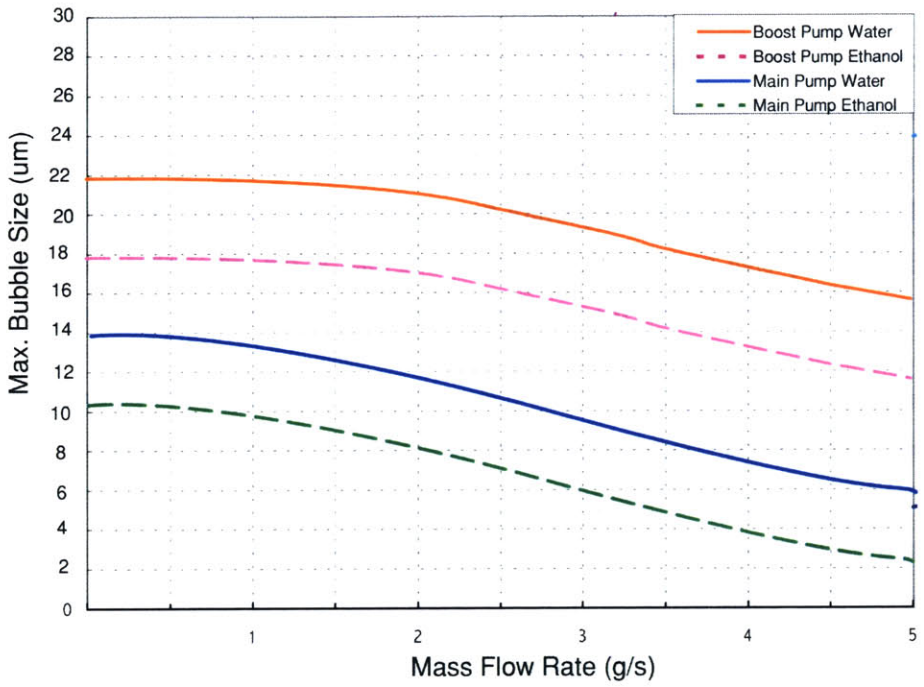


**Figure 2.12 Maximum bubble size calculations for turbopumps over operating regime for different working fluids**

## 2.4.8 CAVITATION ZONE LENGTHS

Results of Figure 2.12 enable the calculation of a cavitation zone length, and the distance along the impeller blade at which maximum cavity radius occurs. Using the following equation:

$$l_c = \sum \frac{(Q_{beq} + q_{vap})}{A} dt \tag{2.25}$$

where the sum is from $t=0$ to $t=$ value when $r=r_{max}$ to find the maximum cavity radius distance, and $t=0$ to $t=$value when $r=r_o$ to find cavitation zone length. Analysis up to this point assumes traveling cavitation. Whether the cavitation is traveling or fixed is dependant on $z_C$ and other empirical observations and therefore cannot be analytically determined without experimental data.

### 2.4.9 NONSPHERICAL BUBBLES

The preceding analysis has assumed spherical bubbles. They are not spherical in reality, and they grow and collapse in close proximities to other cavities and solid boundaries. Pressure fields are non-uniform and the bubble size may be large relative to the distances over which the pressure changes occur. This section discusses the departure from spherical shape. Macro-scale experimental data has proven that the Rayleigh assumptions are inaccurate only in the initial phases of growth and the final stages of collapse [3]. Therefore, the following discussion will be for these phases.

Two departures from spherical have been observed. The first is a general deformation of the shape of the bubble. Under some conditions of wall proximity and pressure gradients in the liquid, cavities flatten. The second departure from spherical is the occurrence of surface irregularities at the interface. Rebounding bubbles usually have a rough irregular appearance, and may be a cloud of minute individual bubbles. Using perturbation theory and a solution proposed by Plesset [28], the conclusion is drawn that due to surface tension, the non-spherical bubble may decrease so much that the original bubble breaks up and forms a cloud of smaller bubbles[2]. On the other hand, for large amounts of gas, the final size may be great enough to avoid large instabilities.

### 2.4.10 CAVITATION DYNAMICS MODELING CONCLUSIONS

The Raleigh-Plesset equation is the basic relationship used to determine the cavitation characteristics in centrifugal pumps. It can be shown that in the case of a microturbopump, the pressure due to the small passage area is the dominant term controlling bubble growth rate. Surface tension and heat transfer help to decrease the size of the bubble after 300 nanoseconds, are not sufficient to cancel a significant portion of the effects from the small passage area. However, since accurate values for the number of cavities per unit volume per second cannot be theoretically determined, only qualitative results can be estimated with the Raleigh-Plesset equation.

From the nominal solution of the Raleigh-Plesset solution, it is shown that for the design flow rate, 20 um radius bubbles can form. Thus for a 1000 um blade, 10 bubbles take up 20% of the effective blade, which could inhibit performance. However, the number of cavities per unit volume is not known. In order to accurately predict the cavitation characteristic, experimental data on a micro-scale must be gathered.

## 2.5 CHAPTER CONCLUSIONS

This chapter theoretically investigated the cavitation phenomenon on a micro-scale. Cavitation was defined, and potential damage discussed. Inception and bubble growth were analyzed. Potential deviations from macro-scale theory include the role of residence time, surface roughness, and passage area constraints. Much of macro-scale theory is based on empirical data. Estimates are presented, but empirical evidence must be gathered before the theories can be validated. The next chapter describes the design and setup of an experimental cascade used to establish cavitation characteristics on a micro-scale.

# 3 CAVITATION MICRO-CASCADE DESIGN AND FABRICATION

## 3.1 INTRODUCTION

In order to quantify the behavior of cavitation bubbles inside a microturbopump, experimental data must be gathered to validate theoretical modeling at this small scale. A non-rotating microfabricated cascade is the simplest approach to the issue of cavitation in a specified pressure distribution. This chapter describes the experimental design and fabrication of such cascades. First, objectives of the experimental cascade are defined. Two different blade geometries are designed to simulate both the cavitation inception point and pressure profiles of the microturbopumps. With these blade geometries, cascades are designed to simulate flow and blading properties. Theoretical cavitation inception curves and bubble growth analysis are presented on the cascade designs. Differences between the cascade and a microfabricated pumps are discussed, so that comparisons can be made with experimental results.

The second half of this chapter focuses on the fabrication of the cascades. Starting with the cascade geometries, wafer layers are designed and a mask set generated. The steps used in fabrication are explained. Issues that arose during cascade generation are discussed. Two builds of the cascades have been completed to date.

## 3.2 OBJECTIVES AND DESIGN REQUIREMENTS

The objective of the experiment is to collect data that characterizes cavitation phenomena in micro-scale pump blading, to reduce the risk cavitation poses to a microturbopump. A cascade was microfabricated to achieve this goal, and the following objectives were established for the experiment:

- Identify if/when cavitation occurs on a micro-scale
- Identify important characteristics of cavitating/non-cavitating liquid flow at a micro scale
- Gather empirical data needed to validate micro-scale cavitation theory
- Generate data needed for design tools and guidelines for micro-scale pump blades

Therefore, in order to achieve these objectives, the cascade was designed to:

- Similar length scales as the microturbopump
- Simulate the cavitating conditions of the microturbopump
- Similar pressure profile as the microturbopump
- Similar flow properties as the microturbopump (such as mass flow rate)
- Simulate the number of blades of a pump

From these objectives in mind, blade and cascade designs were produced as described the following sections.

## 3.3 EXPERIMENT BLADE AND CASCADE DESIGN

Two sets of pump blades were designed into cascades. A stationary cascade design cannot simulate an identical flow field to that of a rotating centrifugal pump. These devices attempted to preserve many of the important flow features. This section details the blade and cascade designs chosen to simulate the pump blading.

### 3.3.1 EXPERIMENTAL BLADE DESIGNS

Since the device is non-rotating, it will neither be able to achieve the high pressure recovery of a pump, nor the high rotational velocities which lead to a lower pressure cavitation inception point. Therefore, two blade geometries were designed in order to capture these two aspects of the pump. A symmetric blade shape was chosen to ensure that cavitation would occur even at very low operating

velocities, mass flow rates, and other inlet conditions. The cavitation inception point was designed to be close to the main turbopump design mass flow rate. A second, asymmetrical blade shape was designed in order to simulate the pressure recovery of the turbopump.

The symmetric blade shape is a modified version of the NACA 0045, with a high relative negative pressure ($C_p$) occurring about 20% down from the leading edge of the blade, as seen in Figure 3.1. In order to achieve the high negative $C_p$, the NACA 0045 leading edge was made increasingly more blunt, until the code would not converge due to heavy separation off the blade at the transition point. Due to this method of design, the blade exhibits a sudden increase and decrease in pressure around the transition point, which is about 50% from the leading edge. This pressure distribution can be seen in Figure 3.1.

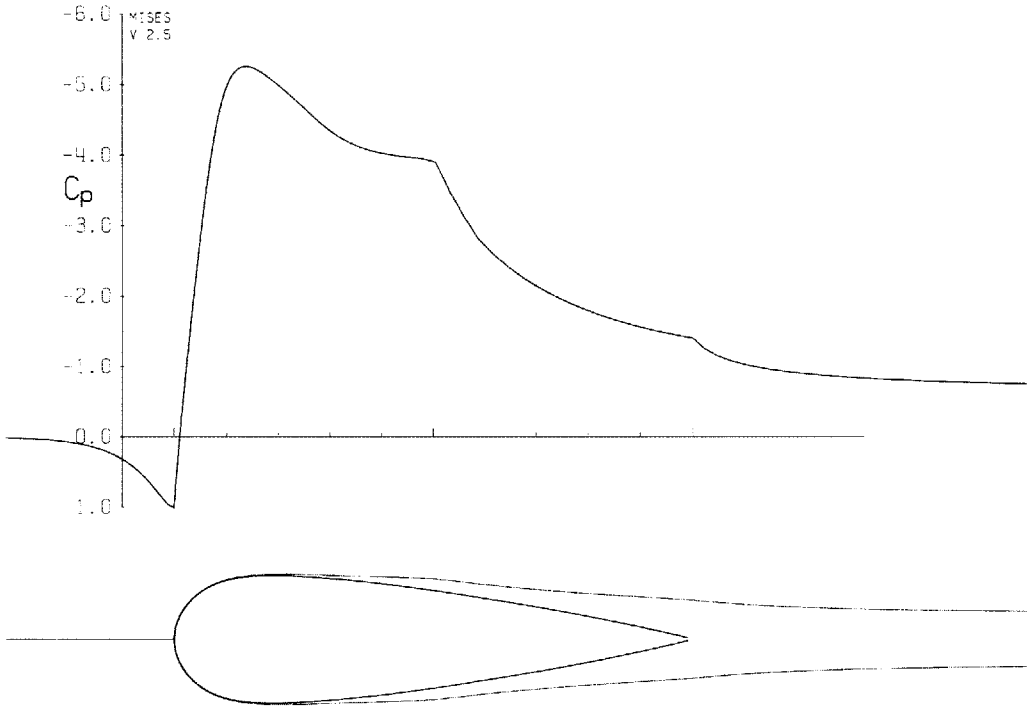


**Figure 3.1 MISES Blade design for a modified NACA 0045 symmetric blade, showing a high negative pressure peak and pressure perturbation at transition**

The asymmetric design incorporated a high turning radius and thus some pressure recovery. It was designed to be similar to the turbopump $C_p$ profile, as seen in Figure 3.2. Since this is a stationary cascade, the pressure rise is nominal compared to that of a turbopump. However, it does have the same $C_p$ profile as the turbopump main blade for the first 20% of the chord, and then exhibits pressure

recovery, which is the same trend as the turbopump (see Figure 2.3 for $C_p$ profile of microturbopump main blades). Since the point of minimum pressure, (the place where cavitation is likely to occur), is similar for both the turbopump and this blade design, a comparison can be made. However, cavitation inception for these asymmetric blades would occur at high mass flows and low inlet pressures due to the large flow area, thus at lower velocity for a given mass flow, requiring lower inlet pressures for cavitation.

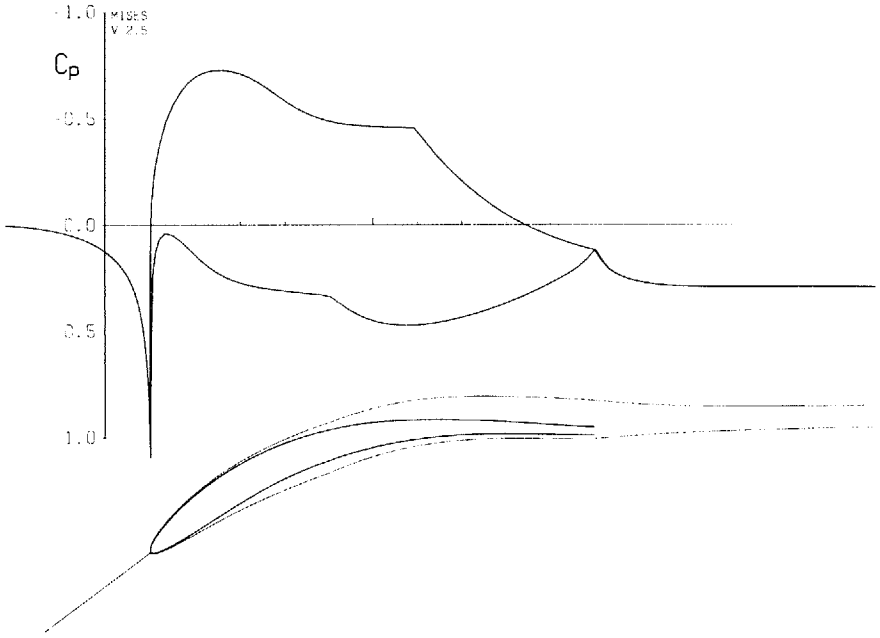


**Figure 3.2 MISES blade design for an asymmetric blade, showing a pressure recovery downstream and a pressure peak similar to that of the turbopump (Figure 2.3)**

### 3.3.2 CASCADE PASSAGE DESIGN

After the blade geometries had been determined, cascade geometries were designed to simulate the turbopump flow and blading conditions. Since a cascade will not produce the same velocity as a rotating device for a given area, the cascades were designed to a smaller area in order to preserve mass flow. However, decreasing the area also meant reducing the number of blades in the passageway. Therefore, for the symmetric blade shape, two different cascade geometries were designed, one simulating the correct mass flow, and other designed with the same blading as the pump. In order to keep the magnitude of size consistent with the turbopump, the blade length was

chosen to be 900um, and blade height 100um, compared to the 1000um length, 225um height blades of the demonstration boost turbopump.

Figure 3.3 shows the symmetric cascade of 3 blades, designed so that the cross-sectional area along the blades was reduced to that of the cross sectional area of the turbopump blade passages. The nozzle was designed using two-dimension wind tunnel contraction design charts [21] developed using inviscid flow analysis on a one parameter family of wall shapes, based on two cubic arcs. The set of design charts allows for a design so that separation from the nozzle could be avoided and the exit boundary layer thickness would be near its minimum. The diffuser was designed using Senoo and Nishi's [22] prediction of flow separation. This geometry exhibited a predicted cavitation inception point that agreed with the main turbopump blades at the design mass flow rate of 2.5 g/s (Figure 3.9).

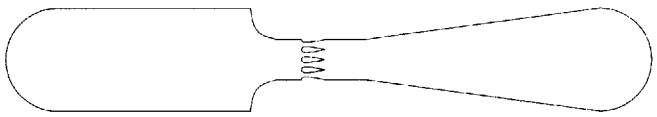

**Figure 3.3 Symmetric passage A with comparable inlet conditions as turbopump**

The second cascade passage using symmetrical blades was designed with 9 blades but no nozzle or diffuser to explore the effect of increasing the number of blades, or more specifically, how cavitation on one blade affects cavitation and pressures characteristics of other blades and passageways. Since there is no nozzle or diffuser, the boundary layer from the inlet will be fully developed by the time it reaches the cascade. These effects are further explored in Section 3.4, where 3D computational fluid dynamics are used to model the cascade. Figure 3.4 depicts this cascade.

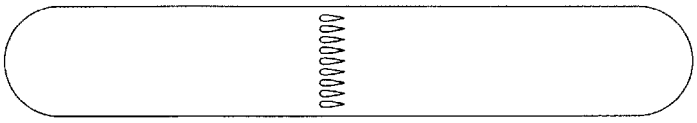

**Figure 3.4 Symmetric passage B with added blades**

For the asymmetric blades, a cascade was designed with to an inlet angle of attack of 37°. The inlet was designed using the same design charts as the first symmetric cascade. The diffuser was predicted not to separate. The asymmetric design passage is depicted in Figure 3.5.

**Figure 3.5 Asymmetric blade design passage**

## 3.4 3D NUMERICAL MODELING

MISES, quasi-3D compressible inviscid boundary layer code, was used to design the blades for the cascades. However, MISES does not account for the entire cascade features, including 3D top and bottom wall effects, which may be significant since the passage height is about 10% of the blade chord. Since the pressure profile is vital in simulating cavitation, and the growth of cavitation depends on the passage area (Section 2.4.6), knowledge of the stream tube height is needed. Therefore, a 3D Navier-Stokes flow solver, FLUENT, was used to validate MISES and predict the experimental results. The following section presents a brief overview of the numerical modeling efforts.

### 3.4.1 FLUENT MODELING OVERVIEW

Three stages of FLUENT modeling were performed to validate MISES and compare with experimental results. The first stage consisted solely of 2D modeling, in order to compare FLUENT and MISES. The second stage of modeling focuses on developing an accurate 3D model of one cascade geometry (symmetric cascade A) and a working fluid of water, to examine 3D effects on the pressure distribution along the blade. Stage three of computational fluid dynamics (CFD) modeling expands the stage two model to incorporate the other two cascade geometries as well as a working fluid of ethanol. The numerical solution can then be used for theoretical modeling, as done in Section 3.5, and also compared against experimental data, to prove the validity of FLUENT as a modeling tool, as presented in Chapter 5. Finally, the effects of the 3rd dimension can be closely examined with respect to each design, to determine spatially where cavitation inception would occur. Detailed results of these efforts are presented in Appendix A, along with descriptions of the numerical models used and explanation of modeling discrepancies. Chapter 5 validates stage three models against experimental data. Relevant modeling results are presented in the following section.

### 3.4.2 SIGNIFICANT RESULTS

This section summarizes results from the 3 stages of FLUENT modeling

**Stage 1:** The results of this modeling suggests that 2D FLUENT laminar solutions are highly inaccurate downstream of the blade, since recirculation eddies form downstream of the blade after the laminar separation point. The turbulent k-e model matches the MISES predicted $C_p$ distribution the best, although differing significantly from the profile during the laminar region. The stage of modeling established FLUENT as a viable flow solver

**Stage 2:** Stage 2 of FLUENT modeling solved for the pressure profiles along the 3rd dimension of the blade, showing that the point of minimum pressure occurs along the center of the blade. It also validated FLUENT as a 3D solver by comparing results with initial data. These comparisons showed that the 3D laminar case was the best case to run since the small passage area quenches out significant turbulent effects in the modeling. The stage of modeling determined a viable grid resolution to use for future grids and runs of 3D geometries, by refining the grid until no there was no solution dependence on the grid.

**Stage 3:** Stage three of FLUENT modeling established 3D numerical solutions of the cascade designs to be used in theoretical modeling and to be validated against experimental testing. The Symmetric A cascade matched the results from Stage 2, which depicts a less pressure recovery than that predicted by MISES. The Symmetric cascade B with 9 blades showed an even lower minimum $C_p$ point, with correspondingly less recovery of pressure along the blade. Therefore, the effect of adding more blades reduces the minimum point of pressure coefficient, thus making cavitation inception more difficult to achieve. These results are incorporated into the numerical modeling of Section 3.5. Figure 3.6 depicts the two symmetric cascade blade profiles along with the MISES predicted profile, for a working fluid of water. The results for ethanol are similar, except the pressure profile goes to a less negative $C_{pmin}$ and exhibits correspondingly less pressure recovery, due to the differences in viscosity and density. Comparisons of ethanol and water for the different cascades can be found in Appendix A.

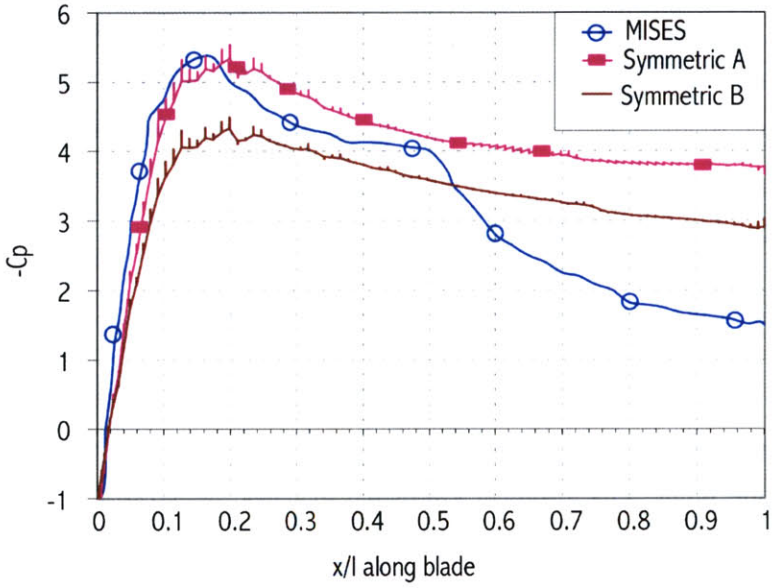


**Figure 3.6 The final stage 3D FLUENT pressure profile predictions for the two symmetric cascade designs, plotted against the 2D MISES prediction**

The 3D asymmetric FLUENT solution showed major deviation from the 2D MISES predicted pressure profile, as depicted in Figure 3.6. 3D effects cause the pressure coefficient to remain negative at the end of the blade, showing very little pressure recovery on the suction side of the blade. Also, the point of minimum pressure occurs more downstream of the blade than as predicted by MISES. Using a working fluid of ethanol changes the profile slight, with even less pressure recovery

downstream, as depicted in Figure 3.7. These 3D effects and consequences to cavitation predictions are discussed in Section 3.5

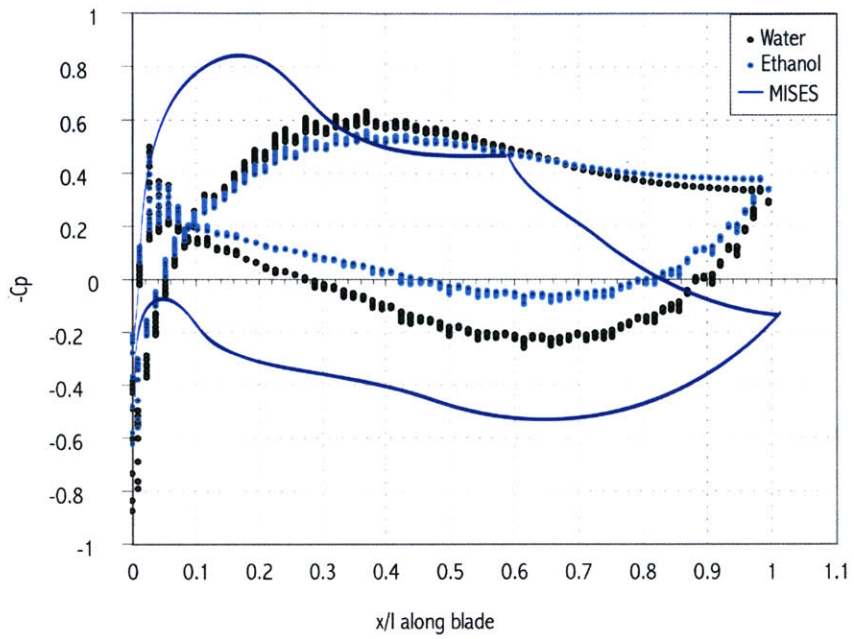


**Figure 3.7 FLUENT Asymmetric cascade pressure profiles using water and ethanol plotted against that predicted with MISES**

Figure 3.8 shows the 3D static pressure profiles of a run preformed in stage three of modeling. From this profile, the dependence of pressure with distance from the top and bottom walls is shown to be slight, with the lowest pressure usually occurring in the middle of the passageway. Pressure profiles for the other cascade geometries and working fluids showed similar results, and can be viewed in Appendix A.

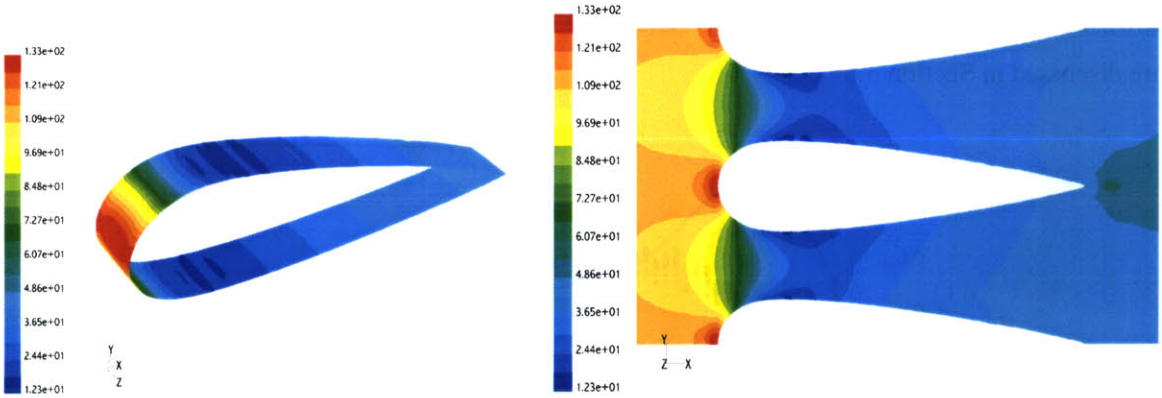


**Figure 3.8 3D static pressure profiles for the symmetric cascade A**

### 3.4.3 NUMERICAL MODELING CONCLUSIONS

Better predictions of the pressure profile along the blade for a given cascade geometry are solved with FLUENT, since the model can incorporate 3D endwall effects. These effects are shown to create less pressure recovery downstream of the blade, which stimulates cavitation growth. Also, the minimum $C_p$ changed slightly due to the 3rd dimension, which will affect the theoretical cavitation inception point. From the results presented in the previous section, more accurate predictions can be made about cavitation inception and growth on a micro scale, as presented in Section 3.5.

## 3.5 CASCADE CAVITATION PREDICTIONS

From the blade and cascade designs, predictions can be made about cavitation characteristics, and comparisons can be made with those characteristics predicted for the micro-turbopumps. Section 3.5.1 calculates the theoretical cavitation inception point for the cascade geometries, as well as compares these points with those for the microturbopumps. A bubble growth analysis is then performed on the cascade geometries in Section 3.5.2, where predictions of maximum cavity zone lengths and cavity size for a given mass flow rate and inlet pressure are presented.

### 3.5.1 DEVICE THEORETICAL CAVITATION INCEPTION

From the blade shapes, a cavitation inception curve can be mapped out for a given inlet pressure and mass flow rate using the method described in Section 2.3.1. These curves are plotted in Figure 3.9 for

a working fluid of water. From the curves it is evident that the rotating pump blades follow different cavitation curves than stationary cascade blades due to the effect of the additional rotational velocity term. However, the main interest is to establish the cavitation characteristics are for the design inlet pressure and mass flow rates of the main and boost pumps. As portrayed in Figure 3.9, the 3 symmetric blade cascade nominally cavitates in about the same area as the main pump blades, and the 9 symmetric blade cascade nominally cavitates where the boost pump cavitates. Therefore, examining the cavitation characteristics of the symmetric blades around the main pump design point may be valuable information in terms of elucidating the turbopump cavitation characteristics. The asymmetric blades, on the other hand, will give us some insight on the effect of pressure recovery on bubble growth and collapse.

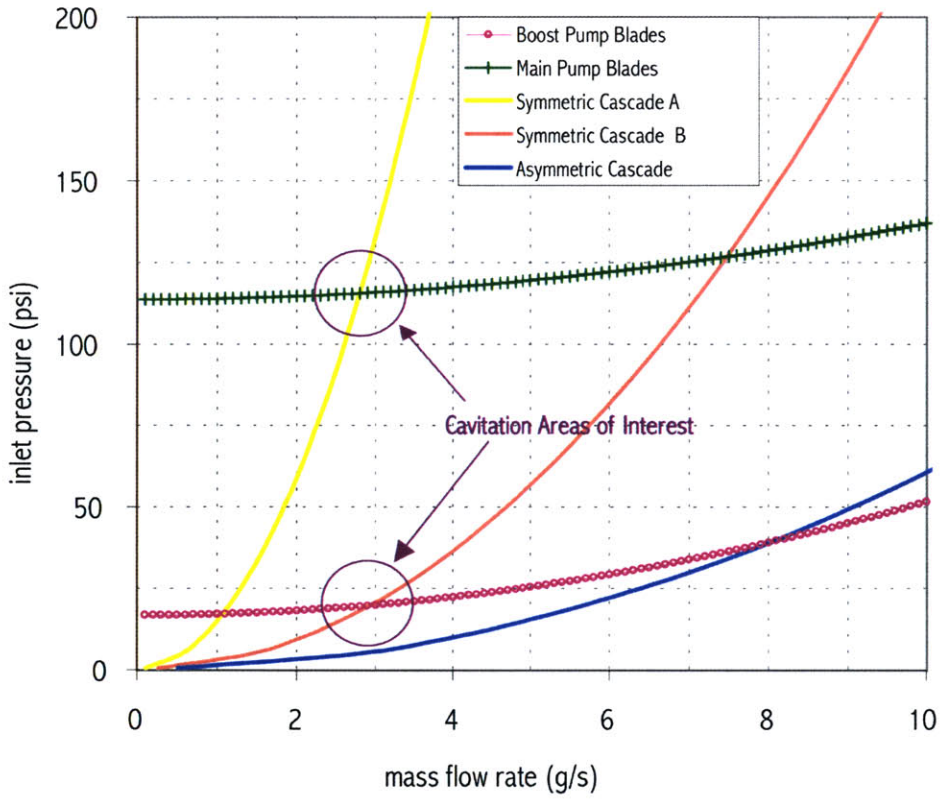


**Figure 3.9 Theoretical cavitation inception curves for water**

### 3.5.2 CASCADE BUBBLE GROWTH ANALYSIS

Following the analysis described in Section 2.4, maximum bubble size and cavitation zone lengths can be predicted for the cascades. Assuming that the blades were experiencing fully cavitating conditions ($\sigma_i$ was below $C_{pmin}$ for the duration of the traverse time along the blade) the maximum bubble radius for the symmetric blade can be predicted using empirical data from a macro-scale NACA 0045 blade [19]. The data from a NACA 2420 macro-scale hydrofoil was used when applying bubble growth equations to the asymmetric cascade, since this blade shape was the closest in geometry to the asymmetric blades [25]. The maximum bubble radius at the cavitation inception point is plotted in Figure 3.10, for all three cascades, and for both water and ethanol. These curves suggest that bubbles can form which are sufficiently large to cause perturbations in the flow.

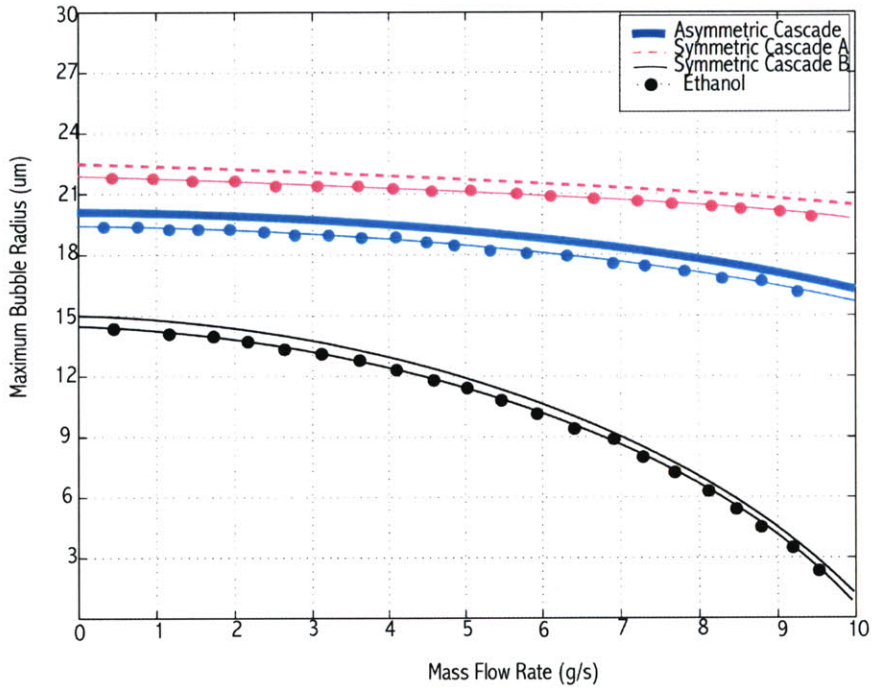


**Figure 3.10 Maximum bubble size vs. mass flow rate for the 3 cascade geometries and working fluids of water and ethanol**

Since empirical data is known for the macro-scale versions of the blades, this data can also be used to predict cavitation zone lengths for the cascade. Therefore, using equation (2.25), maximum cavitation zone length for a given mass flow rate is calculated for blade experiencing fully cavitating conditions. These results are plotted in Figure 3.11, and suggest that for the symmetric cascade A, cavitation will

be a problem above 2 g/s. For the other cascades, the maximum possible cavitation zone length is less than half the blade length.

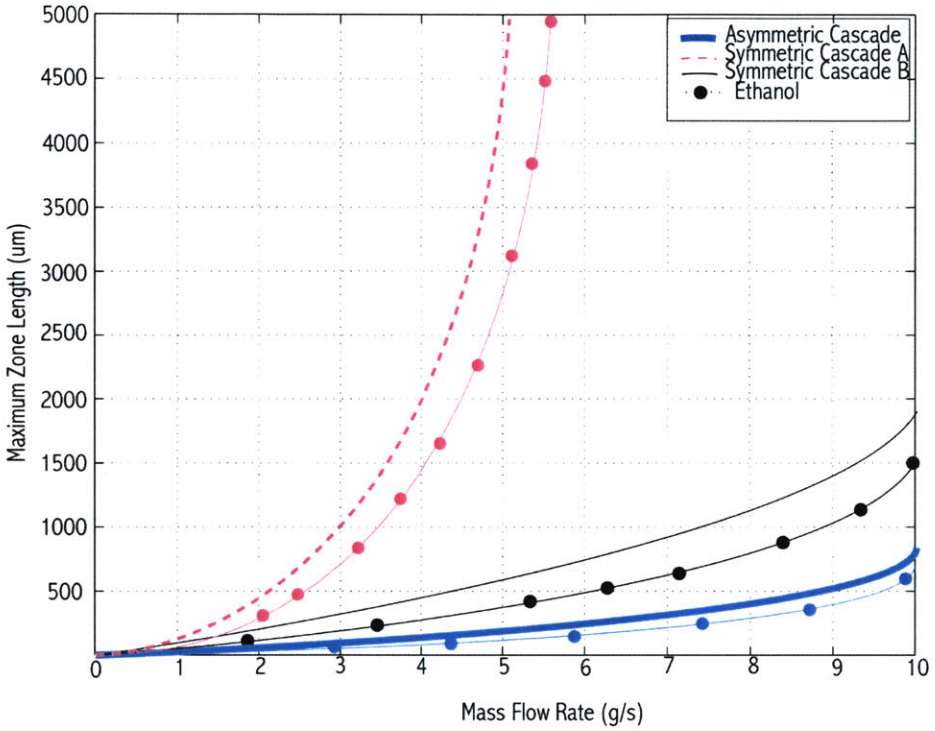


**Figure 3.11 Maximum cavitation zone length vs. mass flow rate for the 3 cascade geometries**

These results from the micro bubble growth analysis are based on empirical data gathered from the macro-scale. Once experimental data is gathered from micro-cascades, plots can be constructed from visual observations, and compared to the above. Empirical evidence on the number of bubbles per unit volume for a smaller scale can then be compared to that of a macro-scale and eventually be applied to analysis of bubble growth in a micro-turbopump.

## 3.6 DIFFERENCES FROM ROTATING DEVICE

Due to complications of bearings and rotor dynamics in a rotating machine, the simplest design that addresses the objectives listed in Section 3.2 is a stationary cascade. However, the cavitation characteristic differences between a rotating pump and stationary cascade deserve discussion. The cascades are designed so that the theoretical cavitation curves will simulate the same cavitation conditions at the design inlet pressure and mass flow rate, but they cannot simultaneously simulate

the pressure recovery. Therefore, the effects and damage of bubble collapse cannot be explored. Also, in rotating machinery there can be secondary cavitation due to the interaction between the rotating and the stationary members. Non-uniform flow in the upstream fixed passage becomes an unsteady flow downstream, which may cause cavitation [3].

## 3.7 CAVITATION DEVICE DESIGN AND FABRICATION

Once the blades and cascades were designed, a microfabricated device was designed to gather data on the cavitation characteristics along the blade. Optimally the device should allow for pressure readings along the blade and a window to visually observe cavitation. Section 3.7.1 details the individual device design, which incorporated eight pressure taps along the blade and passageways and a Pyrex wafer on top to allow for proper visual cavitation observance briefly discussed. The next section then discusses the microfabrication concept, outlining how the particular device can be fabricated. The obstacle of decreasing surface roughness of the blades during fabrication is discussed in Section 3.7.3. Finally, the devices layout per wafer is discussed in Section 3.7.4.

### 3.7.1 WAFER LAYERS AND MASK LAYOUT

In order to fabricate a device that allows for both pressure measurements along the blade and a viewing port of the blades to visually inspect the cavitation a 3D cavitation device was designed. The first device designed was a two 400um thick silicon wafer stack with a 500 um thick Pyrex wafer anonically bonded on top, while subsequent designs used a 3mm Pyrex wafer on top to allow the experiment to run at higher pressures. The clear Pyrex wafer allows for a proper viewing portal for the cascade passage and blades. The silicon wafer below the Pyrex consists of a cascade passage etched 100um deep into the top of the wafer, and 8 pressure taps 16um in radius around the center blade, etched through 300 um on the bottom. Figure 3.12 shows a close up the top silicon layer of a fabricated symmetric blade with pressure taps around the blade.

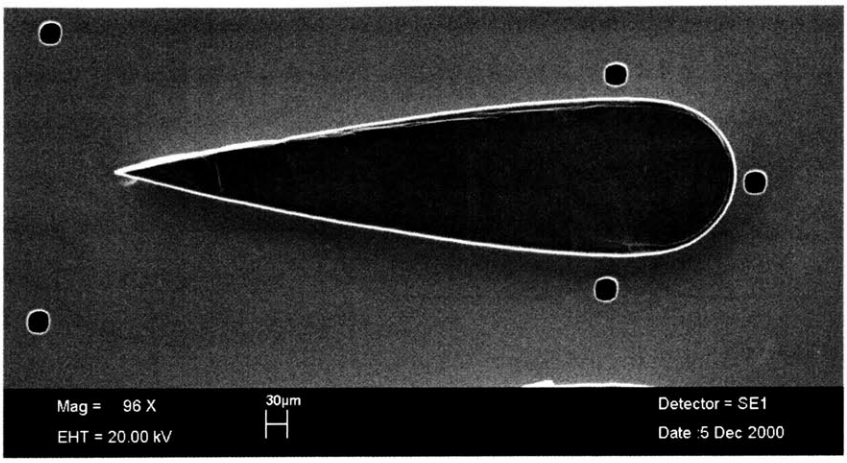


**Figure 3.12 Layer 1 and 2 of cavitation device, showing the center symmetric blade with pressure taps**

The top wafer has 2000um radius holes at the fluid inlet and exit of the cascade. These holes were also propagated though to the second wafer so that they could connect directly to external packaging. The inlet holes were sized large to ensure that cavitation would not occur until the fluid reached the blade passageways.

The second silicon wafer had 200um deep passages etched into the top taking the pressure taps into a bottom layer, which optimally had to be the same for all cascade geometries, since it consisted of pressure and wafer ports to be connected to external packaging. A schematic of these 4 silicon layers is presented in Figure 3.13. The design challenges included ensuring that the pressure ports on layer four were far enough apart to fit the external o-ring width, without the passageways on layer three overlapping. Layer 4 also had to be consistent for all 4-cascade designs in order to meet external packaging requirements, which added another design constraint. Therefore, an optimization of pressure tap number and placement resulted in 8 pressure taps, one upstream, 5 along the blade, and 2 downstream. The 13 masks needed to make the 4 different cascade experiments are described in Appendix C.

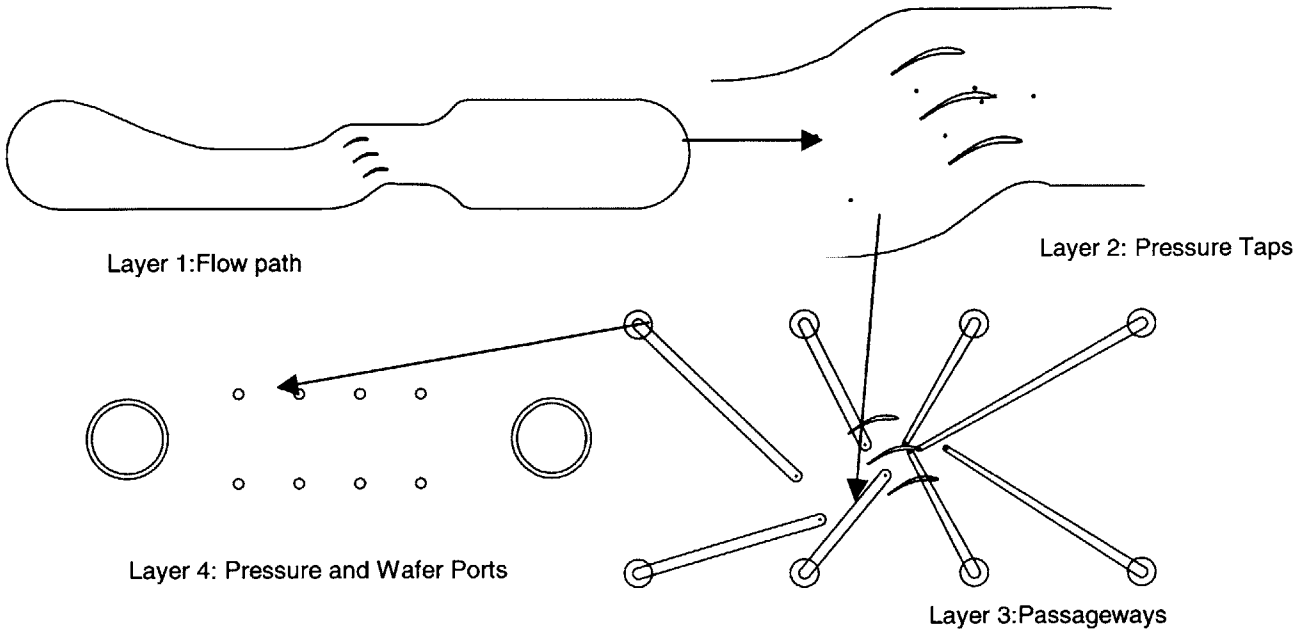


**Figure 3.13 Wafer Layers**

### 3.7.2 MICROFABRICATION CONCEPT

The cavitation device microfabrication process, like the turbopump, uses bulk microfabrication techniques. This involved chemically etching away selective material from silicon wafer substrates. Etched wafers were then bonded together to form a laminated stack of finished devices. The aspects of microfabrication that apply specifically to the cavitation device include deep reactive ion etching (DRIE), and Si-Si and anonic bonding. DRIE is the specific process used to do the etching for the device, while bonding techniques allow for the silicon wafers and Pyrex wafers to be bonded together to form a 3D device.

However, before etching and bonding, the wafers went through a preparation process. First, to define alignment marks on each side of the wafer, silicon dioxide was deposited on the wafer to protect the surface of the wafer during processing. The deposition was followed by a densification step where the wafers were held at 1100°C for 1 hour to drive off excess hydrogen remaining in the oxide from the deposition process. Then the oxide layers were patterned with masks. A 2um thick layer of photoresist was used as a mask for the etching of the oxide, and then pattered using the appropriate

mask. Once the oxide on both sides of the wafers was patterned, the DRIE process began. A complete process flow can be found in Appendix B [23].

Time-multiplexed deep reactive ion etching, or TMDE, was used to etch the cavitation devices. The process consists of alternating etch and passivation cycles. The etch cycle produces a shallow etch into the substrate using a fluorine chemistry, with $SF_6$ as the feed gas. This shallow etch is then coated by a thin polymer layer in the passivation cycle. During the etch cycle, the polymer is removed by ion-bombardment, meaning the layer at the bottom of the feature is removed first, exposing this lower surface to the etchant, while leaving the sidewalls protected. The lower surface is etched, and passivation begins again, re-covering the sidewalls. The cycles of etching and passivation repeat until the desired feature depth is reached[20]. Due to this etching technique, all features must be on the same characteristic dimension in order for the etch rate to be consistent for all features. Therefore, when designing masks for the cavitation dies, the large 2000um inlet and exit holes used *halo* etches. This technique is characterized by placing a smaller hole inside the larger hole needed to be etched in the mask itself, so that the halo in between the two circles is on the order of the other dimensions in the mask. The smaller hole then simply falls out of the wafer upon etch completion. This etching was done at MIT by a tool manufactured by Surface Technology Systems (STS).

Once all the etching was complete, the wafers were ready for bonding. The two silicon wafers were aligned and pressed together in an aligner-bonder manufactured by Electric Visions. Strong covalent bonds were then created at the interface by annealing the wafers at 1100° C. A Pyrex wafer was bonded to the top of the two wafer silicon stack using an electrochemical bond called an anonic bond. In anonic bonding a negative voltage is applied to the glass and a positive to the silicon layer. The elevated temperature of the process increases the mobility of the sodium ions in the glass and the negative voltage pulls the sodium ions away from the interface. As the sodium ions are pulled away from the interface a net negative charge is left at the interface. The wafers are held in intimate contact and thus a chemical bond forms.

### 3.7.3 SURFACE ROUGHNESS

One challenge in the fabrication of the device was overcoming surface roughness to ensure accuracy of the experiment. If the characteristic dimension of the roughness is a small fraction of the local boundary layer thickness, it may have little effect on cavitation. On the other hand, if the roughness protrudes far enough into the boundary layer, it can have the effect of a series of small surface

discontinuities and produce local cavitation at a higher value of $\sigma_i$ than would be characteristic of the general shape of the passage, as described in section 2.3.3. Therefore, it was desired to keep the surface roughness under 1um, which made fabrication more challenging. In order to achieve this level of surface roughness, the blade dimensions were made bigger than those for the turbopump. To date, features with a radius of curvature greater than 3um are usually 99% accurate in the STS etching machine. However, as depicted in Figure 3.14b, some blades were etched away due to uneven photoresist deposition. A visual inspection of each blade was performed before final bonding to ensure that the blades had a characteristic surface roughness that was less than 1/10 of the blade length, so that h/L<0.1, as depicted in Figure 3.14a.


**(a)**

**Figure 3.14 Surface roughness of the blades. (a) shows the nominal blade surface roughness, where (b) depicts roughness of blades with uneven photo resist deposition**

### 3.7.4 NUMBER OF CAVITATION DIES PER WAFER

Since the conventional wafer size used in the microrocket effort is 100mm, this wafer size was used in device fabrication. No feature should be closer that 5mm from the edge of the wafer, so 90mm diameter circle was considered the maximum extent of the cavitation dies [1]. Each die is 10mm x 31mm, so 12 dies could theoretically fit in this circle, in six rows of 2 dies, but since wafer non uniformities exist at a higher probability near the edges of the wafer [11], the top and bottom row have only one die centered, so that only 10 dies fit on each wafer. Alignment marks were also put in the sides of the wafer, so that each wafer layer could be aligned properly during photolithography and

bonding steps of the fabrication process. The cavitation die wafer layout configuration is shown in Figure 3.15.

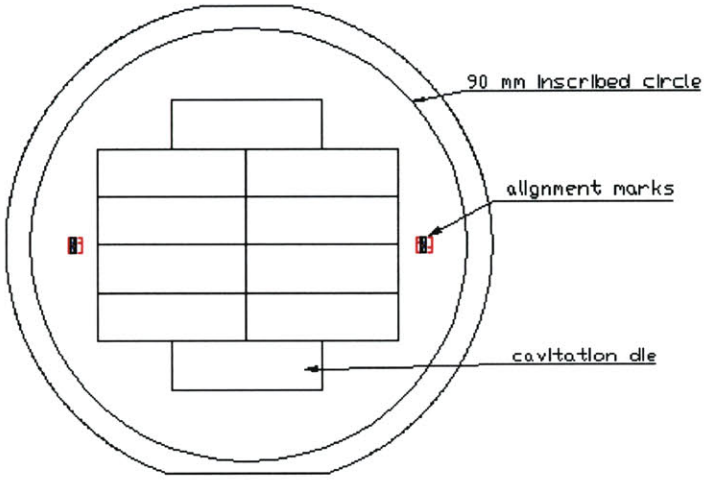


**Figure 3.15 Cavitation Die Layout in Wafer**

## 3.8 CHAPTER CONCLUSIONS

This chapter described the design and fabrication of microfabricated cascades used to characterize cavitation. Blade geometries and cascade designs were presented to best simulate the turbopump blade cavitation conditions. Theoretical cavitation inception curves and bubble growth analysis were presented for the cascade designs, with 3D computational fluid dynamic results. Differences between the cascade and a microfabricated rotating device were discussed, so that comparisons can be made with experimental results. The blade and cascade designs were then used to create a fabrication plan and mask set. The fabrication of the device was explained, and 2 builds of cavitation devices have been built.

# 4 EXPERIMENTAL SETUP AND TESTING

## 4.1 INTRODUCTION

The chapter discusses the packaging, and experimental setup and testing of the cavitation device. A method was devised to transport high-pressure liquids from external pressure tanks into the internal passageways of the cavitation device. The chapter also describes the experimental apparatus constructed to deliver the liquids into the packaging, and to provide engineering data used in analyzing the characteristics of cavitation on a micro-scale. The experimental apparatus consists of three major systems; the flow and pressurization system used to deliver the flow to the cavitation device, the data acquisition system used to record time-dependant data, and the video monitoring and recording system used to visually observe the effects of cavitation.

The other focus of this chapter is the experimental testing of the device. First, the experimental procedure is briefly explained. Next, a brief overview of the test plan and test matrix is presented. Finally, the section ends with summary of the tests performed and the status of each die before and after testing.

## 4.2 PACKAGING

A packaging scheme was developed that connected the device to both the pressure transducers used to collect pressure data, and the liquid intake and exit. The cavitation device was designed to operate with liquid inlet pressure up to 1000 psi at standard temperature conditions. Therefore, the cavitation die was mounted in a brass package using o-rings to create sealed fluid connections to the die. The package was based on the approach used by Frechette [6] for the microturbine-driven bearing rig. As shown in Figure 4.1, an aluminum spacer plate, with a hole to receive the cavitation die, was clamped between the top and bottom brass places to hold the die in place and establish the fluid connections.

In addition, the top plate had a rectangular viewing port fabricated so that the blades and 2 blade lengths upstream and downstream could be viewed during testing to observe cavitation.

During the first build, the spacer plate was 1.8mm thick, slightly thicker than the die, so that the fragile silicon would not come into contact with the top or bottom brass plates. Therefore, for the 3mm thicker dies of build 2, the spacer plate was made appropriately thicker. In all cases, the device is supported by O-rings distributed on the front and back surface of the die. In order to provide more structural support on the die, O-ring grooves were positioned on the top plate where the inlet and exit ports existed on the bottom die, even though there were no fluid connections [9]. The O-rings used for the liquid inlet and exit ports were significantly larger in diameter then those used for the pressure taps, since the ports were bigger (Figure 4.1). However, all the O-rings were the same thickness so that the compression rate was the same. AppleRubber .032 x .016 70BN and .171 x .016 70 BN O-rings were chosen, and the package was designed with O-ring grooves to create a 40% compression of the O-ring. The approach provided sealed fluid connections theoretically up to 1000psi.

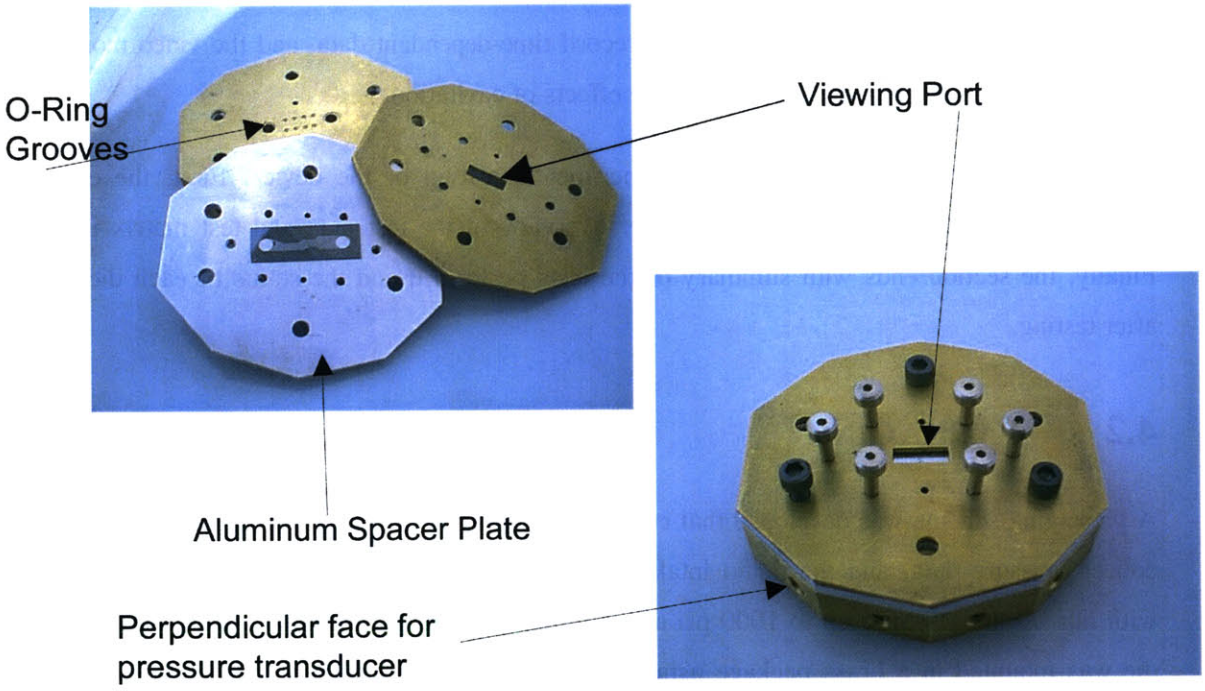


**Figure 4.1 Photographs of the package**

Kuilte pressure transducers were mounted on the bottom plate of the package. Therefore, the package was octagon in shape. For the inlet and exit ports, standard ¼" stainless steel tubulations were brazed

into the brass, which then were connected to Swagelok fittings to the rest of the experimental rig (Figure 4.2). Through holes clamped the package onto the rig table (Figure 4.5). Technical drawings of the packaging can be found in Appendix D.

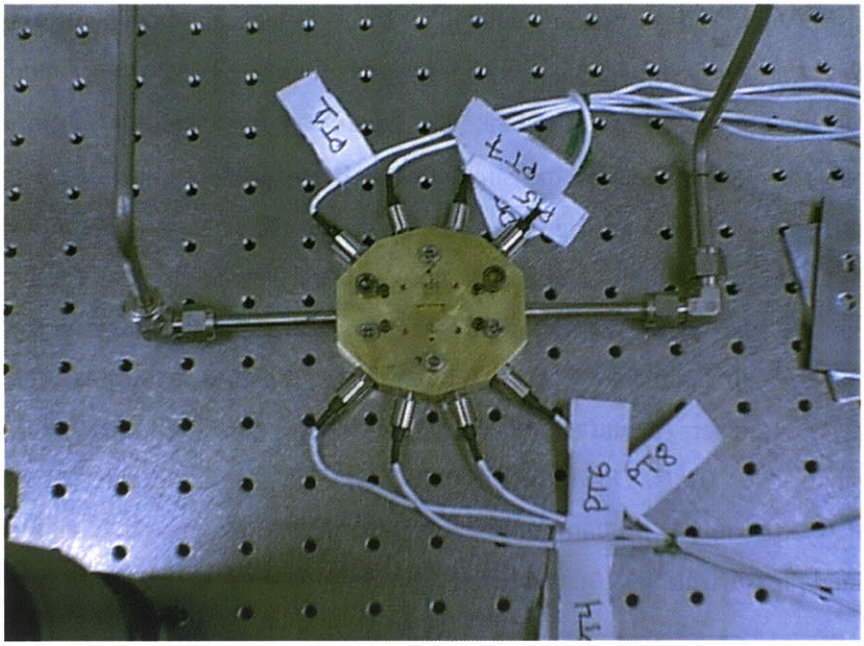


**Figure 4.2 Packaging connection to pressure transducers and fluidic connections**

## 4.3 EXPERIMENTAL RIG SETUP

The apparatus used to test the devices consisted of three primary subsystems. The pressurization and flow system connected the working fluid to the inlet and exit of the device at the desired pressure and mass flow rates. The data acquisition system provided accurate engineering data used in analyzing the device, and video monitoring and recording system allowed visual observations of cavitating devices. These subsystems will be described in more detail in the following sections. In addition, a TMC (Technical Manufacturing Group) Optical table was used to reduce vibration during the running of the experiment.

### 4.3.1 PRESSURIZATION AND FLOW SYSTEM

The role of the pressurization and flow system was to provide controlled pressure to the inlet and exit ports, at a given mass flow rate. This system was designed to accommodate a liquid microbearing

experiment to run during approximately the same time period and a microturbopump experiment to run in the future. A schematic of the pressurization and flow system is shown in Figure 4.3.

The stainless steel supply and dump pressure tanks, both rated to 1800psi, were attached to both a helium pressure tank and a vacuum tank, in order to reduce the amount of air bubbles that were present in the pressurized liquid. Also, once the supply tank was at vacuum, liquid from the liquid fill container was used to fill the pressure tank. The liquid was pre-filtered to 0.2μm, and went through a 0.5μm in-line filter once it exited the supply tank. Extra needle valves and 3-way valves were to ensure that the liquid turbopump rig could operate during the same time period. Mechanical pressure gauges were added to the supply and dump tank as a safety precaution in case the transducers failed. A sightguage was placed after the dump tank to indicate whether the dump tank was filled or empty. Upstream of the main inlet line, a mass flow meter was placed to measure the flow rate into the device. The flow meter (manufactured by MicoMotion, model CMF010) was designed for an operating range of 0-10 g/s. Downstream of the device, a metering needle valve regulated the mass flow if needed. Appendix E lists an example checklist used in running the cavitation device. A picture of the flow and pressurization system is depicted in Figure 4.4.

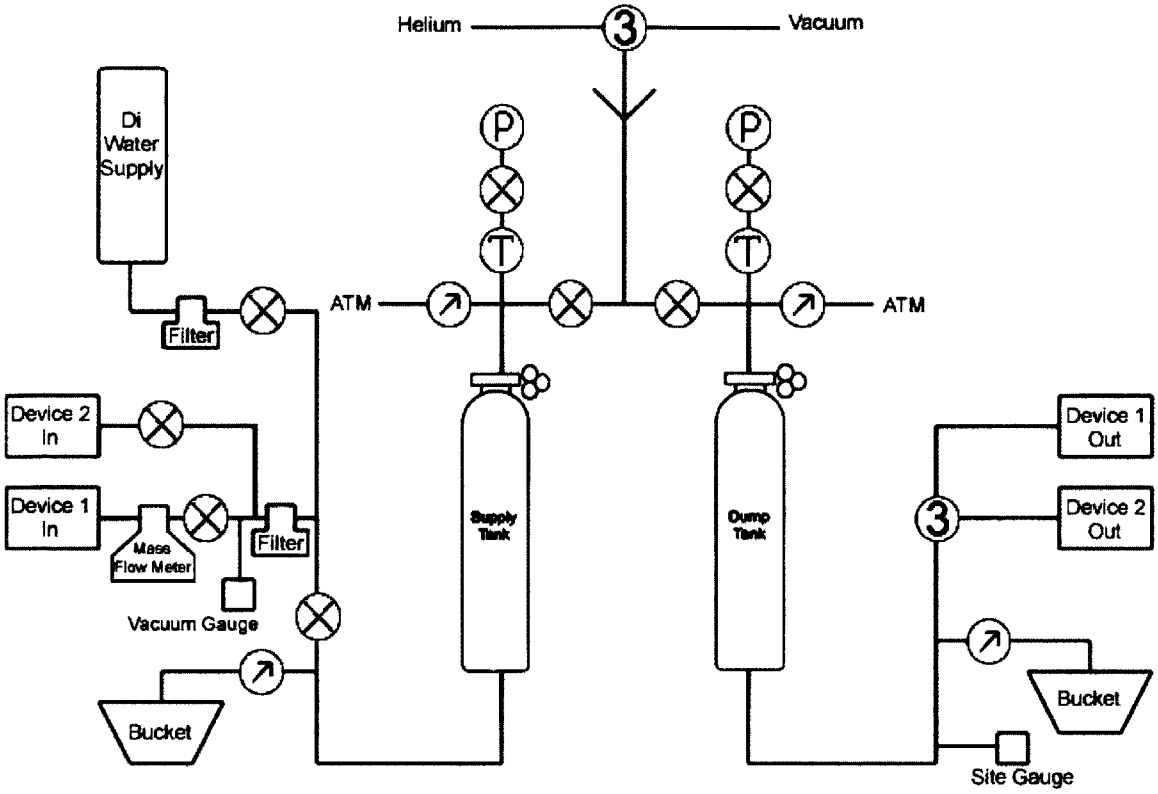


**Figure 4.3 Schematic of pressurization and flow system**

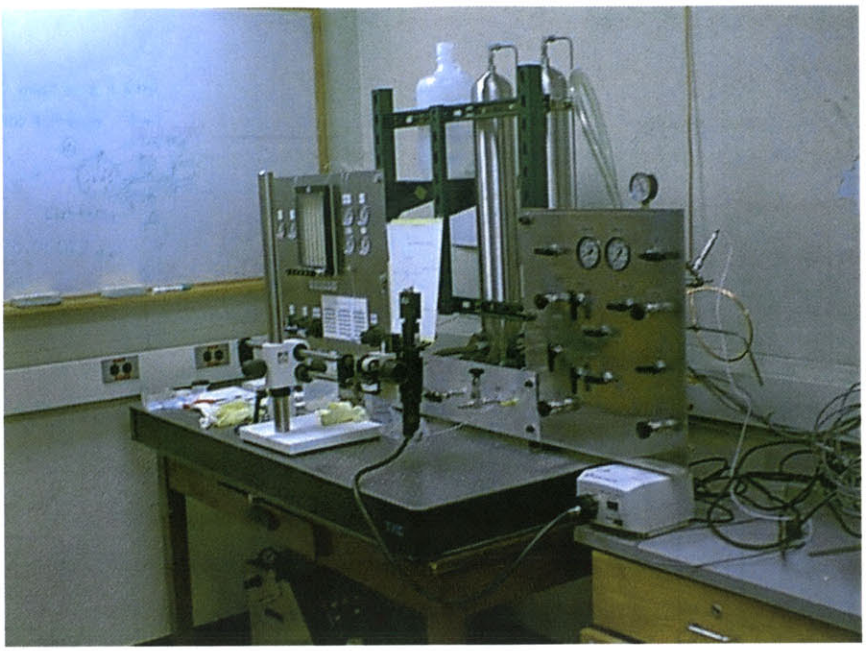

**Figure 4.4 A picture showing the full flow and pressurization system**

### 4.3.2 DATA ACQUISITION SYSTEM

The data acquisition system recorded the voltage and current signals from the pressure transducers and the mass flow meter, respectively. Over 20 Kulite pressure transducers, ranging from 100psi to 5000psi, were attached to LEMO connectors so that variable pressure transducers could easily be plugged into and out of a connection box. The raw signal from the inputs was sent though a 32-channel SCXI front mounting terminal block that was attached to an adjustable gain SCXI signal-conditioning module. The signal conditioner, which converts the raw signal to a 0-5V signal[4], took up 1 slot of a 4 slot SCXI chassis, which was then attached to a multifunction DAQ board which samples at 50kS/s (National Instruments). LabView Software running on a DellOptiplex Pentium Pro computer was used to acquire the data and generate the control outputs. The LabView software recorded the complete quasi-steady pressure and mass flow data for each run into a binary data file, sampling an average of 50 samples at a frequency of 50kHz.

---

[4] The current signal is placed through 2 SCXI current resistors to change the signal to voltage.

### 4.3.3 VIDEO MONITORING AND RECORDING SYSTEM

A video monitoring and recording system recorded the cascade cavitation. A video camera recorded the each experimental run, as depicted in Figure 4.5. The camera lens magnifies the port by about 100x. The image was recoded on SVHS or digital video.

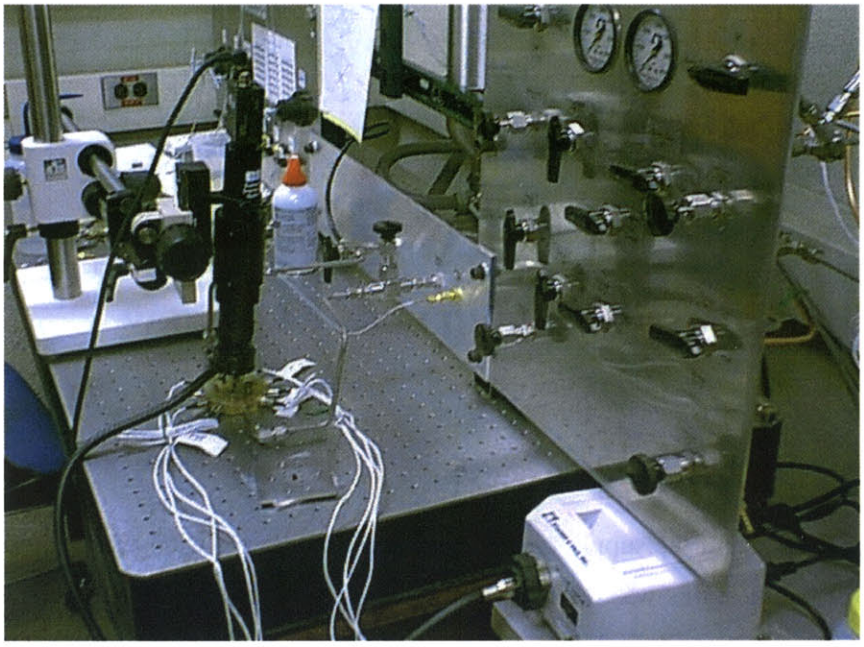

**Figure 4.5 Packaging clamped to TMC optical table with high magnification video camera**

## 4.4 CALIBRATION

This section briefly discusses the calibration procedure for the pressure transducers. The mass flow meter was pre-calibrated at the factory. To calibrate the 100psi pressure transducers, a 100psi test gauge with a stated accuracy of 0.25% was connected to the inlet pressure tank, and helium was used to pressurize this tank. Each pressure transducer was then subsequently attached to the inlet pressure tank. The helium pressure was increased in approximately 10 psi increments, and the pressure as measured by the test gauge was recorded at each point. A linear fit to the data yields a constant slope, in psi per volt of input signal, which were with 1% of factory given slope numbers. When reducing raw data from each test run, this slope is used, but the zero offset is recomputed based in the conditions immediately prior to the test.

## 4.5 EXPERIMENTAL UNCERTAINTY

The results of an uncertainty analysis are summarized in Table 4.1 for typical measured and derived parameters discussed in this chapter. Appendix F presents the details of the uncertainty analysis.

**Table 4.1 Summary of results from Experimental Uncertainty Analysis**

| Parameter | Type of measurement | Typical Value | Uncertainty | % Uncertainty |
|---|---|---|---|---|
| Pressure Taps | Measured | 10 psi | 0.5 psi | 5 |
| Liquid Mass Flow | Measured | 2.5 g/s | 0.01 g/s | 4 |
| Liquid Velocity | Derived | 20 m/s | 0.1 m/s | 5 |
| Zone Lengths | Observed/Measured | 1.5 lengths | 0.5 lengths | 30 |
| $C_p$ values | Derived | -5 | 0.025 | 5 |

## 4.6 EXPERIMENTAL PROCEDURE OVERVIEW

This section will briefly describe the procedure for generating a test run, with reference to Figure 4.3. The detailed checklists that were used to guide the test run are given in Appendix E.

The first step was to fill the supply tank and experimental device with water. To avoid the possibility of trapped air bubbles, this was done by drawing a vacuum between the DI water fill tank flow valve upstream of the supply tank and device to the valve at the outlet of the device. Once at vacuum, the flow valve was manually opened, allowing DI water to flow into both the supply tank and the experimental device. There was a valve between the supply tank and experimental flow channel for flow regulation during the fill process.

The next step was to pressurize the supply and dump tank. First, a pressure check was preformed to ensure that all the pressure transducers were functional and calibrated properly. The pressure tanks were both pressurized to 50psi, in increments of 5psi, and validated against the LABView outputs to ensure that all pressure transducers were reading the same output to within 1%. Then, the supply tank and dump tank were pressurized to the values specified by the test matrix for the run under consideration. The valve at the outlet of the experimental device was kept in the closed position so that the downstream pressure could be set to a specified value before the beginning of the test.

At this point, the video equipment was optimally configured for an on-screen capture of potential cavitation. Finally, the run began by opening the valve downstream of the experimental device,

initiating data collection in LabVIEW, and starting the video recorder. For a typical run, the data was collected for 1 minute. For non-cavitating runs, the video was manually stopped during the run. At the end of the run, the LabVIEW program was stopped and the valve downstream of the device was turned off. To begin another test, the tanks were re-pressurized to another set of values specified in the test matrix. Testing continued until the water in the supply tank was exhausted. Then, the dump tank was drained and the procedure was repeated.

At the end of a day of testing, all pressure tanks were fully depressurized and re-pressurized to check the accuracy of the transducers at 50psi. Once this data was gathered, all tanks were depressurized and all flow valves into and out of the experimental device were turned off. Appendix E details the procedures mentioned, as well as the changing of dies and draining of water from the dump tank.

## 4.7 TEST MATRIX AND TEST PLAN

This section briefly explains the test matrix and test plan that was used. The first build of dies was initially run at low pressures and mass flows to check the rig and packaging for leaks. Each subsequent test was run at higher mass flows and inlet pressures, to map out the cavitation design space. Data points were chosen above and below the predicted inception point for a given mass flow from the theoretical cavitation curve predicted in Chapter 2. The pressure drop from the supply tank to the inlet of the die was determined experimentally, such that the data points were determined with an accuracy of 10%.

After running the aforementioned tests, similar tests were repeated at a few points to measure the repeatability. Once the cavitation space for a particular die was determined, tests were preformed in cavitating conditions to measure the decrease of performance. Cavitation zone lengths for a particular inlet pressure and mass flow were observed and used as empirical data for validation of bubble growth theory. Finally, hysteresis tests were performed, which started with dies at cavitating conditions and then slowly decreased the inlet pressure until cavitation disappeared. The next run started at these desident cavitation conditions, and the inlet pressure slowly increased until cavitation started again. The difference in inlet pressure between incipient cavitation and desident cavitation was recorded. The number of runs for each kind of testing depended on the results from the previous tests.

Build #2 cavitation testing proceeded in a similar manner to that of the first build, and was designed to run at higher inlet pressures. Therefore, a larger part of the design space was incorporated. The

inception tests consisted of pressurizing the inlet and outlet pressure to the same pressure, and then slowly decreasing the outlet pressure until cavitation inception occurred. For each die and working fluid, this test was performed from 100psi to 450psi, in increments of 25 to 50psi. Once cavitation inception was observed and recorded, the outlet pressure was further reduced to record data points at different levels of cavitation severity.

Control tests consisted of choosing about 10 points above and below the theoretical cavitation inception curve and running at these points in the test space. These control runs also were used as a basis for the repeatability and hysetersis tests, which were run similarly to that described for the first build. Again, the number of runs for each kind of testing varied depending on the particular die, the previous results obtained from the die, and results obtained from other dies of its kind. For example, once repeatability was established, the number of runs needed for a subsequent die was significantly reduced. An example of a test matrix for build #2 is presented in Figure 4.6.

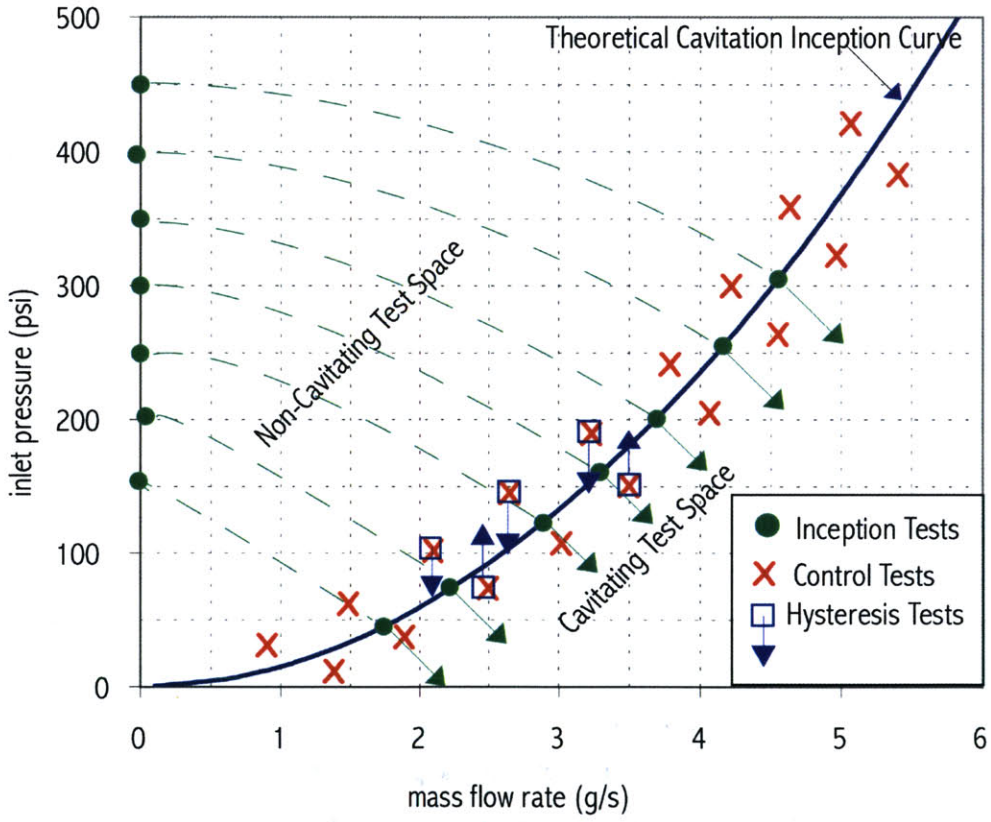


**Figure 4.6 Example of a Build #2 test matrix**

## 4.8 EXPERIMENTAL TESTING OVERVIEW

This section summarizes the tests preformed on every working die, and presents the status of each die after the completion of tests. The first build of dies yielded two ten-die wafers, one of asymmetric cascades and the other of symmetric cascades. During this build, only 11 dies survived the bonding step without delamination. The subsequent build consisted of one ten-die wafer of symmetric dies, and exhibited a much better yield rate of 90%. All tests of the first build were preformed with a working fluid of water, with the exception of two asymmetric dies. Both water and ethanol were used for testing the dies of the second build. Several dies ended up failing during testing, mainly due to Pyrex failure at high pressures.

### 4.8.1 BUILD #1 SYMMETRIC DIES

As depicted in Figure 4.7, 6 dies survived the bond, only one of which was a Symmetric Cascade B. For this reason, the die was not run until the completion of the Symmetric Cascade A testing, by which point the decision was made to fabricate another build of symmetric dies. As a result, the Symmetric Cascade B was not tested.

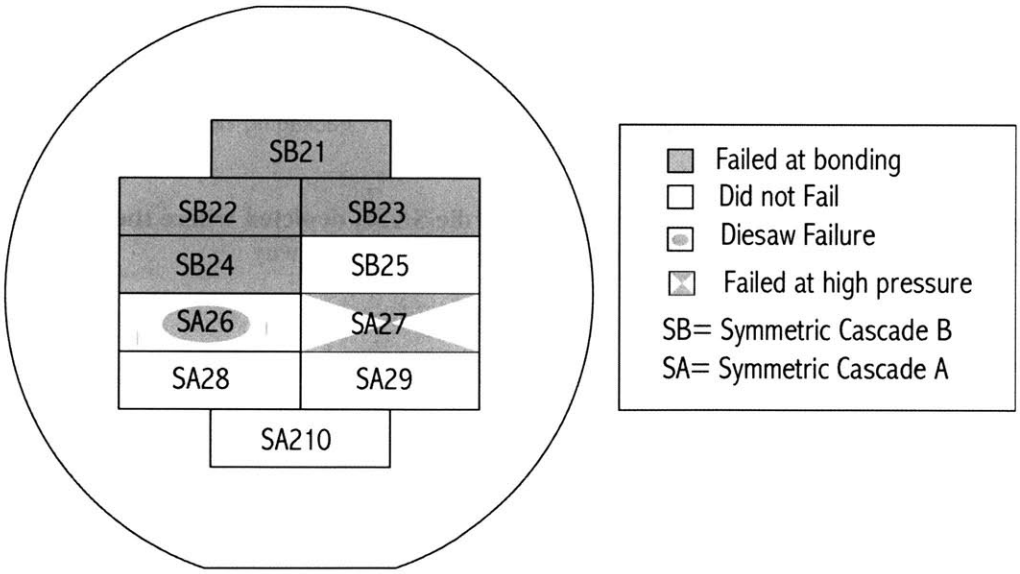


**Figure 4.7 Yield Rate for Symmetric Build #1 Dies.**

During the dies-saw process, die SA26 broke due to the de-bonding of the adjacemt dies. The rest of the cascade A dies were tested initially at low pressures, with gradually increasing inlet pressure for each run. Due to high stress loading on the 500um Pyrex wafer in the large inlet area, a section of the Pyrex of die SA27 broke at an inlet pressure of 138psi. A schematic of the failure of the Pyrex is depicted in Figure 4.8. Due to the fact that SA27 failed at 138psi, the other dies were not run at pressures higher than 112psi. A summary of the runs preformed by each of these dies is presented in Table 4.2.

**Table 4.2 Summary of Build #1 Symmetric Die Testing**

| Die | # of runs | Max inlet P | Approx run time | Working Fluid |
|---|---|---|---|---|
| SA27 | 58 | 138 psi | 200 min | water |
| SA28 | 93 | 93 psi | 300 min | water |
| SA29 | 41 | 112 psi | 180 min | water |
| SA210 | 30 | 90 psi | 120 min | water |

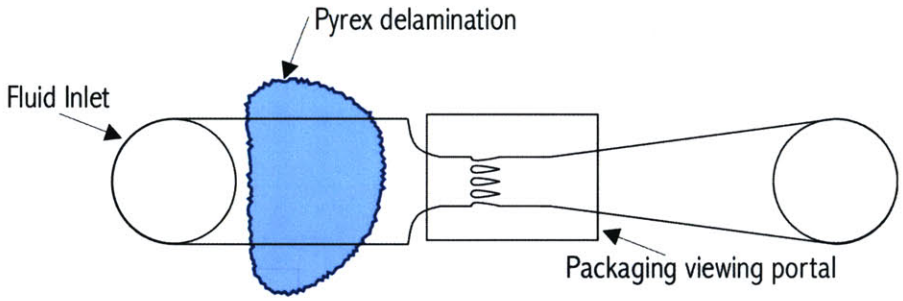


**Figure 4.8 Schematic of Pyrex delamination of die SA27, depicted where the Pyrex layer broke due to high pressure in passageway**

### 4.8.2 ASYMMETRIC DIES

Only 5 asymmetric dies bonded correctly, as depicted in Figure 4.9. Similar to the symmetric die SA27, delamination of the Pyrex from the silicon wafer of die AE26 occurred when the pressure in the passageway increased beyond 70psi. Due to this, dies AE28, AE29, and AE210 were modified to run at higher pressures. A 3 mm Pyrex wafer was attached to both AE28 and AE210. Loctite 401 was used on AE28, while Loctite 330 was used on AE210. Anonic bonding of 1mm thick silicon pieces to the top Pyrex wafer (leaving space for proper viewing of the cascade) was attempted on AE29, but the bond failed. Running AE28 and AE210 at higher pressure were successful only to about 200psi,

where both dies experienced a failure at the Pyrex-Pyrex interface. These two dies also were tested with ethanol, to see the effects of cavitation with another working fluid, and to compare to symmetric die results from build #2, which also incorporated ethanol in testing. Table 4.3 summarizes the tests performed on each working die.

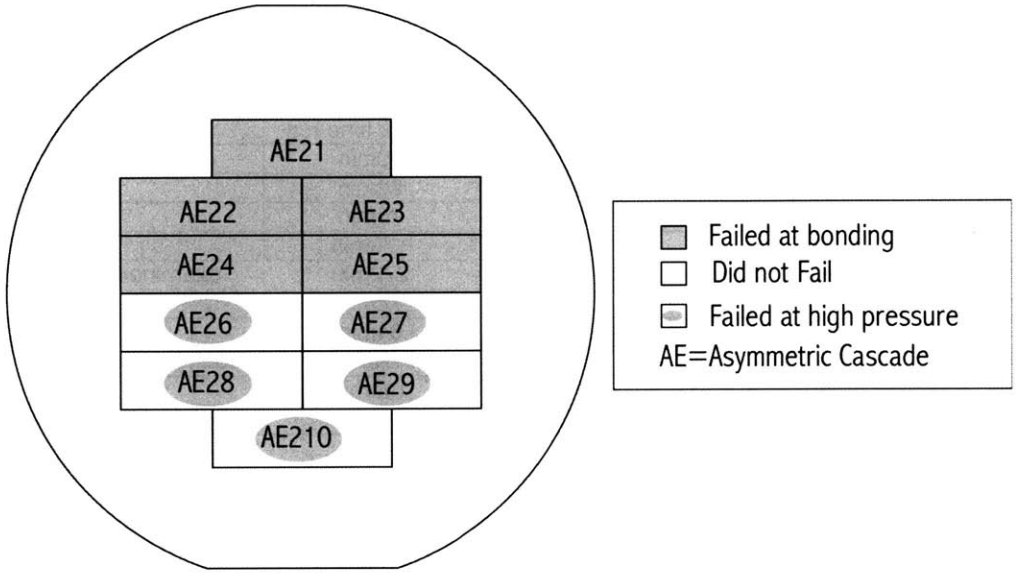


**Figure 4.9 Yield Rate for Asymmetric Dies**

**Table 4.3 Summary of Asymmetric Die Testing**

| Die | # of runs | Max inlet P | Approx run time | Working Fluid |
|---|---|---|---|---|
| AE26 | 7 | 73 psi | 38 min | water |
| AE27 | 30 | 84 psi | 93 min | water |
| AE28 | 38/42 | 106/200 psi | 250 min | water/ethanol |
| AE29 | 26 | 92 psi | 52 min | water |
| AE210 | 0/64 | 0/170 psi | 49 min | water/ethanol |

### 4.8.3 BUILD #2 DIES

The second build of cavitation devices resulted in an excellent yield. Only one die failed during bonding, giving a 90% success rate. Figure 4.10 shows the yield rate and labelling scheme for the build #2 dies. This build had a 3mm Pyrex layer anonically bonded to the silicon wafers, so that it could operate at higher pressures. Therefore, none of the dies failed due to Pyrex failure at high pressures. All dies except two were tested using both water and ethanol over the complete test space. Die AN1 and BN8 were used to evaluate cavitation damage due to erosion. Die AN1 was run at the

conditions that a turbopump may experience when cavitating, for the amount of time that a microturbopump would be theoretically utilized [12]. After the run, the die was examined under a microscope to evaluate the cavitation erosion damage. Die BN8 was not run and used as a control for the test. The most extensively tested die, AH5, was also ground and examined after testing to determine damage after severe cavitation exposure. Table 4.4 summarizes build #2 testing.

**Table 4.4 Summary of Symmetric Build #2 Die Testing**

| Die | # of water runs | # of ethanol runs | Approx time run | Comments |
|---|---|---|---|---|
| AN1 | 1 | - | 20min | erosion test |
| AN2 | 54 | 20 | 99min | |
| AH3 | 21 | 32 | 78min | |
| AN4 | 78 | 70 | 179min | |
| AH5 | 84 | 48 | 272min | examined after run |
| BN6 | 32 | 38 | 72min | |
| BH7 | 17 | 20 | 64min | |
| BN8 | N/A | N/A | N/A | control for erosion test |
| BH9 | 30 | 34 | 120min | |
| BN10 | N/A | N/A | N/A | bonding failure |

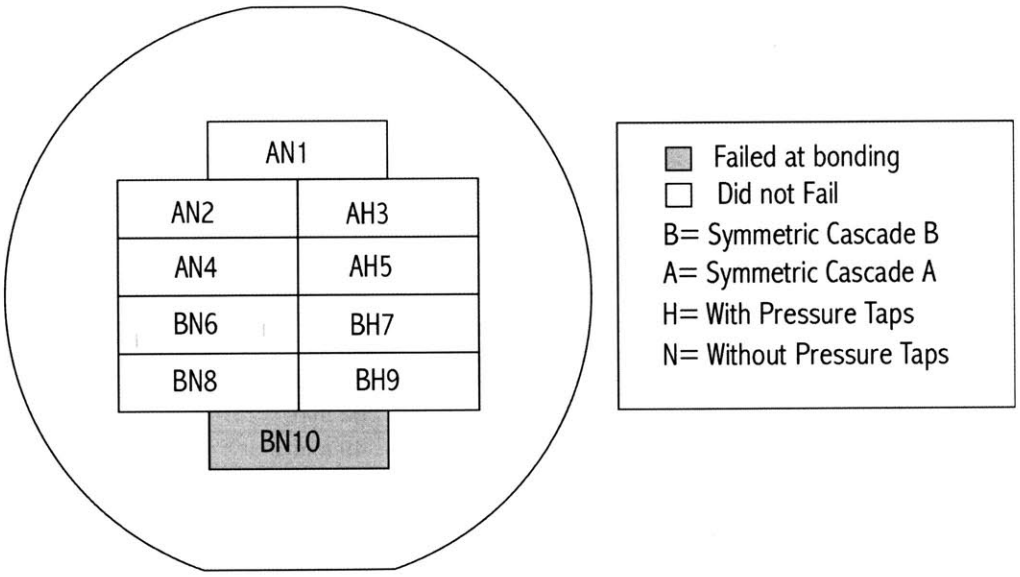


**Figure 4.10 Yield Rate and Naming Scheme for Symmetric Build #2 Dies**

## 4.9 CHAPTER SUMMARY

This chapter discussed the experimental setup and testing for a cavitation device and experiment. Packaging and the experimental rig for the finished device were designed to deliver pressure to the blades at a specified mass flow rate. Calibration and experimental uncertainty were discussed. The procedure for generating a test run was described, and the test plan was presented. Finally, a summary of the testing performed on each working die was summarized. The next chapter discusses the device experimental results and the impact of these results on micro-scale turbopump blade cavitation.

# 5 RESULTS AND DISCUSSION

## 5.1 INTRODUCTION

This chapter presents the results from the experimental phase of the research. Two builds of devices were tested during this phase. Visual observances, repeatability curves, and CFD validation is presented for all the cascade devices of both builds. Performance impacts of cavitation on micro-scale devices are discussed and correlations between results and macro-scale empirical data are presented.

These experimental results provide useful information regarding the cavitation phenomenon of micro-scale turbopumps. Experimental data combined with the theoretical modeling of Section 2.4 is then used to determine the performance loss associated with micro-turbopumps operating at cavitating conditions. Finally, the design criteria for micro-turbopumps are defined.

## 5.2 BUILD #1 SYMMETRIC DIE RESULTS

This section presents the results of the first build of symmetric dies. For this build, water was the working fluid. First, the existence of cavitation on a micro-scale was verified by visual observations as defined and described in Section 5.2.1. Next, points with and without cavitation are plotted against the macro-scale theoretical cavitation inception curve, showing that micro-scale cavitation inception occurs along the curve macro-scale theory predicts. The established repeatability of the test results for multiple dies is used to validate the results in Section 5.2.2. Finally, Section 5.2.3 compares inital 3D CFD models to the test results to assess the utility of a CFD flow solver as a design tool.

### 5.2.1 VISUAL OBSERVATIONS

Cavitation in a micro-scale was visually observed during the first set of tests. Cavitation inception is defined in Chapter 2 as the point where vapor bubbles begin to form in the liquid flow. In terms of the

tested device, cavitation inception is defined as when the first sign of vapor bubbles is observed in the blade passages. Figure 5.1 shows an example of observed cavitation inception.

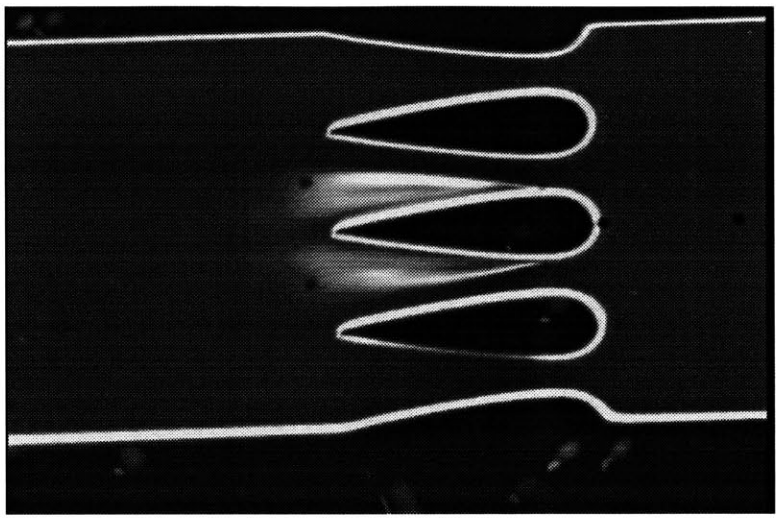

**Figure 5.1 Cavitation inception of build # 1 symmetric die. Note cavitation inception starts at pressure taps.**

Referring to the definitions of Section 2.1, examples of partial cavitation and super cavitation are given in Figure 5.2. For purposes of this experiment, flow with a cavitating zone of one blade length or less was defined as partially cavitating, and flow with a cavitating zone longer than the blade length was identified as super cavitating. Further discussion of cavitation zone data is presented in Section 5.5.

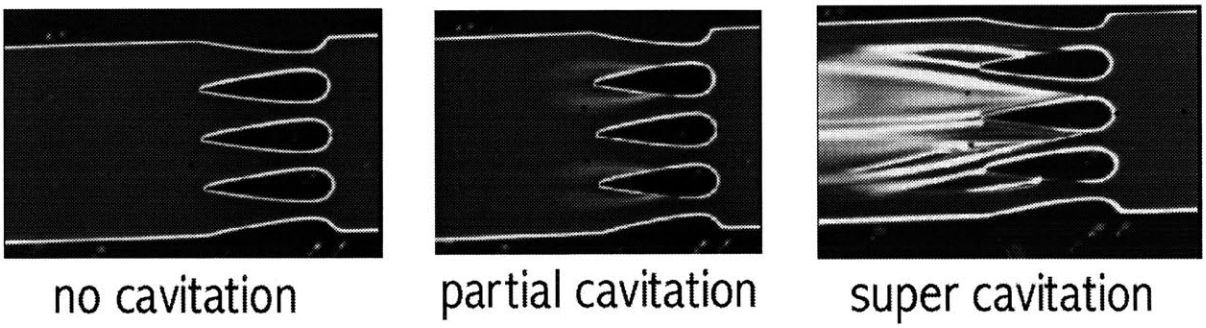


**Figure 5.2 Definitions of visually observed cavitation phenomena on micro-scale blades**

These figures show cavitation exists on a micro-scale. In order to determine when cavitation occurs, inlet pressures and mass flow rates were recoded at cavitation inception, then plotted along with the

macro-scale theoretical cavitation curve presented in Chapter 2. For the purposes of simplicity, cavitation zone lengths were not taken into account, only distinctions between the previously defined partial, super, and no cavitation of Figure 5.2. The theoretical cavitation curve is plotted against all of the build #1 data points in Figure 5.3. From the figure, it is apparent that micro-scale cavitation inception occurs reasonably close to that predicted by macro-scale data. Specifically, when a ~5% experimental error is considered, 95% of the inception data lies on the theoretical inception curve.

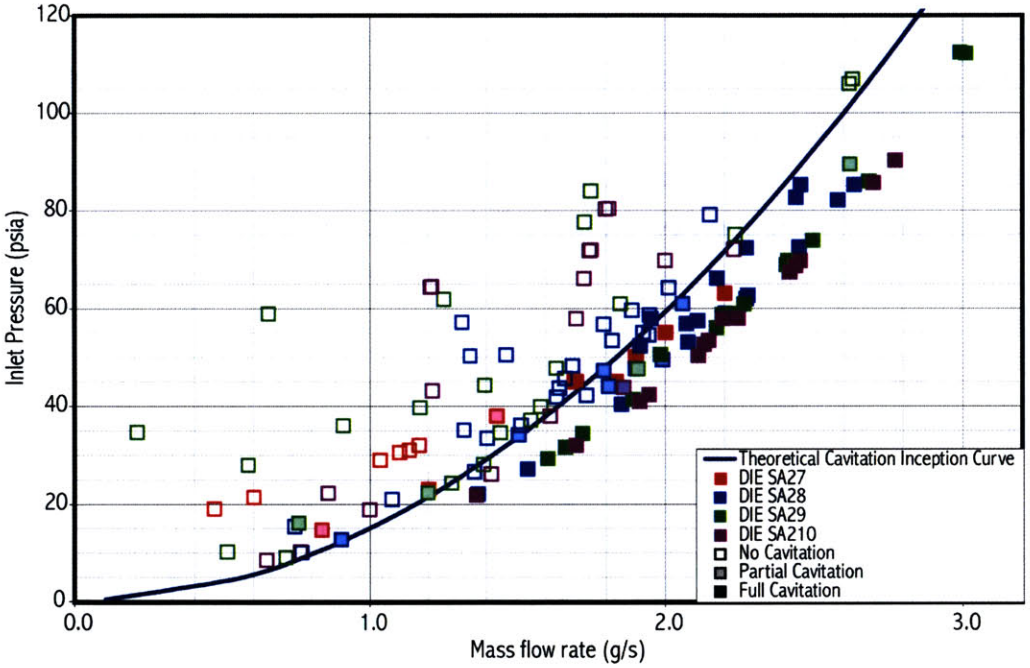


**Figure 5.3 Cavitation inception curve for build #1 working symmetric devices**

Cavitation hysteresis was also examined during testing. Desident cavitation was found to consistently occur at a higher inlet pressure than incipient cavitation. However, the desident point highly varied depending on the state of the initial cavitation. This occurrence is similar to that at macro-scale, as described in Section 2.1. Another observation made was the unsteadiness of the flow during cavitation. As in the macro-scale, traveling partial cavitation was noticed to jump from one blade arbitrarily. For certain cavitating runs, there was a time lag before the onset of cavitation. This lag was on the order of 1 second to 1 minute. Also during some runs, partial cavitation changed suddenly to super cavitation without any change in inlet conditions.

As depicted in Figure 5.1, cavitation inception appeared to start mainly at the pressure taps that had been placed at the minimum pressure point along the blade. Whereas, comparing Figure 5.1 to the partial cavitation of Figure 5.2 , the cavitation of the latter case starts downstream of the pressure taps. This observation suggests that the pressure taps encourage cavitation to start earlier than it would have had the taps not been present. This hypothesis was verified in a second build without pressure taps.

### 5.2.2 REPEATABILITY

Figure 5.4 plots repeatability measurements of 4 runs using the same die at the same conditions, and Figure 5.5 displays the repeatability of 3 different non-cavitating dies. The results agree within the 5% experimental uncertainty calculated in Section 4.5 and establish repeatability of the measurements of the first build of symmetric dies. Cavitating dies exhibited much poorer reproducability, due to the unstable readings of pressure measurements in cavitating flows, and will be further quantified in Section 5.4.2.

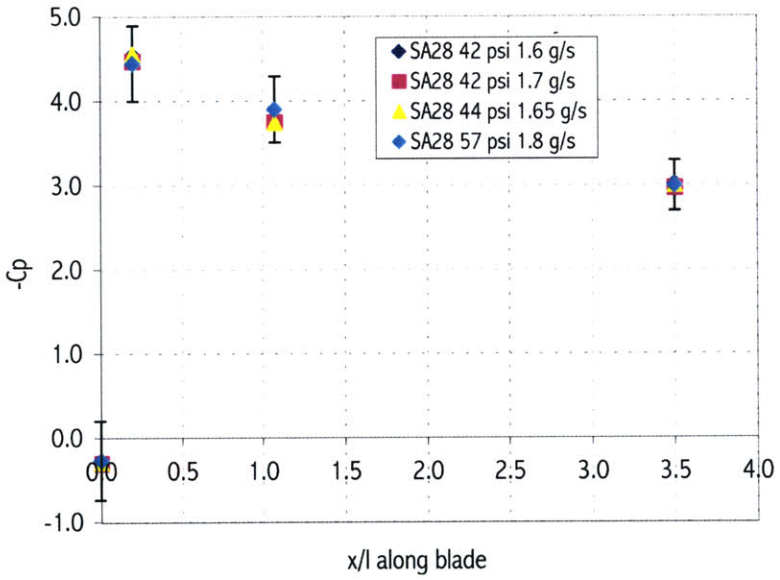


**Figure 5.4 Repeatability of a single die for the first build of symmetric cascades**

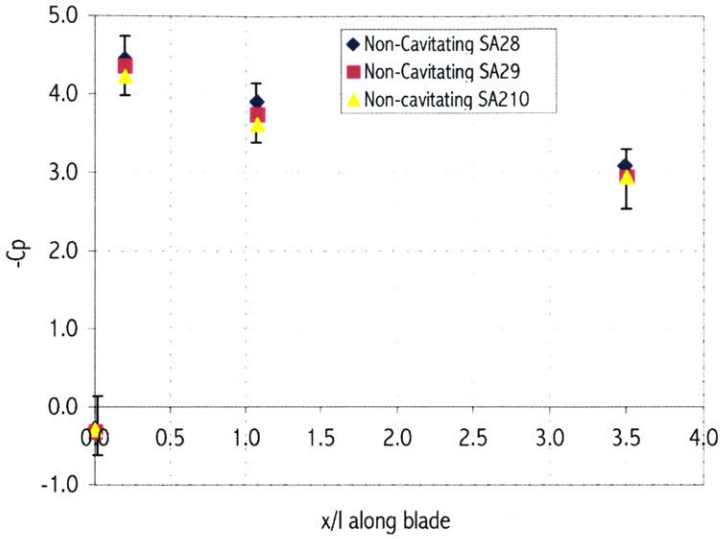


**Figure 5.5 Die to Die repeatability of the first build of symmetric cascades**

### 5.2.3 INITIAL CFD VALIDATION

As explained in Section 3.4 and Appendix A, the results of a 3D FLUENT model of the symmetric cascade A compared with empirical data and to verify the CFD code. The design inlet values were used for the initial model and plotted against non-dimensionalized pressure measurements of 13 non-cavitation experiments. The 3D laminar solution best matched the initial experimental data, and resulted in values within the 5% error bars of the data, as shown in Figure 5.6. These initial modeling results were then used to construct finer grids with inlet conditions corresponding to actual experimental run conditions of the second build, as discussed further in Section 5.4.3.

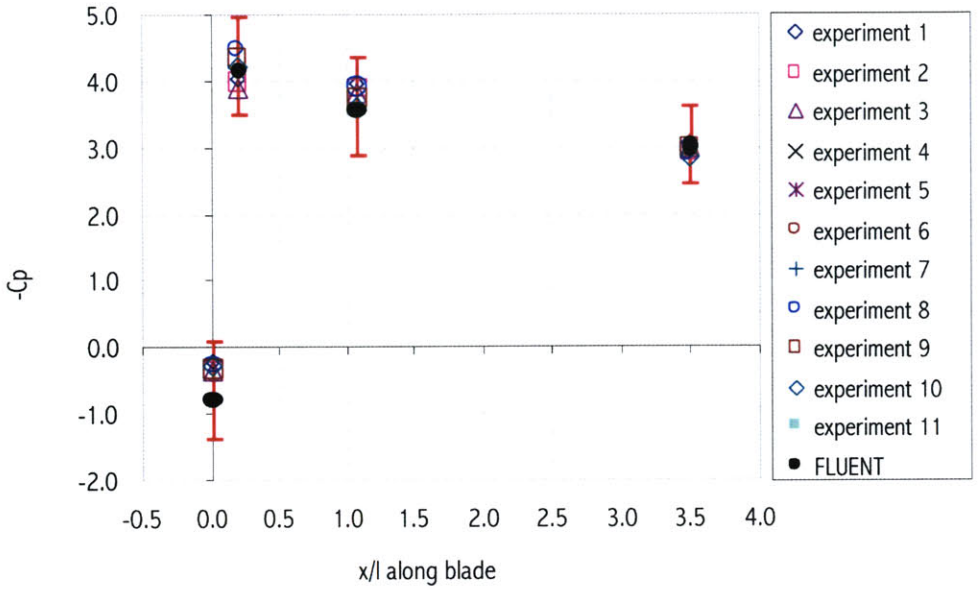


**Figure 5.6 Initial CFD validation for non cavitating dies**

### 5.2.4 CONCLUSIONS

The testing of the first build of symmetric airfoils provided valuable results for analysis. Although only 4 dies were tested, the tests proved that cavitation did occur, and that the cavitation followed the same trends as that observed on a macro-scale. This agreement included inception points, time lag, and hysteresis. Cavitation zone length data was recorded for use in theoretical modeling, and will be decribed further in Section 5.5. In addition, the tests established repeatability of experimental measurements and validated computational fluid dynamic modeling. This modeling is used as a benchmark for further CFD models.

However, the build did not provide a comprehensive set of data needed to fully study the micro-scale cavitation phenomenon. The one functional symmetric B cascade device was not tested, therefore the effects of added blades were unknown. The role of pressure taps in inducing cavitation was not determined. The Pyrex failure of die SA26 at 138psi did not allow for runs above 112psi. To analyze cavitation in the main turbopump design space, higher inlet pressures and corresponding mass flows were required. This prompted the fabrication of a new build without pressure taps and with a thicker layer of Pyrex. Adding 2.5mm of Pyrex to the die enabled the die to handle up to 500psi in the flow channel. The repeatability established from the first build justified fabricating the second build both

with and without pressure taps. Then, pressure results from a die with taps could be applied to one without taps for the same inlet pressure and mass flow rate. The new build allowed for testing of symmetric B cascades, to examine the effect of added blades. The results from the second build are presented in Section 5.4.

## 5.3 ASYMMETRIC DIE RESULTS

This section examines the results obtained from the asymmetric dies. Section 5.3.1 summarizes the experimental cavitation results obtained from all the dies, Section 5.3.2 discusses the repeatability of the dies, Section 5.3.3 compares experimental data to CFD models, and Section 5.3.4 recapitulates conclusions gathered from the testing of the asymmetric dies.

### 5.3.1 EXPERIMENTAL RESULTS

As mentioned in Section 4.8.2, only 5 dies survived the bonding. First, 4 dies were tested over the design space and produced no cavitation. This is due to the fact that the asymmetric pressure profile exhibits a small $-C_{pmin}$, which restricts cavitating conditions at low inlet pressures and high mass flow rates. The pressure drop from the supply tank to the dump tank of the experimental rig was not a large enough to achieve the high mass flow rate needed for a given inlet pressure. Applying a vacuum to the dump tank to raise inlet pressures resulted in breaking the Pyrex of the five dies. To reinforce the dies, 3mm Pyrex was glued to two dies and 1mm silicon was anonically bonded to the remaining die to allow for the die to run at higher pressures. The anonic bond failed, but the other two dies were successfully glued, and allowed higher mass flow rates. However, at higher inlet pressures, the pressure drop still was not large enough to produce significant cavitation. Only 3 runs were observed to have partial cavitation, mainly due to unsteady bubble pockets forming from the pressure taps. Since ethanol is less dense than water, the theoretical cavitation curve is lower for this fluid, making cavitation more difficult to achieve. Figure 5.7 and Figure 5.8 show the empirical results plotted against the theoretical cavitation curve for water and ethanol.

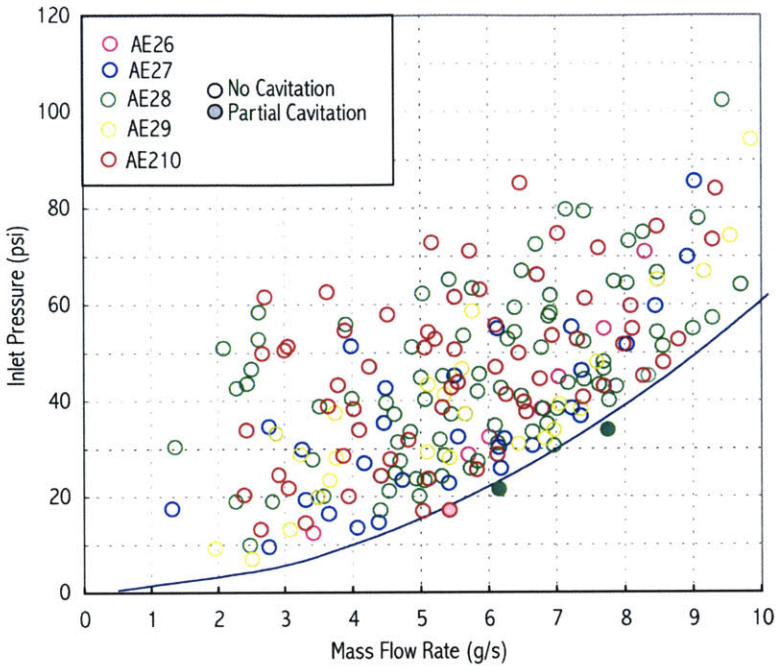


**Figure 5.7 Asymmetric cascade theoretical cavitation inception curve plotted against experimental data for water**

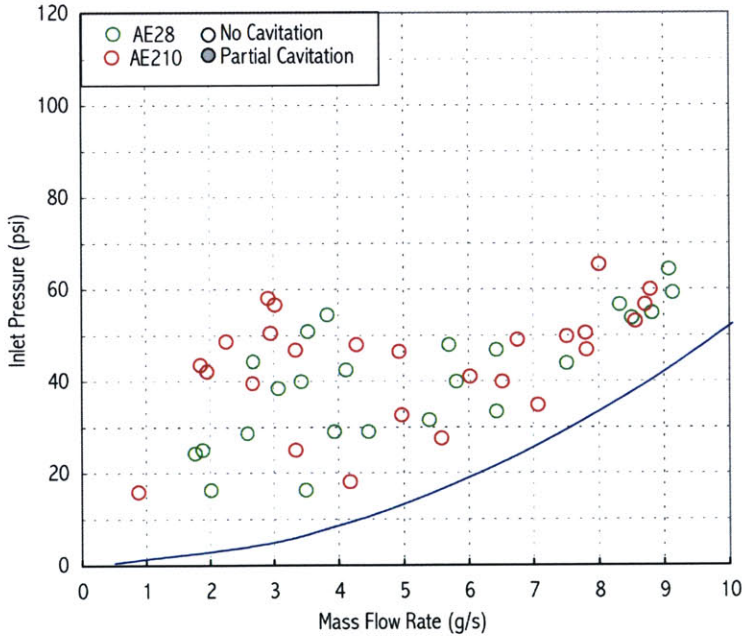


**Figure 5.8 Asymmetric cascade theoretical cavitation inception curve plotted against experimental data for ethanol**

### 5.3.2 ASYMMETRIC DIE REPEATABILITY

Although asymmetric testing did not cavitate, it did confirm repeatability. Figure 5.10 and Figure 5.11 show repeatability of one die at similar conditions and die to die repeatability of non-dimensionalized pressure readings, using the pressure tap locations as indicated in Figure 5.9. The results are shown to be within experimental uncertainty and thus establish repeatability of the asymmetric die pressure measurements.

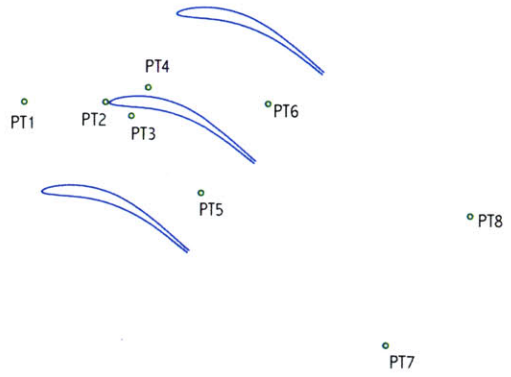


**Figure 5.9 Location of pressure taps along asymmetric blade**

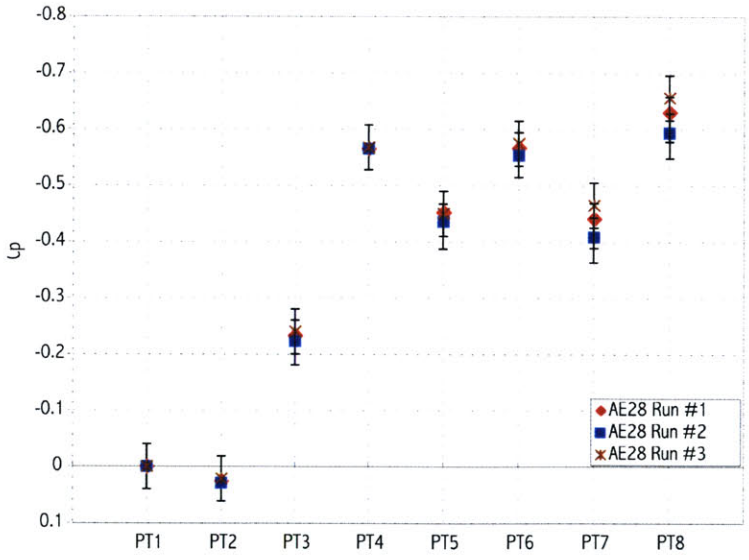


**Figure 5.10 Repeatability for three runs of asymmetric die SA28.**

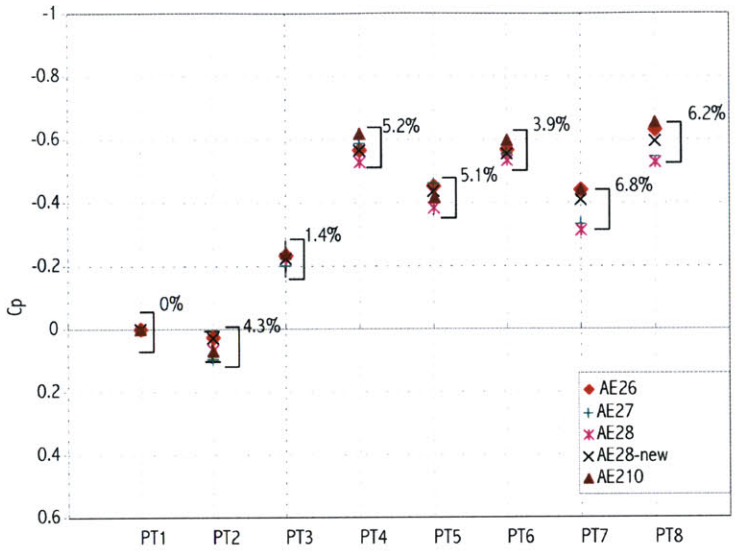


**Figure 5.11 Die to die repeatability for asymmetric devices.**

### 5.3.3 FLUENT VALIDATION EFFORTS

Asymmetric test data was used to determine the utility of 3D FLUENT as a design tool. Once a grid was generated from the initial CFD validation (Section 5.2.3), the model was used to simulate the inlet conditions corresponding to experimental data. Table 5.1 summarizes two models using water and ethanol respectively. Inlet conditions of analogous experimental runs are also shown. Experimental pressure readings were then compared to pressures at the same location on the model and plotted in Figure 5.12 and Figure 5.13 for water and ethanol respectively. In addition, a FLUENT model was constructed for water at microturbopump design inlet conditions and the non-dimensionalized pressure coefficients were compared to 5 different dies at about the same conditions, as depicted in Figure 5.14. All calculational results proved to be within 5% experimental uncertainty.

**Table 5.1 FLUENT modeling inputs along with corresponding inlet conditions for asymmetric dies**

| Run | Inlet pressure | Inlet velocity | Mass flow |
|---|---|---|---|
| Water Experiment | 46.622 psi | 3.1156 m/s | 14.20 g/s |
| Water CFD | 45.449 psi | 2.9924 m/s | 13.456 g/s |
| Ethanol Experiment | 47.715 psi | 2.22 m/s | 10.124 g/s |
| Ethanol CFD | 48.028 psi | 2.435 m/s | 10.245 g/s |

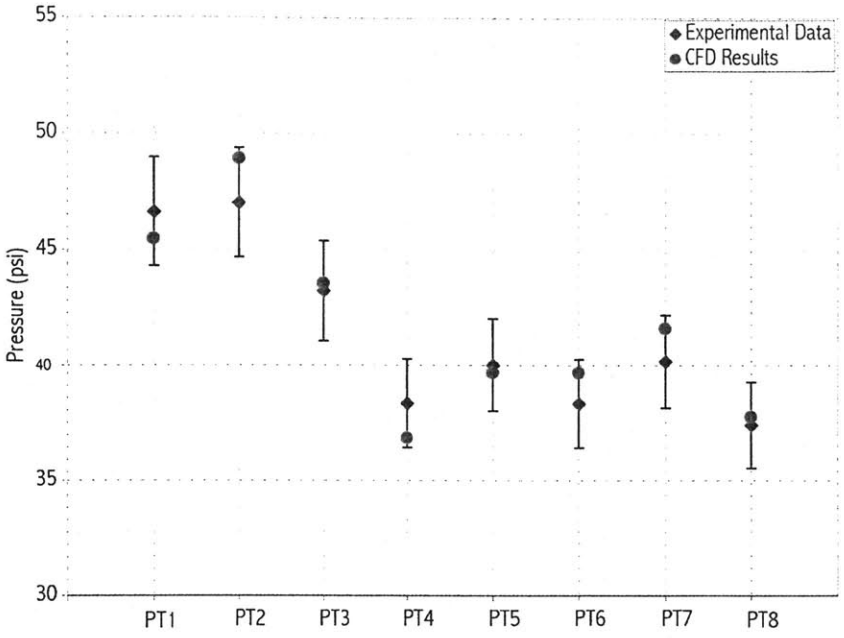


**Figure 5.12 CFD validation for a working fluid of water**

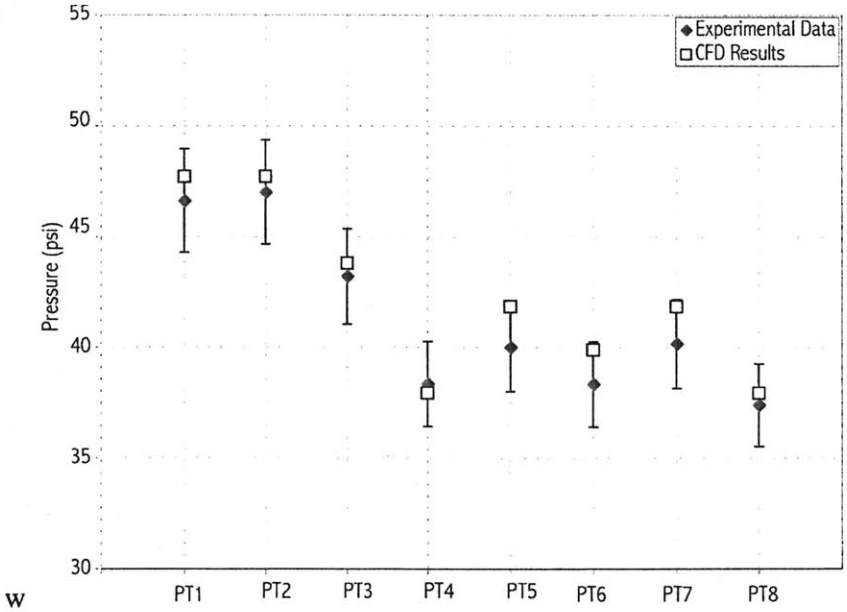


w

**Figure 5.13 CFD validation against ethanol run- falling within 5% experimental uncertainty for pressure data**

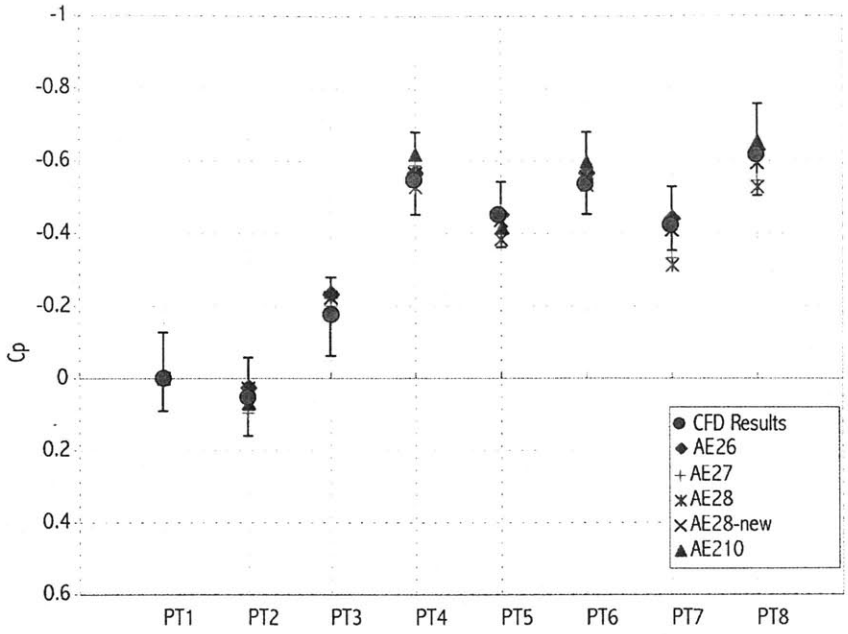


**Figure 5.14 Non-dimensionalized CFD results plotted against experimental data**

### 5.3.4 ASYMMETRIC DIE TESTING CONCLUSIONS

Small $-C_{pmin}$ and large flow area of the cascade, made creating conditions for cavitation difficult. Only 3 runs out of over 200 tests exhibited signs of partial cavitation from the pressure taps. It was decided that asymmetric dies would not be included in the fabrication of the second build, since they would not be useful in the characterization of micro-scale cavitation.

The asymmetric test runs did prove useful in the validation of FLUENT. Die repeatability was shown to be within experimental uncertainty. These runs confirmed FLUENT as a viable flow solver for both water and ethanol.

## 5.4 BUILD #2 RESULTS

This section presents results from testing the second build of devices. This build consisted of the same cascade geometries as the first build of symmetric devices. However, half the dies were fabricated without pressure taps at the minimum cavitation point in order to examine the role of pressure taps on cavitation inception. Thicker Pyrex was used to permit higher pressure experiments. In addition to water, this build tested ethanol. First, visual observations for the second build are described in Section

5.4.1, suggesting that pressure taps induce cavitation inception. Cavitation inception charts are plotted for both working fluids and cascade geometries. Observed cavitation phenomenon such as time lag and hysteresis are discussed. Next, repeatability of this build of dies is confirmed in Section 5.4.2, with further discussion on cavitating repeatability. Finally, computation validation efforts for both non-cavitating and cavitating runs are summarized in Section 5.4.3.

### 5.4.1 VISUAL OBSERVATIONS

Observations of cavitation in symmetric cascades were similar to those described in Section 5.2.1. However, there were noticeable differences between cavitation of dies with pressure taps and dies without pressure taps. As depicted in Figure 5.15, partial cavitation of a die with pressure taps appeared to initiate from the pressure taps, and cavitation was more severe around this blade. However, the die without pressure taps cavitated in a more uniform manner on all three blades. In addition, cavitation of the device with pressure taps appears to start at the pressure taps, whereas for the device without pressure inception appears to occur downstream of the pressure tap location. These observations suggest that the pressure taps initiated cavitation. The point where cavitation occurred on the dies without taps appeared to be within the region of the laminar separation point. As described in Section 2.3.3.3, the blade designs have a laminar separation point and corresponding turbulent reattachment around x/l=0.5. Therefore, this flow discontinuity may instigate cavitation[31]. Further analysis of this subject extends beyond the scope of this thesis and will be recommended for future work.

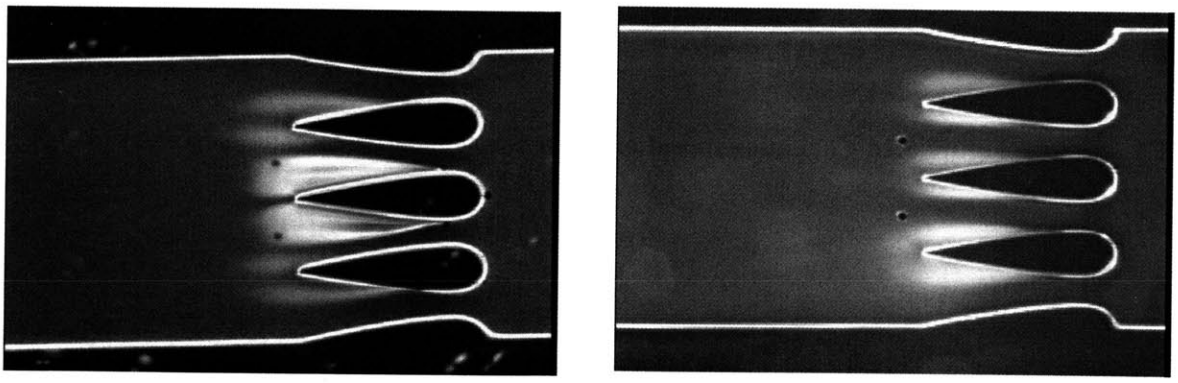

**Figure 5.15 Partial cavitation for dies with and without taps**

For a given mass flow, the cavitation inception point was observed to occur at a lower inlet pressure without pressure taps than with pressure taps. This can be seen in Figure 5.16, which plots data from dies with and without pressure taps along the theoretical cavitation curve for the symmetric cascade A. Running the dies with ethanol produced similar results as water. However, the cavitation inception point appeared to be consistently lower than the theoretical curve, as depicted in Figure 5.17. Figure 5.18 compares the cavitation inception data for both water and ethanol. From the figure, it appears that the results for ethanol were more consistent than water. This may be due to the fact that the testing procedure for ethanol was more refined than for water, producing more consistent results.

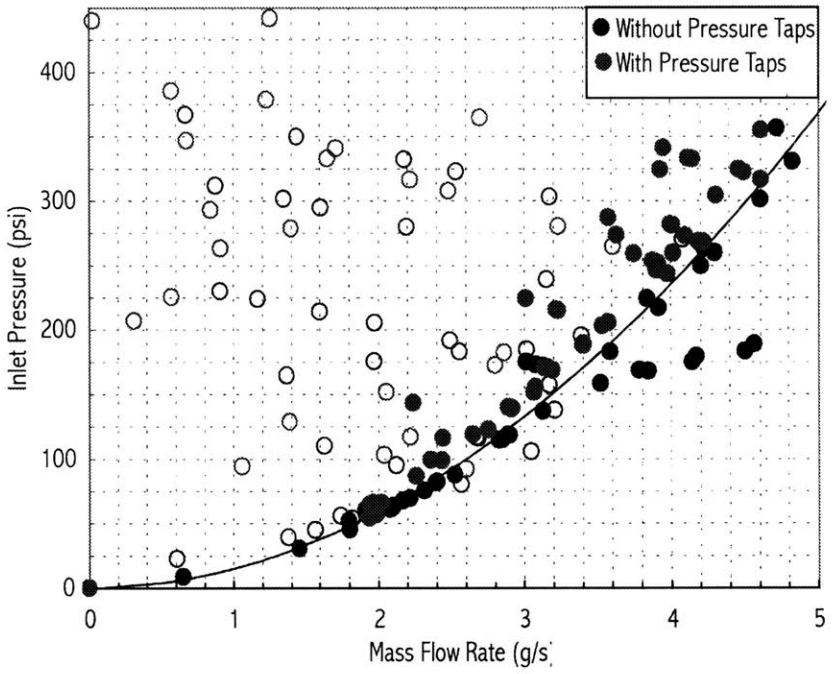


**Figure 5.16 Cavitation inception curve for symmetric cascade A (water)**

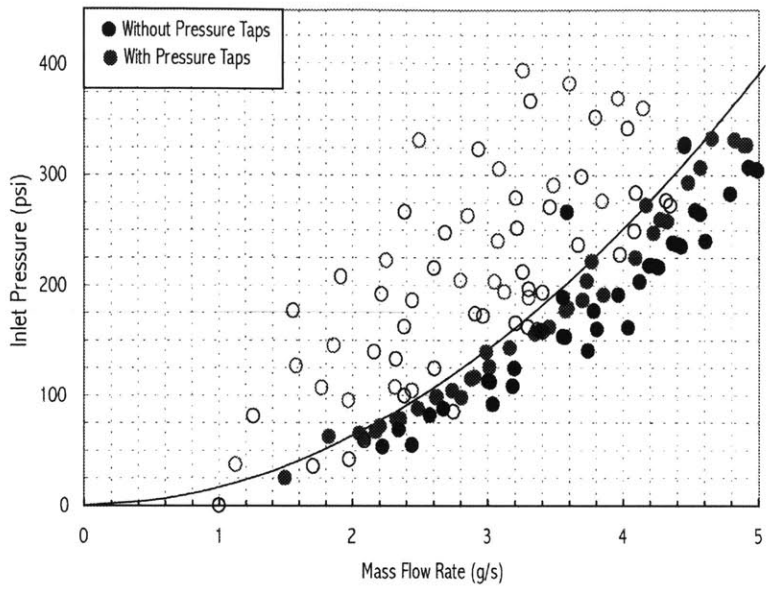


**Figure 5.17 Cavitation inception curve for symmetric cascade A (ethanol)**

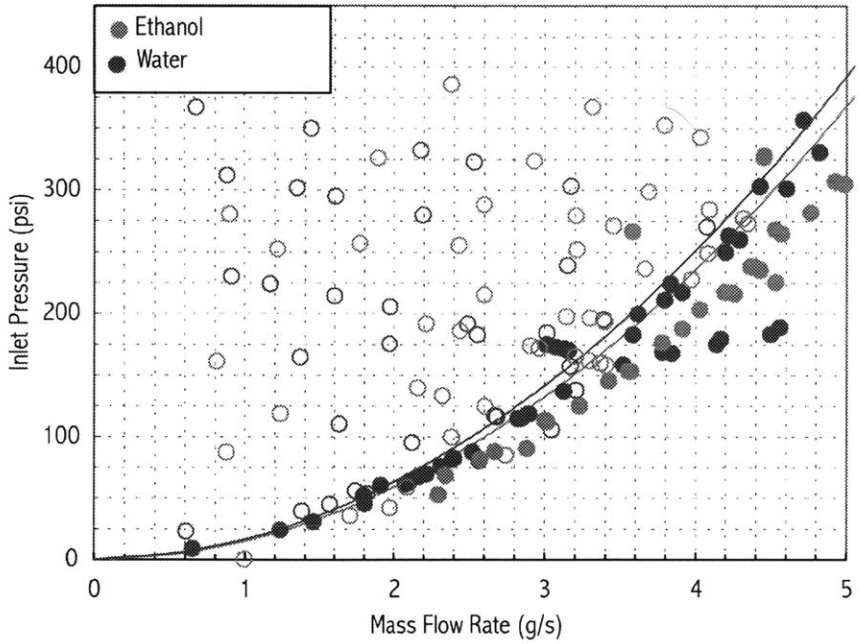


**Figure 5.18 Comparisons of water and ethanol for Symmetric cascade A**

The second build of dies allowed for proper testing of the symmetric B cascades. These cascades were fabricated to examine the effect of added blades on cavitation. From visual observations, it was noted that, like the symmetric cascade devices, cavitation started mainly from the pressure taps. In the runs without pressure taps, cavitation mainly occurred from the three blades in the middle of the device passageway. These results suggest that the point of minimum pressure is at the middle of the passageway, as opposed to the endwalls. Numerical modeling presented in Section 5.4.3 validates this theory. Extensive cavitation of the symmetric B cascade passageways was not achieved due to the high mass flow rates and pressure drops required to create the conditions for super cavitation. Testing with ethanol produced similar results as those with the symmetric cascade A, with the inception points being consistently lower than the theoretical inception curve. Cavitation inception results for water and ethanol are displayed in Figure 5.19 and Figure 5.20, respectively.

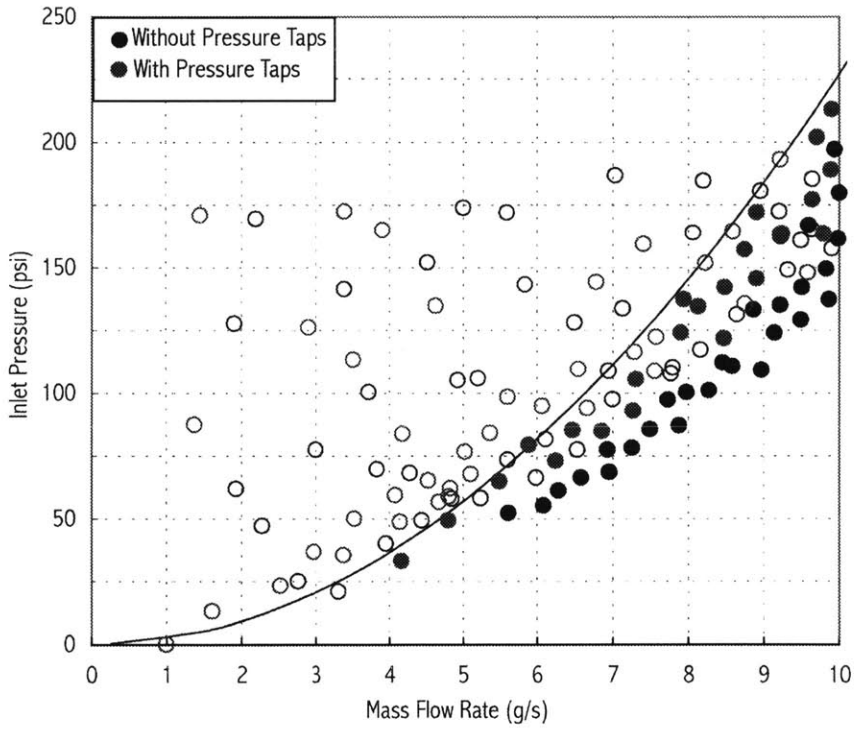


**Figure 5.19 Cavitation inception curve for Symmetric Cascade B (water)**

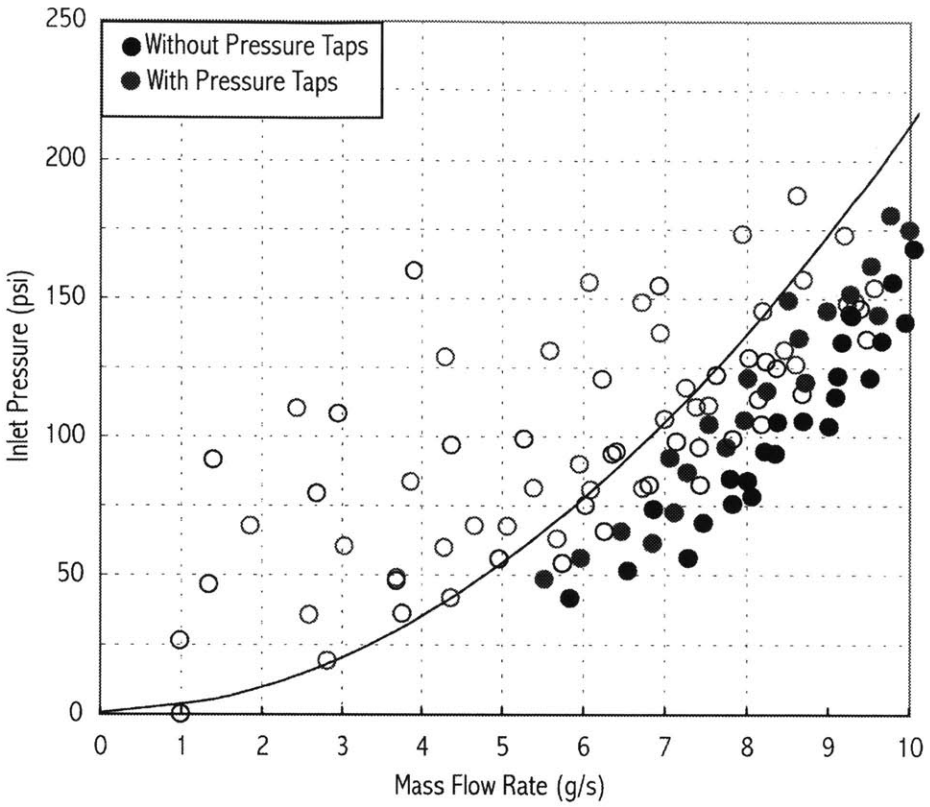


**Figure 5.20 Cavitation inception curve for Symmetric Cascade B (ethanol)**

As in testing of the first build, cavitation hysteresis was observed in build #2. However, for this set of runs, efforts were made to further quantify this hysteresis (as described in Section 4.8.3). Once an incipient cavitation point was found for a particular mass flow, the inlet pressure was decreased to a predetermined extent of cavitation. Once the cavitation zone was visually observed and recorded, the inlet pressure was slowly increased to find the pressure where the cavitation disappeared, the desident cavitation point. The same test was then repeated at the same inlet pressure for varying extents of cavitation. The desident cavitation point always occurred at a higher inlet pressure than the inception point, and appeared to vary with the extent of cavitation the cascade was brought to after inception. An example of hysteresis test results is displayed in Table 5.2 for symmetric cascade A and a working fluid of water, around the design cavitation value of the main turbopump. The results from the table suggest that the $\Delta p$ required to eliminate cavitation increases as the extent of cavitation increases. Further hysteresis test results are presented in Appendix G.

**Table 5.2 Example of Hysteresis Results at Design Values**

| Inception Pressure | Mass Flow | Nondimensionalized zone length | Desident Pressure |
|---|---|---|---|
| 100psi | 2.5 g/s | 0.5 | 103psi |
| | | 1.0 | 115psi |
| | | 1.5 | 128psi |

Lastly, a time lag was observed during this build of testing, as observed with the first build of symmetric devices. When testing at cavitating conditions, sometimes a device would experience a time lag of up to a minute before cavitation started, with no change in inlet pressure or mass flow. However, this lag occurred randomly and therefore was difficult to quantify. Also, it was observed that this time lag was more prevalent on both the dies without pressure taps, and the dies that have not been run extensively. These observations further suggest that cavitation is initiated by perturbations in the flow field, such as pressure taps, the laminar separation point, and/or contaminants the flow field that might have accumulated after numerous runs.

### 5.4.2 REPEATABILITY OF TEST RESULTS

This section presents the repeatability of the test results for both non-cavitating and cavitating test runs. Figure 5.22 and Figure 5.23 show repeatability of one die at similar conditions and die to die repeatability of non-dimensionalized pressure readings, using the pressure tap locations as indicated in Figure 5.21. Table 5.3 summarizes the repeatability of non-cavitating results for all the cascade geometries and working fluids of the second build. The non-cavitating results are within the experimental uncertainty and establish the repeatability of the pressure measurements.

**Table 5.3 Repeatability Results for Non-Cavitating Build #2 Dies**

| Cascade Geometry | Working Fluid | Repeatability Results | |
|---|---|---|---|
| | | Within Die | Die to Die |
| Symmetric cascade A | Water | 4.5% | 6.2% |
| | Ethanol | 5.1% | 4.8% |
| Symmetric Cascade B | Water | 4.3% | 4.5% |
| | Ethanol | 4.6% | 3.9% |

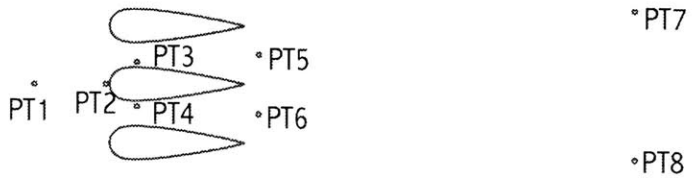


**Figure 5.21 Location of pressure taps along symmetric blade**

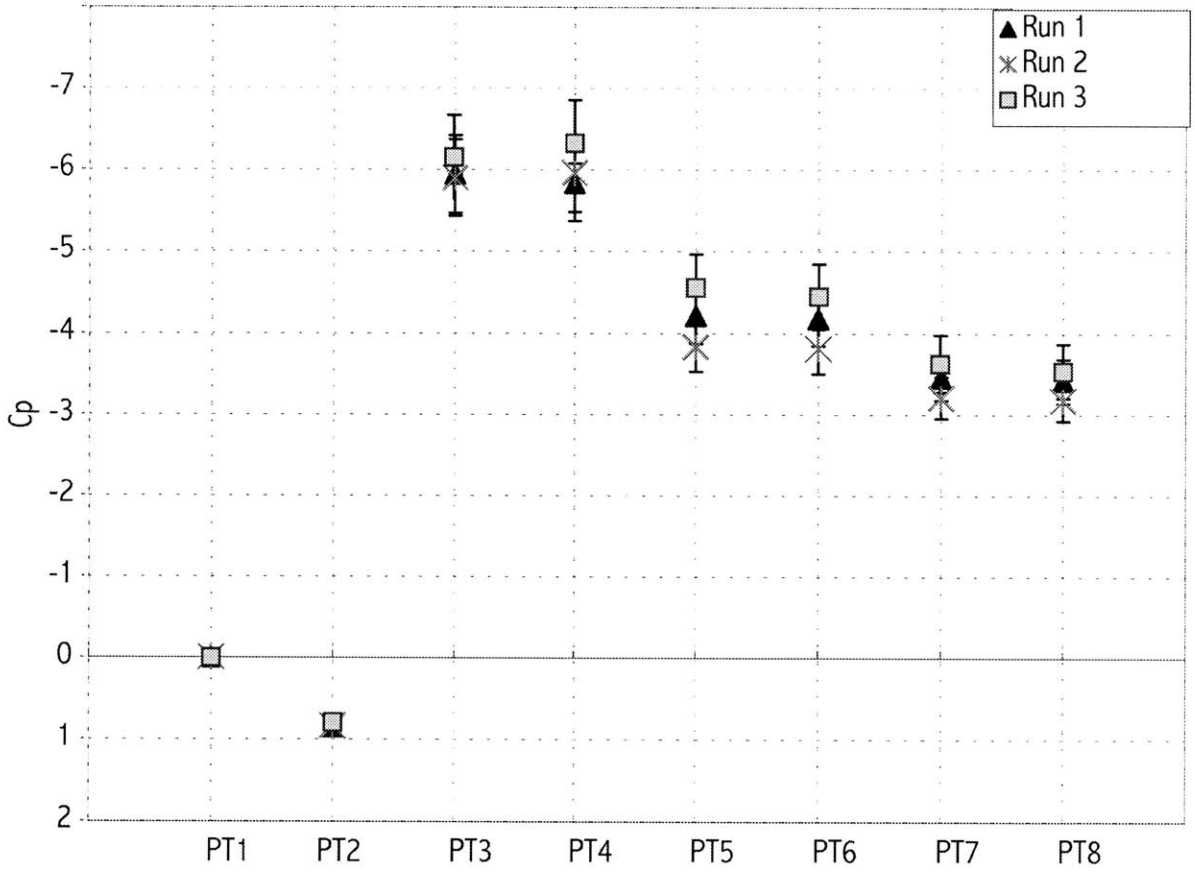


**Figure 5.22 Repeatability of three run of die AH5**

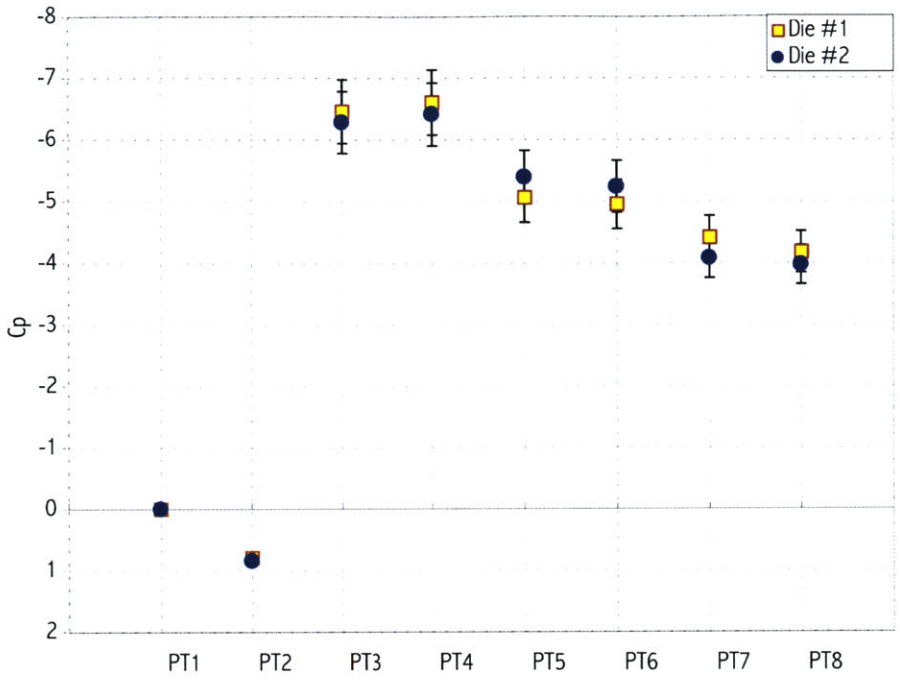


**Figure 5.23 Die to Die repeatability for symmetric A cascades**

Cavitating results, however, did not exhibit the repeatability of non-cavitating runs. This was due in part to the unsteadiness of the results, the time lag, and hysteresis phenomena discussed in the prior section. Unsteady pressure readings at the minimum cavitation point where the fluid is changing phase also contribute to large discrepancies of repeatability. Repeatability results of pressure readings for the second build of dies are summarized in Table 5.4.

Another metric useful for the analysis of cavitation is the reproducibility of the cavitation zone length for a given inlet pressure and mass flow. Unfortunately, these measurements are only approximate due to visual observation error, and due to the fact that only a small $\Delta p$ changed the flow from partial cavitation to super cavitation. For a typical run, the repeatability of a zone length at a particular mass flow and inlet pressure was ±30%.

**Table 5.4 Cavitation Repeatability**

| Cascade Geometry | Working Fluid | Cavitating Repeatability Results | |
|---|---|---|---|
| | | Within Die | Die to Die |
| Symmetric cascade A | Water | 10.9% | 11.0% |
| | Ethanol | 8.9% | 9.9% |
| Symmetric Cascade B | Water | 9.2% | 10.4% |
| | Ethanol | 8.4% | 9.8% |

### 5.4.3 CFD VALIDATION

Results from initial CFD models described in Section 5.2.3 were used to develop more accurate grids and modeling inputs[5]. These models were then used to compare with experimental results from the second build of symmetric dies. As in Section 5.3.3, experimental pressure readings were compared to pressures at the same location on the models generated with the same inlet conditions. Table 5.5 summarizes the inlet conditions modeled along with the experimental values for non-cavitating runs. Average error of the pressure tap readings between modeling and experimental data is also stated. Figure 5.24 shows an example of the CFD validation results for each pressure tap location for symmetric cascade A with water. All models for non-cavitating runs match experimental results within the 5% experimental uncertainty of the pressure readings. Validation results for rest of the runs of Table 5.5 are displayed in Appendix A.

**Table 5.5 FLUENT modeling inputs along with corresponding experimental inlet conditions for non-cavitating runs**

| Cascade Geometry | Working Fluid | Inlet pressure (psi) | | Mass Flow (g/s) | | Ave % difference |
|---|---|---|---|---|---|---|
| | | CFD | Experimental | CFD | Experimental | |
| Symmetric A | Water | 108.96 | 116.85 | 2.2 | 2.23 | 2.3 |
| | Ethanol | 110.43 | 107.34 | 2.3 | 2.2 | 4.6 |
| Symmetric B | Water | 98.376 | 93.93 | 6.63 | 6.65 | 2.76 |
| | Ethanol | 90.874 | 87.774 | 5.94 | 5.95 | 4.43 |

[5] These grid geometries and modeling inputs are described further in Appendix A

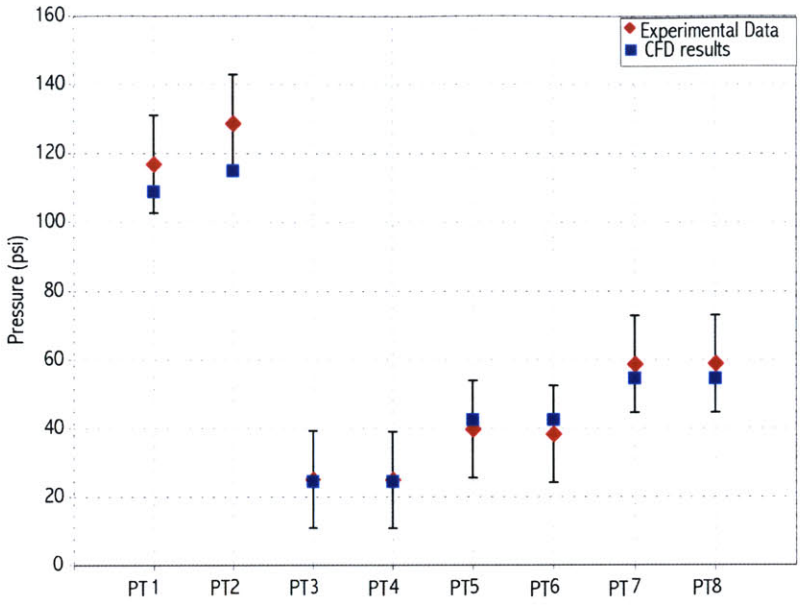


**Figure 5.24 CFD validation example of non-cavitating symmetric cascade A (water)**

Modeling of cavitating conditions produced poor comparisons to data, partly due to difficulty in reproducing cavitating runs. In addition, the numerical modeling scheme did not incorporate a two-phase model, and thus allow negative liquid pressures to exist. Since this model is not physically realistic, a two-phase flow model would be needed to increase accuracy. Average difference from the pressure tap readings between modeling results for cavitating runs were on the order of 25%. Figure 5.25 shows an example of the CFD validation results for each pressure tap location for a cavitating symmetric cascade A with water. From the figure, it is evident that the results exhibit discrepancies at the points of minimum pressure, where the pressure is theoretically negative. Further examples of cavitating CFD results are displayed in Appendix A. However, for practical purposes, modeling micro-scale devices without a two-phase model is sufficient, since design intentions are to avoid cavitation.

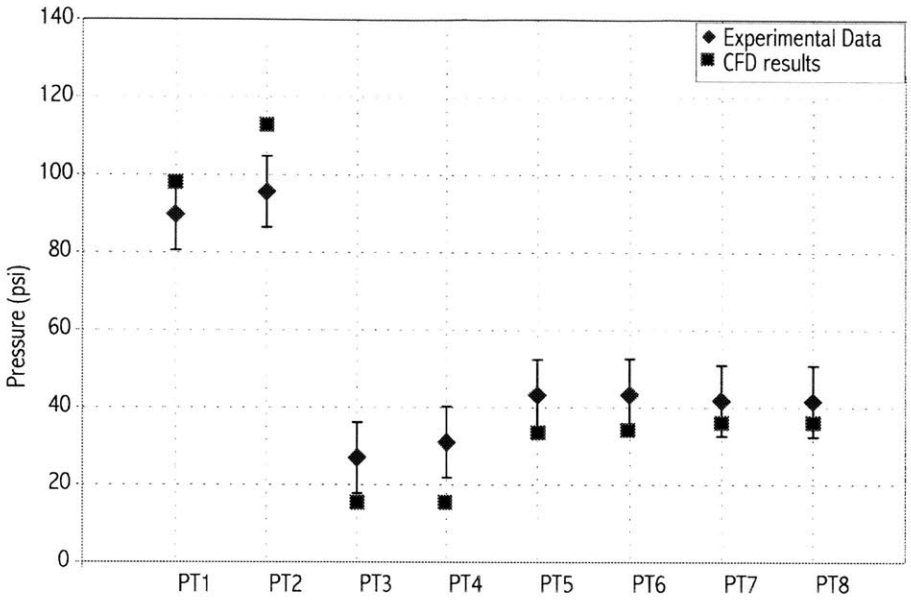


**Figure 5.25 CFD validation of cavitating results**

Another motivation for CFD validation was to examine the 3D flow fields. The final stage of CFD modeling used half of a cascade, and applied a symmetry boundary. This allowed a finer grid with less computation time. The static pressure contours along the blade and cascade for the symmetric B cascade are depicted in Figure 5.26. The figure shows that the point of minimum pressure is along the center of the blade span and along the center of the cascade passageway, depicted at the bottom of the passageway in Figure 5.26. Visual observations of cavitation discussed in Section 5.4.1 validated this observation. Appendix A displays the 3D pressure profiles for other 3D working fluids and geometries, which show the same trends of minimum pressure occurring along the center span of the cascade.

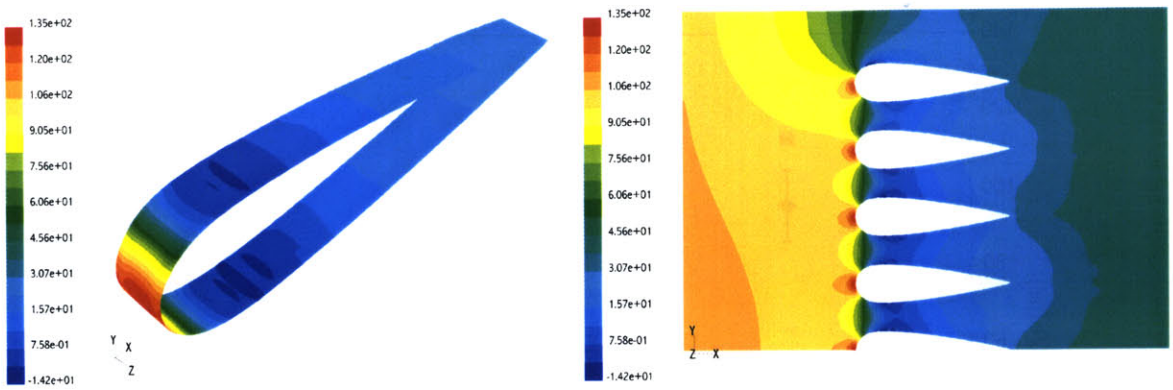


**Figure 5.26 Static pressure contours for Symmetric Cascade B, showing that the point of minimum pressure occurs along the center span of the blade in the center of the passageway**

### 5.4.4 BUILD #2 CONCLUSIONS

The section presented the results from the second build of cascade devices. Theoretical cavitation curves for water and ethanol were presented, showing that the inception point follows macro-scale theory within 10%. Visual observations suggested that cavitation is initiated by disruptions of flow patterns in the cascade, such as pressure taps, contaminants in the flow, and the laminar separation point on the blade. The effects of added blades were examined, concluding that cavitation was most likely to occur in the center of the passageway regardless of the number of blades. Observations also showed the hysteretic and time lag characteristics of cavitation.

Repeatability of the second build of dies was established for non-cavitating runs. Cavitating runs did not exhibit the same repeatability characteristic due to the unsteadiness of pressure readings, hysteresis, and time lag phenomenon. Finally, CFD modeling validated FLUENT as a viable design tool, and the 3D effects of the flow field were determined. The next section discusses cavitation influence on cascade performance by synthesizing data from the symmetric dies.

## 5.5 CAVITATION PERFORMANCE IMPACTS

This section quantifies the performance impact of cavitation on the cascades. The main performance losses associated with cavitation include loss of $\Delta p$ downstream of the blades, blockage, and cavitation erosion. Once the performance effects are determined, results can then be directly applied to the modeling of cavitation in micro-scale turbopumps, discussed in Section 5.6 Section 5.5.1

discusses performance loss in terms of percentage loss of Δp along the passageway. The scheme used in generating a pressure profile along the blade from experimental data is presented. Test results are used to create a model of loss of pressure recovery versus the cavitating zone length observed in a cavitating test. Next, Section 5.5.2 discusses flow blockage due to cavitation, indicating where points of maximum cavitation zone length exist for a given mass flow. Correspondingly, zone length versus inlet pressure can be estimated for a given mass flow. These results are then compared with the bubble growth theory presented in Section 3.5.2. Correlation factors are calculated from empirical data to relate macro-scale bubble growth analysis to a micro-scale, so that the performance loss of a turbopump due to cavitation can be calculated. Finally, Section 5.5.3 presents results from the cavitation erosion tests, examining whether erosion due to cavitation is a significant problem for the microfabricated devices.

### 5.5.1 PRESSURE RECOVERY LOSS

When flow cavitates along a blade passage, the liquid "sees" the shape of the blade plus the vapor bubble pocket around it. Therefore, the flow along the blade is subjected to a different pressure profile than design, and in most cases the pressure recovery ($\Delta p$) downstream of the blade drops. 3D CFD results were used to construct the pressure profile along the passageway from the data points, by interpolating the computational values with experimental data at the same inlet conditions. The data was fitted to polynomial functions using a linear interpolation fitting function. This minimized the mean square error between the data and the model values, and created a polynomial function in a least squares sense. Polynomial coefficients were returned for a structure containing a Cholsky factor of the Vandermonde matrix, degree of freedom, and norm of residuals as fields to obtain error estimates on predictions[30]. The codes detailing this method of data reduction is shown in Appendix H.

Figure 5.27 depicts the pressure profiles along the blade of a die SA29 for a non-cavitating, partially cavitating, and super-cavitating test. In this example, the non-cavitating run reached a $-C_{pmin}$ of about 4.3 and exhibited about 20% pressure recovery. The partially cavitating run did not reach the $-C_{pmin}$ of the non-cavitating run, since the liquid vaporized before this point, and less pressure recovery was recoded at the end of the blade (x/l=1.1) where cavitation pockets were visually observed. However, downstream of the passage (x/l=3.5), where no cavitation was observed, the test exhibited the same non-dimensionalized pressures as the non-cavitating flow. This suggests that partial cavitation has a performance impact only where the cavitating pockets occur. In contrast, super cavitating runs

exhibited less pressure recovery throughout the entire passageway. In some cases, like that of Figure 5.27, even if the observed super-cavitation does not last 3.5 blade lengths, there was still less pressure recovery. This is due to the fact that blockage interfered with pressure recovery. For a super cavitating die, the loss of pressure recovery was on the order of 10%. Performance loss curves were generated only for tests with pressure taps. Curves for different cascade geometries and working fluids are displayed in Appendix G. These display the same trends as that of Figure 5.27.

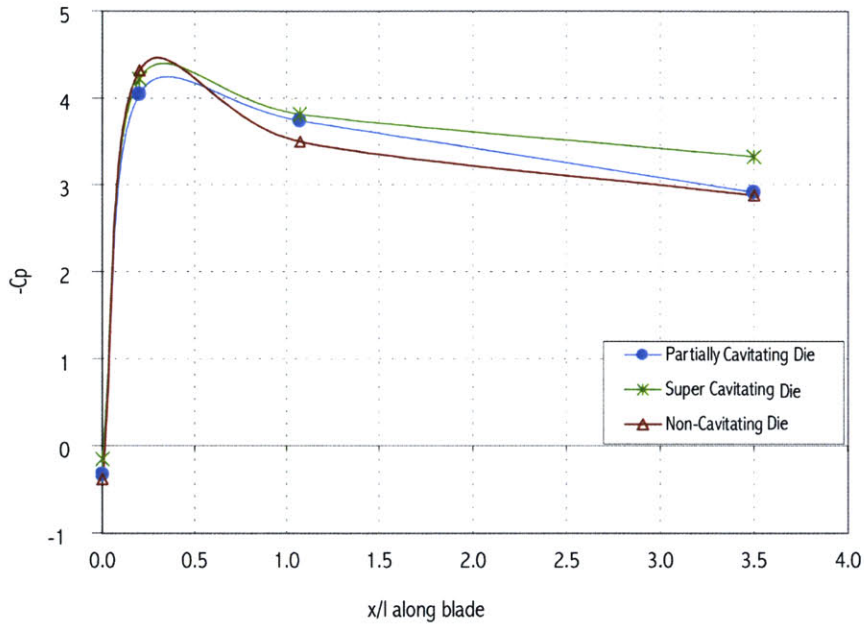


**Figure 5.27 Performance loss effects for partially cavitating, super cavitating and non-cavitating die SA29**

For a turbopump, loss of pressure recovery is transformed directly into performance loss, since performance is related to $\Delta p$ (Section 2.2). Therefore, performance curves such as Figure 5.27 can be used to determine the performance impact of different cavitation extents. For each cavitating test, a cavitation zone length normalized with the blade length was visually observed and recorded. The data was then coupled with performance charts such as Figure 5.27 to determine the loss of $\Delta p$ for a given zone length. These results are plotted in Figure 5.28 for all symmetric cascade geometries. Experimental data was fit with a polynomial function.

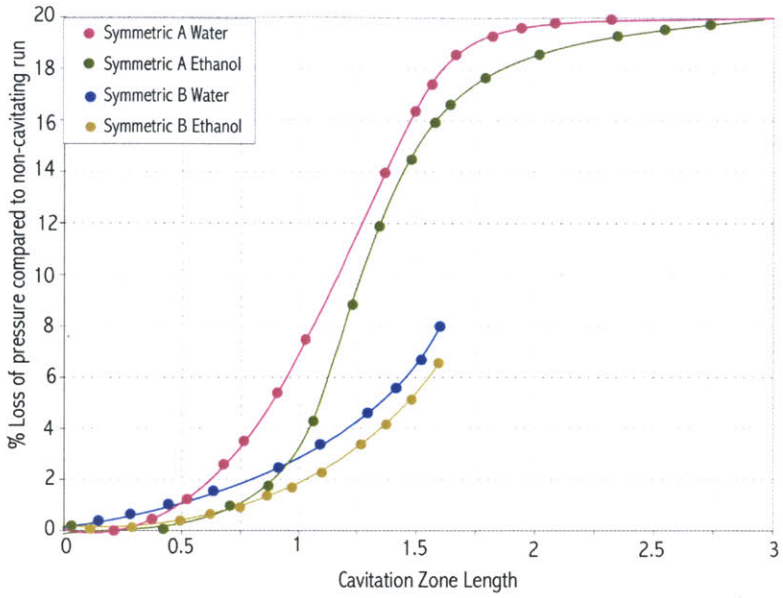


**Figure 5.28 Amount of pressure loss for a given cavitating zone length**

From the figure, it is apparent that normalized zone lengths above 1.6 were not observed in the symmetric B cascades. Also, the symmetric A cascades appear to have a point of inflection around the zone length of x/l =1.5. From visual observations, this appears to be the point where partially cavitating pockets such as those depicted in Figure 5.1 combine to form a super-cavitation pocket like that depicted in Figure 5.2. Once super cavitation is established, the performance loss appears to reach a limiting value of about 20%. As discussed in Section 5.4.2, the reproducibility of cavitating zone lengths for a given inlet pressure and mass flow rate was poor. Combined with the visual observation error, these results carry an uncertainty of ±25%. The uncertainty analysis for this calculation is presented in Appendix F.

### 5.5.2 CAVITATION ZONE LENGTH ANALYSIS

The pressure drop from the supply tank to the dump tank controls the mass flow through the device. However, when the extent of cavitation becomes large enough, the mass flow does not change if the pressure drop increases for a given inlet pressure. Instead, the extent of cavitation increases. The cavitation zone length does reach a limiting value, however, since the pressure drop through the rig cannot be greater than the inlet pressure. Figure 5.29 shows a schematic of the limiting value of mass flow for a given inlet pressure and pressure drop for the symmetric cascade A with water. As shown,

the cavitation inception point does not reduce the mass flow, but soon thereafter the cavitation becomes severe enough to immediately block the passage. The results from this figure show that the inlet pressure drop from cavitation inception to the maximum possible cavitation zone length is extremely small, which is what has been observed experimentally. This may be due to hysteresis, since once super cavitation begins; it is difficult to supress cavitation.

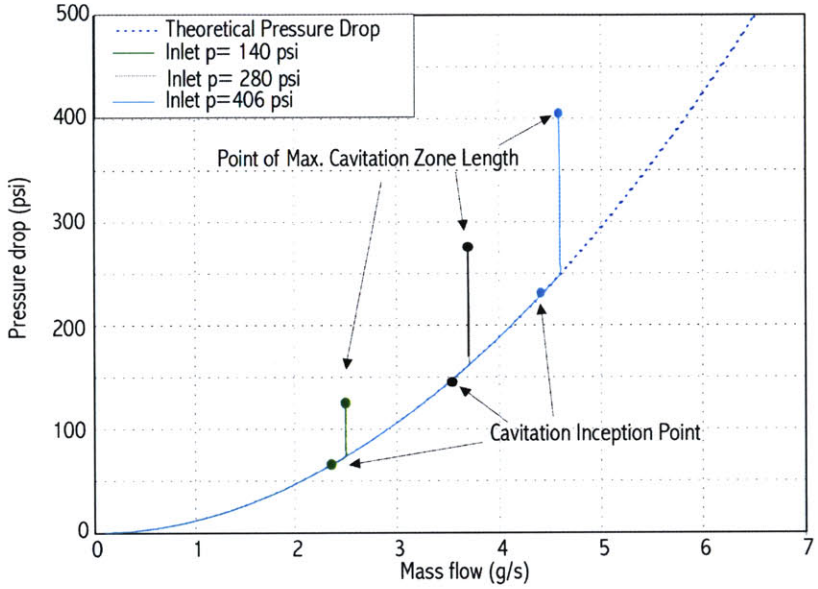


**Figure 5.29 Mass Flow limits for a given inlet pressure due to pressure drop through device**

This limiting value of mass flow and maximum cavitation zone length were experimentally recorded and compared to the zone length theory presented in Section 2.4.8. Figure 5.30 plots maximum cavitation zone length results from all symmetric A cascade testing using water along with the theoretical curve formulated in Section 2.4.8. A data curve fit was applied to the experimental data using a function that produced error bounds which contain at least 50% of the data[30]. This established correlation factors between the experimental results and the macro-scale theory. Figure 5.31 shows the same results for a symmetric B cascade with water. Results show that macro-scale theory predicts a greater cavitation extent than observed experimentally. Since the data is only accurate to ±25%, however, macro-scale theory may still hold true. Tests with ethanol produced similar results, and are plotted in Appendix G. The empirical correlation between the macro-scale was obtained by calculating the mean square error between the two values. The reduction codes for the above calculations are shown in Appendix H.

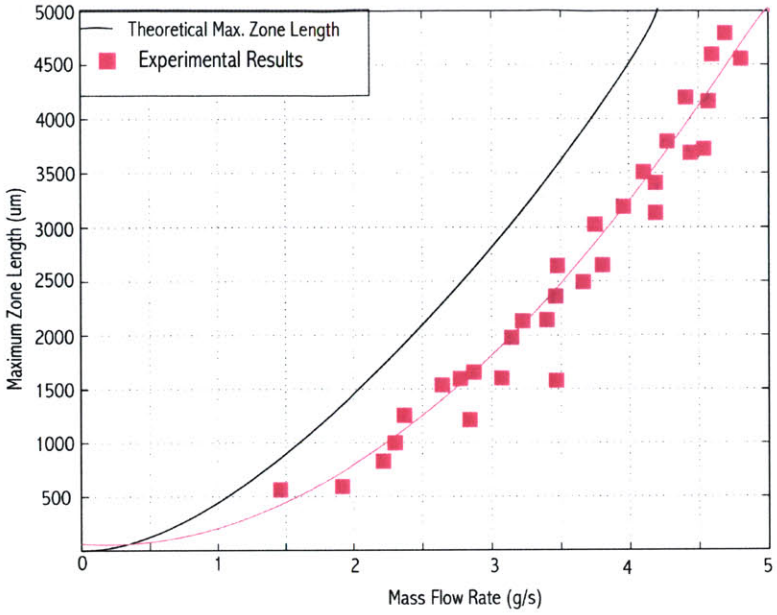


**Figure 5.30 Experimental theoretical zone lengths for Symmetric cascade A (water)**

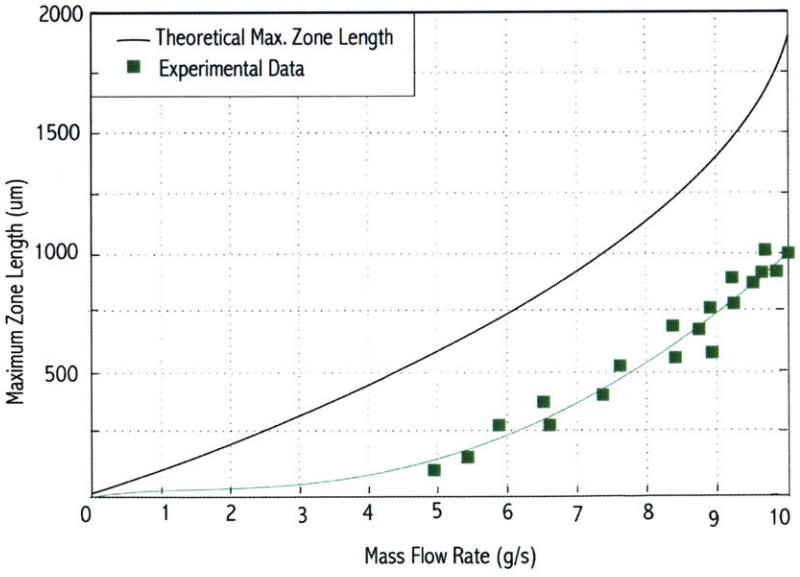


**Figure 5.31 Experimental theoretical zone lengthsfor Symmetric cascade B (water)**

### 5.5.3 CAVITATION EROSION

As mentioned in Section 2.2.2, cavitation erosion damage affects the performance of macro-scale pumps, altering the flow geometry and even inducing mechanical failure. Therefore, cavitation erosion on a micro-scale was examined. In order to simulate micro-turbopump conditions, one symmetric A cascade from the second build was run with water at the turbopump design mass flow of 2.5 g/s at supercavitating conditions (nondimensionalized zone length of 1) for 20min. The blades were then examined under a scanning electron microscope (SEM) with a along with two other devices, one cascade which experienced the most cavitating runs and another device which was not run at all. No signs of erosion were detected on any of the dies, as depicted in Figure 5.32. This suggests that for the purposes of micro-devices operating for less than 20min, cavitation erosion will not be an issue.

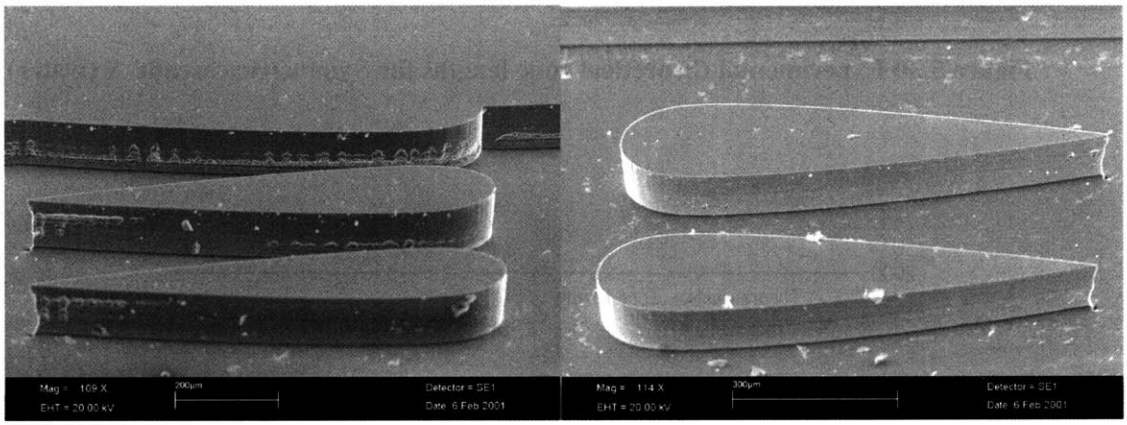


**Figure 5.32 NoCavitation is evident for blades experiencing heavily cavitating conditions**

### 5.5.4 SUMMARY

The impact of cavitation on the performance of micro-fabricated cascades was discussed. Curves were presented which quantified the pressure recovery loss versus cavitating zone length. Experimental values of maximum cavitation zone length versus mass flow was presented and validated against theoretical models. A correlation between inlet pressure and performance loss was defined, to use in modeling microturbopump cavitation. Finally, cavitation erosion was examined, showing that damage caused by erosion will not be a problem for practical applications of these silicon microfabricated devices.

## 5.6 DISCUSSION OF RESULTS

This section synthesizes the experimental results described in the previous section to present overall implications for the design of a turbopump. Performance loss of microturbopumps operating under cavitating conditions is predicted. Then, a summary is presented of the conclusions, and their implications. Finally, design criteria for the microturbopumps are established.

### 5.6.1 CAVITATION PERFORMANCE IMPACTS ON MICROTURBOPUMPS

A design methodology to predict performance impact due to cavitation in turbopumps is presented in this section. From micro-scale cascade results, empirical relations have been found to extend macro-scale bubble growth analysis to the micro-scale. These correlations can then be applied to the bubble growth model for a microturbopump, to determine the maximum zone length for a given mass flow. Using residence time theory, the above relation can be calculated as a function of inlet pressure for a given mass flow. Experimental observations relating zone length to performance loss can then be used to estimate the performance loss for the microturbopumps. Finally, by combining the above two relations, performance loss versus inlet pressure can be plotted for a given inlet pressure, which defines the cavitating operating space for the microturbopumps.

First, an empirical relation was found correlating the zone length theory described in Section 3.5.2 to the experimental data presented in Section 5.5.2. The maximum cavitation zone length for a particular mass flow was then computed by finding the residence time for a particular mass flow from equation (2.22), and equating that to the maximum possible bubble size that can grow during that time period, using the procedure detailed in Section 2.4 and the empirical correction factor determined in Section 5.5.2. However, for a given residence time, there is also an inlet pressure associated with a set mass flow, since the amount of time that the blade will be experiencing cavitating conditions depends on inlet pressure. As the inlet pressure gets closer to the inception point, less of the blade will be subject to negative pressures. The cavitation residence time for a particular inlet pressure can be calculated by the $C_p$ distribution along the blade for a given mass flow. A schematic of this computation is depicted in Figure 5.33 for the demonstration boost turbopump. For a given mass flow, the point where the blade will first be subjected to cavitation can be determined using equations (2.3), (2.5) and (2.6). The fraction of the blade experiencing negative pressures is then calculated, and multiplied with the total residence time of the microturbopump (as calculated in Figure 2.11). Figure 5.33 and Figure 5.34

show the results of these calculations for a mass flow rate of 2.5 g/s for the demonstration boost pump and main microturbopump, respectively.

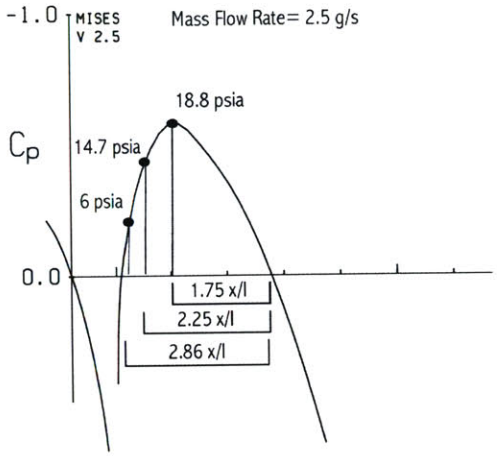


**Figure 5.33 Schematic of the relation between residence time and inlet pressure.**

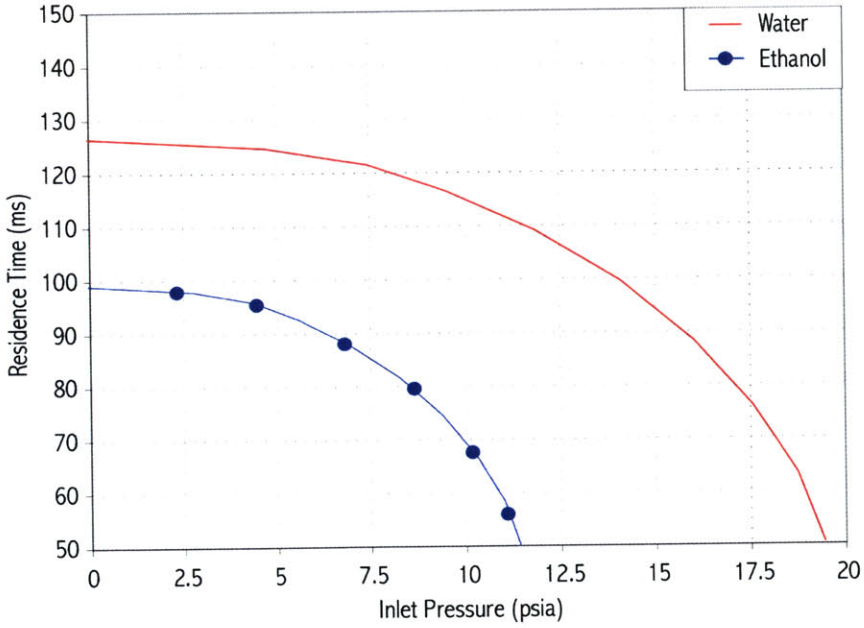


**Figure 5.34 Residence time vs. inlet pressure for demonstration boost pump, at a mass flow rate of 2.5 g/s**

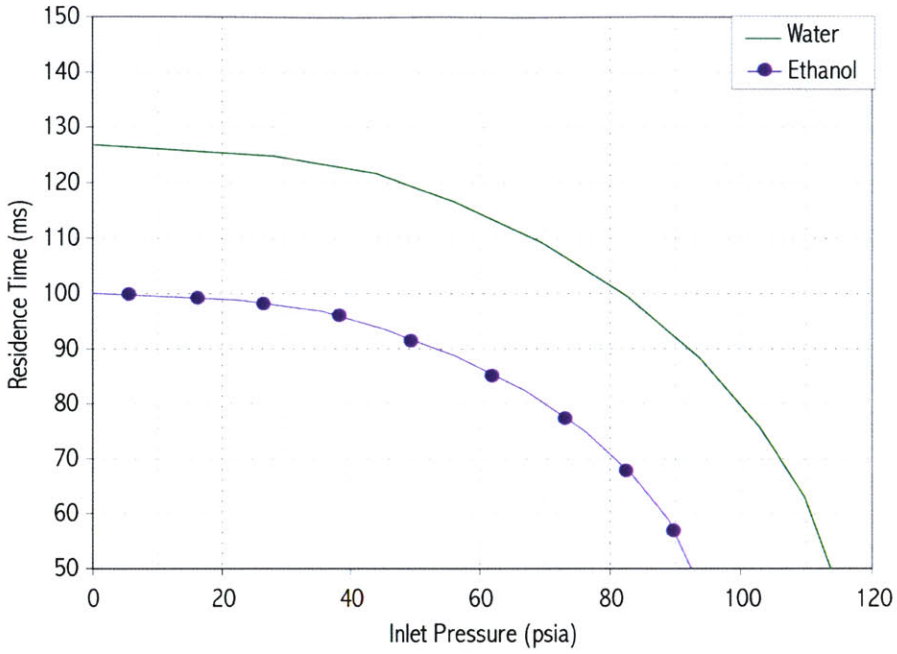


**Figure 5.35 Residence time vs. inlet pressure for main pump, at a mass flow rate of 2.5 g/s**

With the above relations, the maximum zone length can be plotted for a given inlet pressure. The results of this analysis are displayed for both the main turbopump and the boost demonstration pump in Figure 5.36 and Figure 5.37. A code describing the empirical relations used to determine zone length is presented in Appendix H.

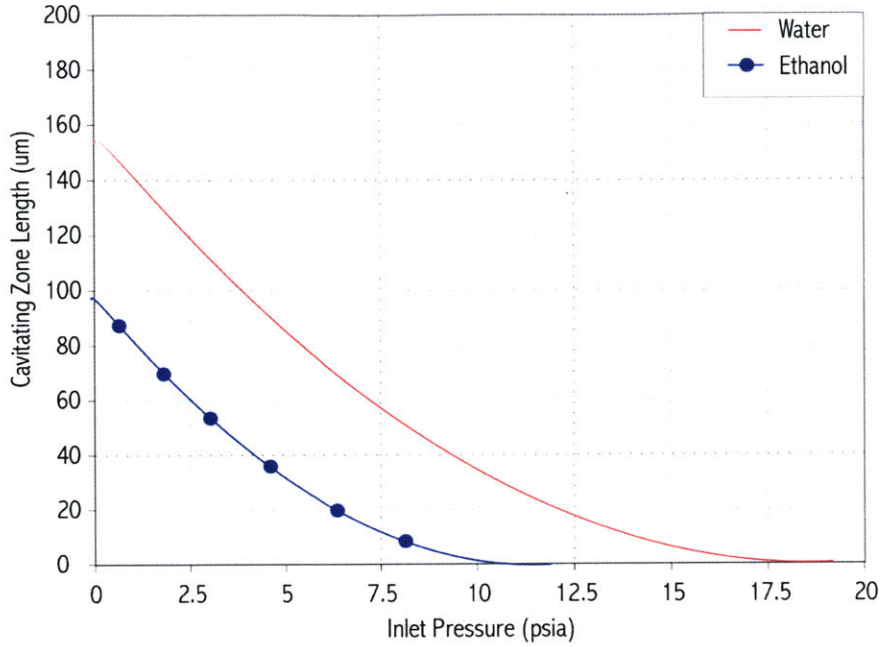


**Figure 5.36 Cavitating zone length vs. inlet pressure for boost pump at a mass flow of 2.5 g/s**

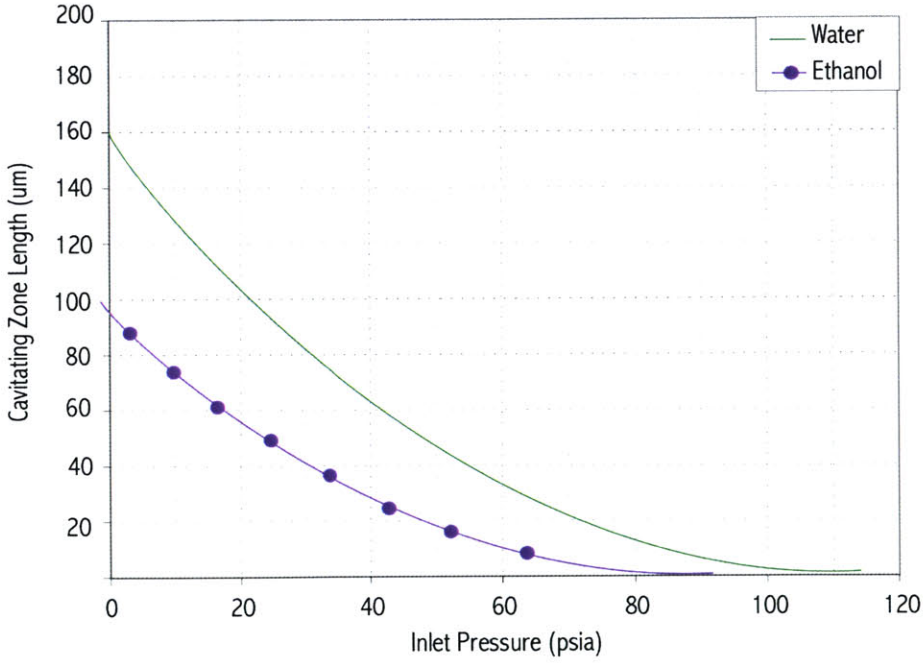


**Figure 5.37 Cavitating zone length vs. inlet pressure for main pump at a mass flow of 2.5 g/s**

As depicted in the figures, the cavitating zone never becomes greater than the blade length due to the high pressure recovery in the pump. Therefore, it appears that the microturbopump will be subjected only to partial cavitation pockets, and never experience super-cavitation.

Finally, the above relations can be correlated with the visual observations noted in Figure 5.28 to plot the performance loss that would occur for operating at a given inlet pressure. The results of Figure 5.28 for all cascade geometries between the zone lengths of x/l=0 and x/l=1 were averaged and applied to the microturbopump modeling. However, for the microturbopump, the pressure profile during the first 0.2 blade lengths along the blade is vital to achieving the $\Delta p$ required [30]. 2D simulations of the demonstration boost turbopump with a different effective blade shape were performed using MISES and determined that the pressure loss was a factor of 4 higher than that predicted by the stationary cascade. This factor was applied to the performance loss estimate, and results for the demonstration boost pump and main turbopump are displayed in Figure 5.38 and Figure 5.39. The detailed reduction scheme for this calculation is shown in Appendix H. Uncertainty analysis of the calculation was performed and determined to be ±34%.

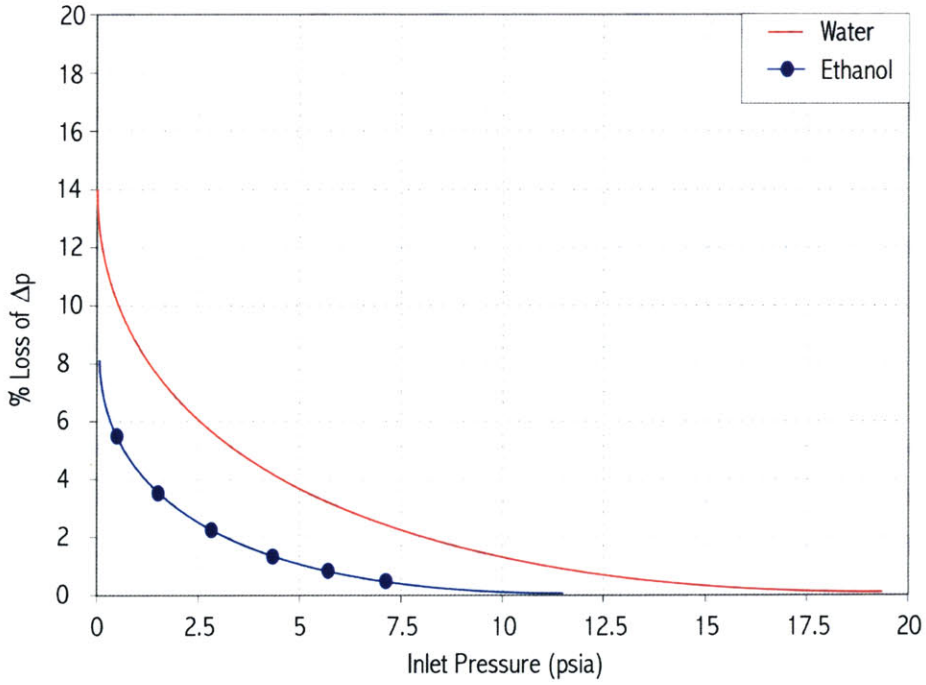


**Figure 5.38 Performance loss vs. inlet pressure for a boost turbopump at a mass flow of 2.5 g/s**

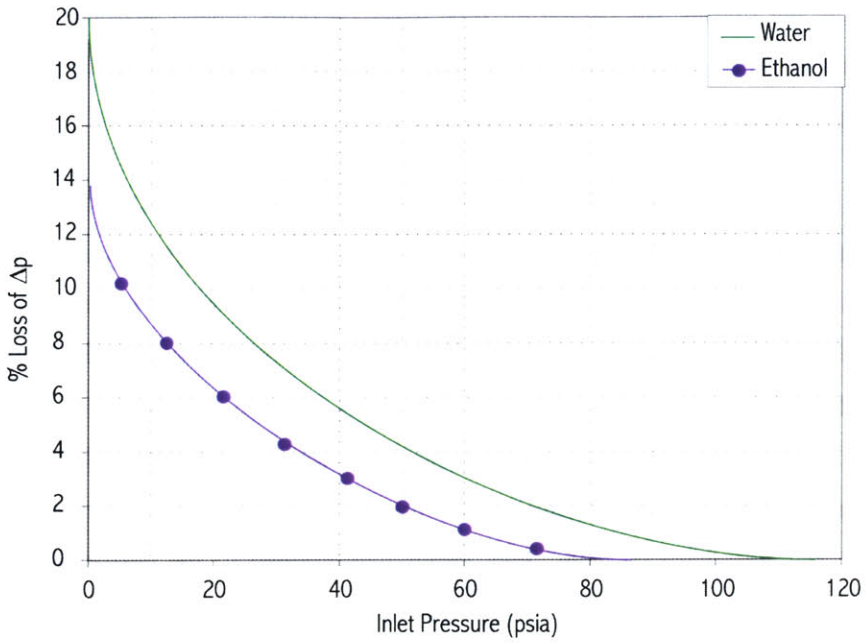


**Figure 5.39 Performance loss vs. inlet pressure for the main turbopump at a mass flow of 2.5 g/s**

### 5.6.2 MICRO-SCALE TURBOPUMP BLADE CAVITATION CONCLUSIONS

This section summarizes the conclusions about micro-scale turbopump blade cavitation from the results presented in this chapter.

Micro-scale cavitation has been showed to exist, and therefore is a potential technical issue for the micro-turbopump. Inception curves follow that of macro-scale theory within experimental error, although the inception point occurs consistently at a lower inlet pressure than macro-scale theory predicts. Perturbations in the flow field, such as pressure taps, the laminar separation point of the blade, and contaminants of the flow are potential contributors to the initiation of cavitation on the blades. Macro-scale cavitation phenomenon such as hysteresis and time lag also occur on the micro-scale and should accounted for in design. The methods established to detect cavitation include visual observations and acoustical measurements.

The performance loss associated with micro-scale cavitation is less severe than that observed in macro-scale applications. A first-order methodology to predict the performance loss has been formulated from micro-scale experimental data and theoretical modeling. The predictions suggest that the maximum loss of $\Delta p$ associated with cavitation is 14% for the boost demonstration pump and

20% for the main microturbopump. The turbopump may operate at cavitating conditions for the duration of design life with no corresponding erosion damage.

3D numerical models are viable tools for the design of cavitation-free devices. These models have been proven to accurately predict the pressure profiles along micro-scale turbopump blades. Validation efforts have also illustrated the 3D pressure contours along micro-scale devices, providing valuable information about sidewall and endwall effects at a micro-scale.

### 5.6.3 CAVITATION DESIGN CRITERIA FOR A MICROTURBOPUMP

The conclusions stated in the previous section provide a preliminary basis for the establishment of cavitation design criteria. The following guidelines have been formulated to optimize the performance of a microturbopump:

1. To ensure a cavitation-free microturbopump, the inlet pressure must be above that determined by 3D numerical models.

2. Elimination of perturbations in the flow field may prevent cavitation from initiating.

3. To detect cavitation, both visual and acoustic methods should be used.

4. Once cavitation has occurred, the inlet pressure must be raised higher than that which initiated the cavitation to free the pump of cavitating effects, the amount depending on the extent of cavitation.

5. The turbopump should be designed to a $\Delta p$ 20% higher than required for sufficient operation, to ensure that the pump will still deliver the $\Delta p$ required for successful operation of the micro-rocket engine during the most extreme cavitating conditions.

## 5.7 CHAPTER SUMMARY

This chapter has presented the results of the tests run on micro-scale cascades. These tests were conducted using both ethanol and water. Cavitation was observed to start at the same location as predicted by macro-scale theory. The characteristics of cavitation hysteresis and time lag were discussed. Repeatability of the tests was established. Results were shown that established 3D

numerical modeling as a viable design tool. An analysis of the performance impact of cavitation on a micro-scale was conducted, concluding that micro-scale effects are not as severe as those found on the macro-scale. Experimental results were combined with theoretical modeling to establish implications of cavitation on micro-scale turbopump blades. Finally, cavitation design criteria for micro-turbopumps were defined.

# 6 CONCLUSIONS AND RECOMMENDATIONS

This chapter will present a summary of the research conducted for this thesis, describe the specific contributions of this research, and make recommendations for future work in this area.

## 6.1 SUMMARY

The subject of a silicon micro-fabricated turbopump for the use in a micro-fabricated bipropellant liquid rocket engine has been introduced. Cavitation has been identified as a major technical issue in the demonstration of a micro-turbopump.

The cavitation phenomenon has been investigated on a micro-scale, specifically in relation to the microturbopump designs. Cavitation inception and bubble growth were theoretically analyzed, and potential deviations from macro-scale theory were discussed. The analysis suggests that residence time, surface roughness, surface tension, and passage area constraints are significant factors in the determination of cavitation inception and growth. However, no micro-scale data was available to verify these findings.

A non-rotating microfabricated cascade was designed, fabricated, and tested to quantify the behavior of cavitation bubbles at micro-scale. Three cascades were designed with two different blade geometries (using 2D and 3D numerical codes) to simulate flow and blading properties of the turbopump. The devices consisted of two wafers of silicon with Pyrex on top to allow visual observations. Pressure taps were placed around the blade to measure the performance loss due to cavitation.

An experimental rig was constructed, and 18 dies were tested from two builds. Visual observations confirmed the existence of micro-scale cavitation, and showed the phenomenon of hysteresis and time lag. Test results showed that cavitation inception followed macro-scale theory. Test repeatability was established. 3D numerical modeling results were shown to match the data. Performance impacts of

cavitation on micro-scale devices were discussed, presenting correlations. Micro-scale cavitation appears to cause less damage than micro-scale cavitation.

The analysis of micro-scale cavitation led to design criteria for micro-scale turbopumps. Micro-scale experimental results combined with macro-scale theory determined performance impacts for cavitating micro-turbopumps. It was shown that for a micro-turbopump operating at the most severe cavitating conditions, the performance loss is not greater than 20%.

## 6.2 OVERVIEW OF CONTRIBUTIONS

The contributions of this work may be summarized as follows:

1. The theoretical modeling of micro-scale cavitation, including theoretical cavitation inception curves and bubble growth analysis

2. The design, fabrication, packaging, and testing of a micro-scale cascade constructed from silicon to examine the effects of micro-scale cavitation

3. The experimental demonstration and analysis of cavitation on micro-scale cascades

4. Validation of FLUENT as a viable 3D numerical tool to for micro-cascades

5. Development of cavitation design criteria for a microturbopump incorporating the performance loss associated with a cavitating pump

## 6.3 RECOMMENDATIONS FOR FUTURE WORK

The recommendations for future work in this area are as follows;

Using current cavitation cascade designs:

1. Examining cavitation characteristics of a potential fuel or oxidizer to be used in the micro-turbopump would not only allow for a more comprehensive analysis of cavitation on a micro-scale, but also be a more applicable exercise in determining design criteria for the microturbopump.

2. Since the microturbopump may be operating at very high temperatures due to the high coolant temperatures emerging from the recirculation jacket around the thrust chamber, cavitation experiments should be run at correspondingly higher temperatures. This would increase the vapor point of the liquid, making the pump more susceptible to cavitation. The potential consequences of cavitation at a high temperature should be researched.

3. The phenomenon of hysteresis and time lag should be more closely examined, since hysteresis makes cavitation difficult to overcome once it has started. However, the time lag phenomenon allows for no loss of performance associated with the beginning of the run, which may have many benefits to the microturbopump with a design life of about 20 minutes.

4. Documentation and analysis of the noise produced by partially cavitating and super cavitating runs should be acquired and analyzed, in order to determine the frequencies at which bubbles collapse for a given kind of cavitation. This will help determine what kind of cavitation is occurring during full-scale operation of a liquid bi-propellant rocket engine, where the turbopumps are hidden from sight.

5. The experimental rig to date has been run with contaminants up to 5um, which may be creating worse cavitating conditions than would be created with less contaminants. Running a clean cascade device though a fully purged rig to ensure less contamination may result in a lower theoretical cavitation curve.

Other devices:

1. Another cascade device should be fabricated which has the close to the same pressure profile as the symmetric devices, but a laminar separation point which occurs downstream of the blade, after sufficient pressure recovery. Running this device would determine the role of the laminar separation as a cavitation initiator.

2. A more effective asymmetric cascade should be designed and fabricated, in order to see the effect of bubble collapse on the flow. In many cases, bubble collapse is more damaging to macro-scale pumps than inception.

3. The implications and design criteria developed for the microturbopump must be validated with experimental results. A demonstration boost pump and main turbopump must be fabricated and tested to determine the viability of the design methodology presented in this thesis.

# APPENDIX A

# CFD MODEL VALIDATION EFFORTS

## A.1 INTRODUCTION

The Appendix describes the numerical models used when designing the cascade experiment, and details relevant results in the three stages of FLUENT modeling.

## A.2 MODEL DESCRIPTIONS

### A.1.2 MISES

MISES is a quasi 3-D design and analysis code for turbomachinery cascades. It uses the integral momentum boundary layer theory and projects the 3-D equations on an axisymmetric streamsurface of varying radius and thickness to solve the steady two-dimensional Euler equations. The equations are discretized on a streamline grid and used to represent the inviscid flow field. The viscous effects on the cascade surface and in the wake are modeled by a two-equation integral boundary layer formulation coupled to the inviscid flow field by the displacement thickness concept. Closure of the boundary layer equations is achieved through relations for the skin friction, dissipation, and energy thickness. The fully-coupled system of non-linear equations is solved simultaneously by a global Newton-Raphson method. Further details of the code are given in [24] and [25].

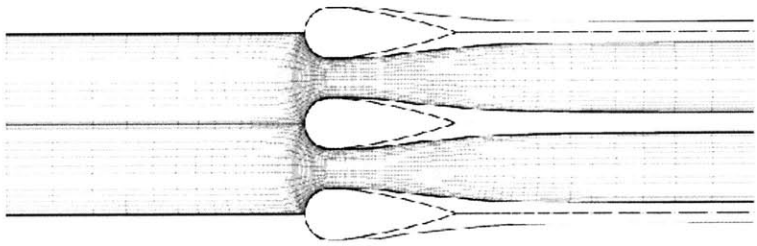

**Figure A.1 Typical Grid for a MISES solution, showing no resolution of the boundary layer**

### A.1.3 FLUENT

Fluent is a general purpose computational fluid dynamics code developed by Fluent Inc. that predicts fluid flow, heat transfer, mass transfer, chemical reactions, and other related phenomena. The software solves for the complete Navier-Stokes Equations, the continuity equation, the energy equation, and a turbulence model. In addition, the stress tensor, the equation of state, and a constitutive relation are solved to comprehensively describe the flow. The flow solver solves a representation of each of the equations for each cell in the computation domain of the problem many times over. The basis of the turbulence models come partly from experimental work, and addresess various types of flow via such characteristics as the amount of separation, recirculation, and convection due to heat sources. The modeling capabilities of the Fluent package include flows in 2D or 3D geometries using structures or unstructured grids, incompressible or compressible flow, laminar, turbulent, steady state or unsteady analysis, and convective heat transfer.

### A.1.4 Comparison of Models

MISES is essentially a 2D compressible code that does not solve for endwall effects, since it uses the integral momentum boundary layer approach, as depicted in Figure A.1. To solve for incompressibility, a very low mach number was used in the design efforts. However, MISES can predict transition on the blade, and models laminar separation with a corresponding turbulent reattachment of the flow over the blade. The laminar formulation uses an $e^9$ and bypass transition models, and the turbulent formulation includes a shear stress lag equation to model upstream history effects of non-equilibrium boundary layers. Fluent, alternatively, can predict 3D endwall effects, incorporate a full incompressible flow solution, and resolve a boundary layer. However, in order to run a FLUENT calculation, the flow field must be specified as either fully laminar or fully turbulent. Transition along the blade cannot be predicted using this flow solver. Table A.1 shows a comparison of the flow solvers of MISES and FLUENT.

**Table A.1 Comparison of MISES and Fluent CFD solvers**

| | MISES | FLUENT |
|---|---|---|
| Dimensions | 2D | 2D & 3D |
| Solver | Integral momentum boundary layer approach | Solves full Navier-Stokes Equations |
| Boundary Layer Resolution | Does not resolve boundary layer | Resolves boundary layer |
| Transition Modeling | Models transition | Does not model transition, can only run full laminar or full turbulent models |
| Compressibility | Compressible code | Incompressible code |
| Geometry | Can only model cascade of 3 blades, cannot model end wall effects | Can model full device flow path |

The main bottleneck between validation of FLUENT against MISES is FLUENT's inability to predict transition. A fully laminar solution nor a fully turbulent solution will not be accurate in comparing the flow solutions with MISES. Therefore, 100% agreement cannot theoretically be achieved without appropriate correction factors.

## A.2 PRESENTATION OF MODELING EFFORTS

The FLUENT modeling efforts were divided into 3 stages of CFD runs. The first stage of runs attempts to validate 2D FLUENT code with MISES. Therefore, all runs were performed in two dimensions using one cascade geometry and a working fluid of water for simplicity. These runs also allowed for proper validation of a 2D FLUENT grid geometry using boundary layers along the blades. The second stage of modeling consisted of generating a 3D model of the flow and comparing it to 2D results at the same inlet conditions, to show the effects of a 3D flow field on the cascade passageways. This stage used one cascade geometry, depicted in Figure A.2, and water. The outcome of this stage resulted in a 3D grid geometry and run conditions that were in close agreement with initial experimental data. The experience acquired in grid generation, boundary conditions, and solvers, could then be used in stage 3 of modeling, which consists of extending the runs to account for different cascade geometries and a working fluid of ethanol. This final stage of runs would eventually be used as validation against a full set of experimental results. The following sections will describe the stage and briefly presents results and conclusions from the most significant CFD runs.

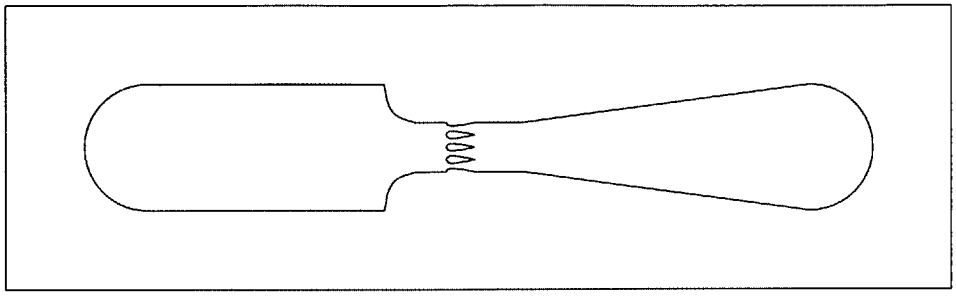

**Figure A.2 Cascade Geometry used for Stage 1 and Stage 2 of FLUENT CFD runs**

## A.3 STAGE 1: 2D FLUENT RUNS

The first stage of the CFD modeling efforts created a viable 2D grid and compared the results with MISES. The entire cascade was modeled in FLUENT, as opposed to the 3 blades in a free cascade that are modeled in MISES. Since transition could not be modeled using FLUENT, both laminar and turbulent modeling runs were preformed, and the results presented. The results of this modeling suggests that 2D laminar solutions are inaccurate downstream of the blade, since recirculation eddies form after the laminar separation point. The turbulent k-e model matches the MISES predicted $C_p$ distribution the best, although differing significantly from the profile during the laminar region.

### A.3.1 MODELING SCENARIOS

Each run in this stage used roughly the same inlet boundary conditions and a working fluid of water. The first run performed was a laminar 2D run using a rough grid with no boundary layer resolution. Finer grids were then generated until the solution showed no dependence on grid resolution. Comparisons of the two girds are shown in Figure A.3. With the finer grid, one laminar run and 3 turbulent runs using different turbulent models and specifications will be presented. A summary of the stage 1 models presented is shown in TableA..

**TableA.2 Summary of Stage 1 FLUENT runs (all runs with mass flow = 1 g/s)**

| Run name | # of cells | 2D/3D | Model | Turb. Specs. | inlet p (psi) | inlet v (m/s) |
|---|---|---|---|---|---|---|
| 2d_noBL | 58388 | 2D | Laminar- no BL | -- | 18.41 | 6.47 |
| finer_lam | 144890 | 2D | Laminar | -- | 18.07 | 6.37 |
| finer2vr | 144890 | 2D | Turbulent S-A | TVR = 4 | 19.96 | 6.55 |
| finer2vr7 | 144890 | 2D | Turbulent S-A | TVR = 7 | 19.86 | 6.56 |
| finer2_ke | 144890 | 2D | Turbulent k-e | 2 Zonal Wall | 16.41 | 6.47 |

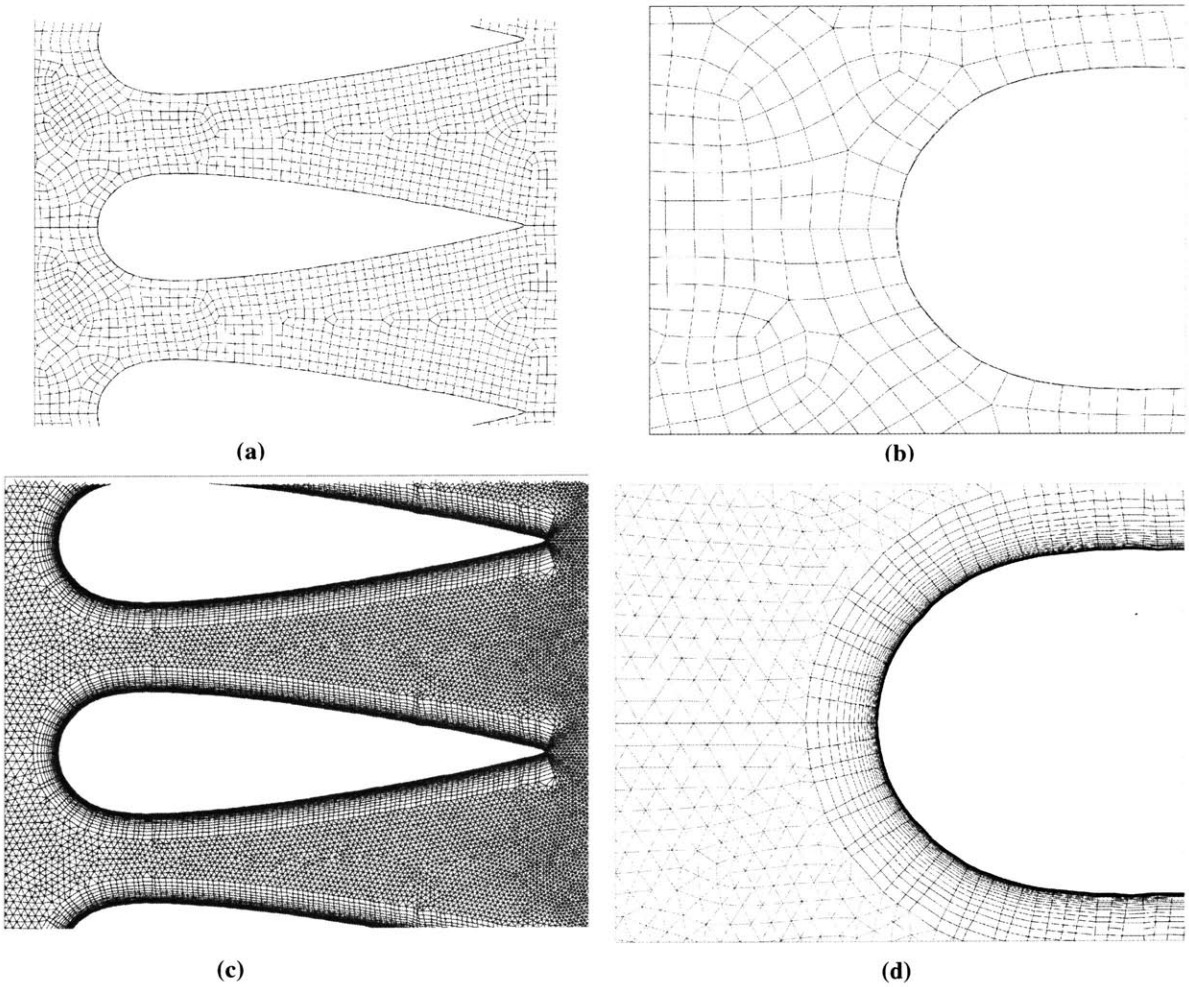


**Figure A.3 (a) & (b) First 2D structured grid with no boundary layer resolution. Compare with refined unstructured grid (c) & (d) where the boundary layers are well defined**

The turbulence models used for modeling included the Spalart-Allmaras model and the standard k-e model. The Spalart-Allmaras model solves one transport equation for a quantity that is a modified

form of the turbulent kinematic viscosity. The standard k-e model solves for two transport equations, and is semi-empirical. The turbulent kinetic energy term (k) is derived from an exact equation, where its dissipation rate (e) is based on physical reasoning and bears little resemblance to its mathematically exact counterpart. For more information on the exact transport equations used in turbulent modeling, refer to [26].

### A.3.2 RESULTS

Using a refined grid, four 2D runs are presented to validate FLUENT against MISES. As mentioned previously, FLUENT does not have the capability to model transition, so runs were specified as fully laminar or fully turbulent. All runs used the same boundary conditions: a mass flow rate of 1 g/s specified at the inlet and outlet pressure of 14.7psi. The first case of a fully laminar run produced unsteady eddies off the trailing edge, and therefore would not converge, as depicted in both the residuals of Figure A.4, and the velocity vectors of Figure A.5. The $C_p$ profile for the laminar run differed from MISES significantly, and since it did not converge, it produced an unsteady pressure profile along the blade (Figure A.8).

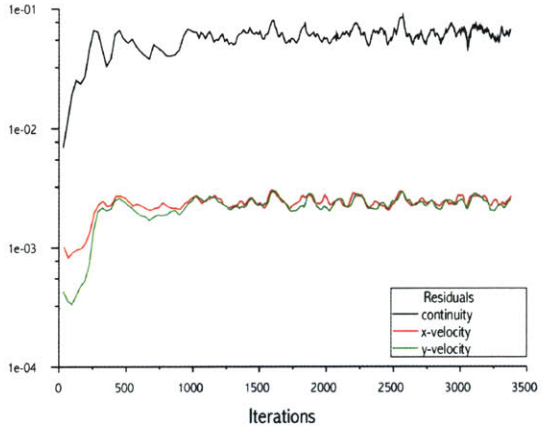


**Figure A.4 Residuals of fully laminar flow, showing poor convergence**

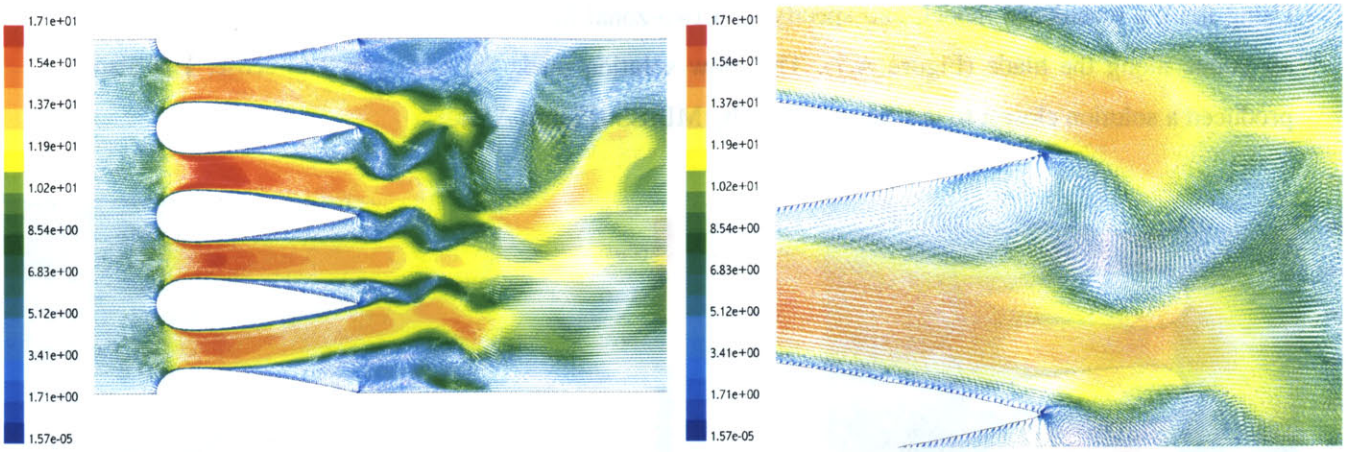


**Figure A.5 Velocity Vectors colored by velocity magnitude (m/s) for the case of a laminar flow solution. Note recirculation eddies at trailing edge**

The Spalart-Allmaras turbulence model decreased the downstream unsteadiness, and the solution seemed to converge. However, as seen in Figure A.6, there were still recirculation zones at the trailing edge of the blade, and the flow was not fully symmetric as shown in MISES. The $C_p$ profiles for the turbulent S-A model were a little closer to that predicted by MISES, although still exhibited a much higher minimum $C_p$ than predicted by both MISES and initial experiments, and the profile showed signs of unsteady behavior (Figure A.8). Changing the turbulence viscosity ratio from 4 to 7 did little to the flow properties, and the pressure profile remained within 1% of the initial values.

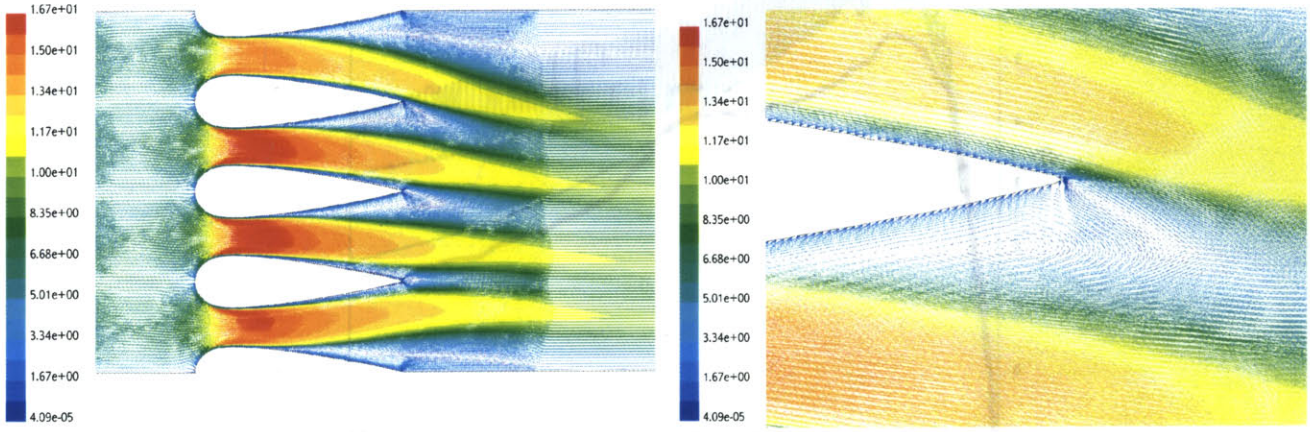


**Figure A.6 Velocity vectors colored by velocity magnitude (m/s) for the case of a turbulent Sparat-Allmaras model. Note the asymmetry of the vectors and the recirculation zone of the trailing edge of the blade**

Using the k-e turbulence model, and specifying a two-zonal layer wall, the flow remained attached at all points along the blade (Figure A.7). This flow solution made the most physical sense, and also produced a solution closest to the one predicted by MISES (Figure A.8).

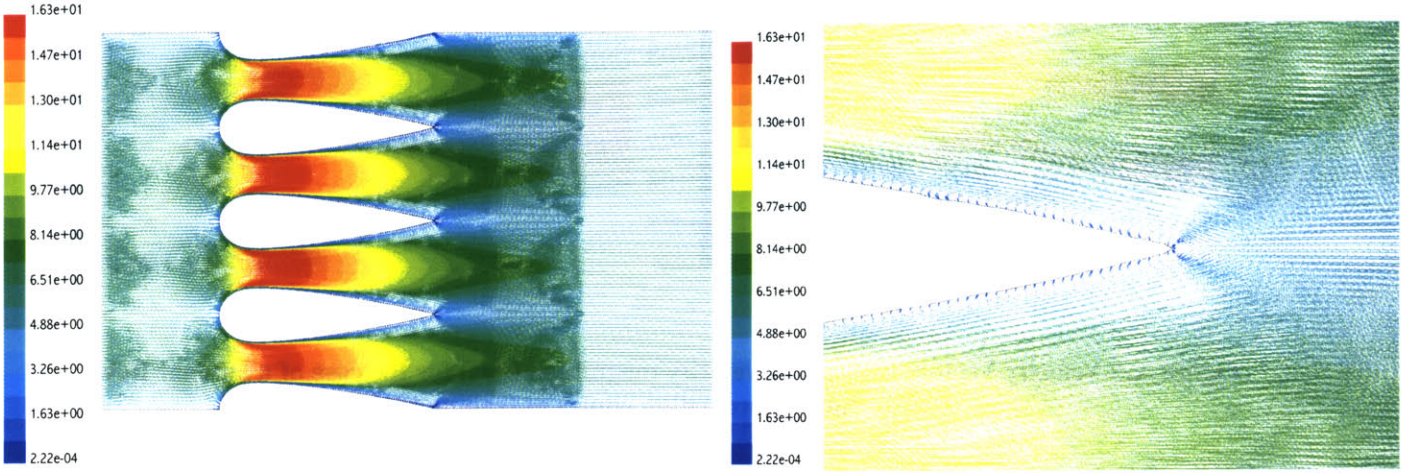


**Figure A.7 Velocity vectors colored by velocity magnitude (m/s) for the case of fully developed turbulent flow using the k-e model. Flow is attached everywhere.**

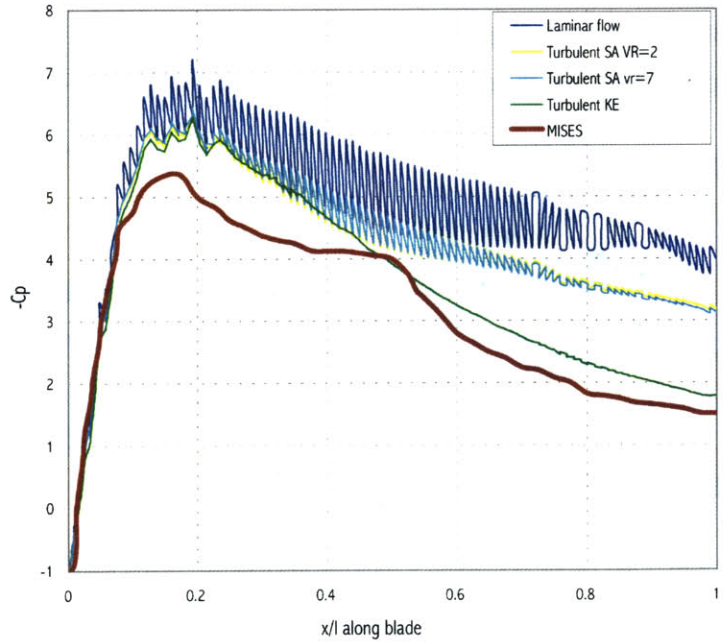


**Figure A.8 $C_p$ profiles of stage 1 CFD runs, showing laminar and turbulent runs compared with MISES.**

### A.3.3 2D Model Conclusions

As shown in Figure A.8, none of the FLUENT 2D models match the pressure profile predicted by MISES. The figure also shows that both the laminar run and the turbulent S-A runs are unsteady. Therefore, it is apparent from both Figure A.8, and the velocity vectors shown previously that the k-e turbulent model matches the MISES prediction the closest, especially in the turbulent region after x/l=0.5. In the laminar region, the model can be up to 15% different which must be taken into account during the 3D validation process. Notwithstanding, these runs show that FLUENT can be an accurate flow solver for modeling incompressible flow.

## A.4 Stage 2: 3D Fluent Validation

The next stage of CFD modeling was comprised of developing a 3D model of the flow field. The validation of the 2D FLUENT calculations with MISES established FLUENT as a flow solver. Thus, modeling in 3D can be used to generate correlation factors to relate the 2D prediction to the 3D flow profile. The 3D results are compared to test data, and are found to be with 5% of the measured data, so that it is validated as a flow solver. The results from this stage of modeling show that the point of minimum pressure is along the center of the passage span, making this the place where cavitation is most likely to occur.

### A.4.1 Stage 2 Modeling Scenarios

The first attempt of a 3D grid resulted in a rough quadrilateral structured 3D grid, and showed 3D FLUENT to be as a viable solver for such flows. More complex, finer grids were constructed until an unstructured tetrahedral grid showed no grid dependence on the solution. Comparisons of the beginning and end 3D grids are shown in Figure A.9. A 2d k-e model was also run at the same inlet conditions to compare the 2D and 3D flow properties. All of the runs presented converged without unsteady unresolved flow, showing that the small passage area quenches turbulent effects, making the flow essentially 100% laminar. A summary of the stage 2 models presented is shown in Table A.2.

**Table A.2 Summary of Stage 2 FLUENT runs (all runs with mass flow = 1 g/s)**

| Run name | # of cells | 2D/3D | Model | Turb. Specs. | inlet p (psi) | inlet v (m/s) |
|---|---|---|---|---|---|---|
| 3d_good | 1089540 | 3D | Laminar | -- | 29.09 | 7.46 |
| 3d_good_sa | 1089540 | 3D | Turbulent S-A | TVR = 4 | 29.78 | 7.43 |
| 2d_good_ke | 144890 | 2D | Turbulent k-e | 2 Zonal Wall | 27.86 | 6.49 |
| 3d_good_ke | 1089540 | 3D | Turbulent k-e | 2 Zonal Wall | 30.71 | 7.39 |
| 26_10 | 89960 | 3D | Laminar no BL | -- | 27.55 | 7.29 |

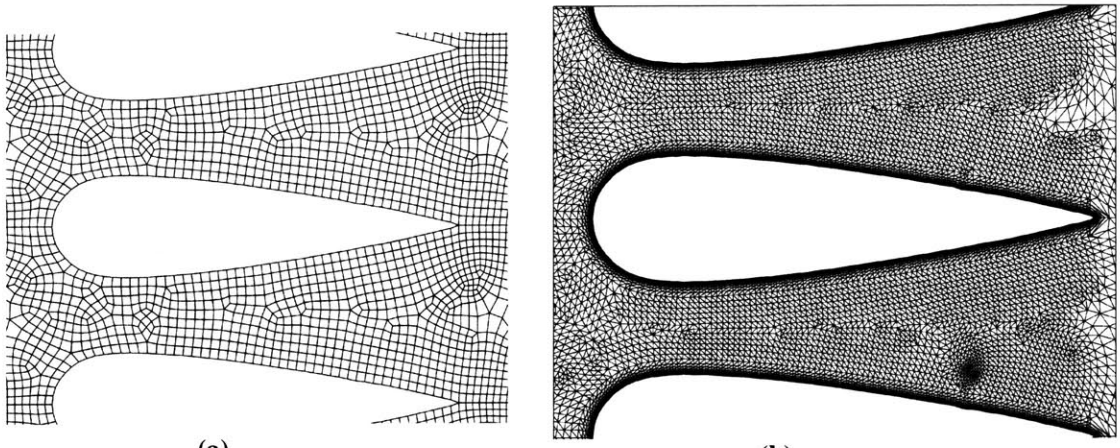

(a) (b)

**Figure A.9 Comparisons of 3D grid (plane taken through center of passageway) (a) rough quadrilateral structured grid with no boundary layer (b) refined unstructured mesh with an attached boundary layer**

## A.4.2 RESULTS

From the first of the 3D runs, results showed a much smaller $C_{pmin}$ than other 2D FLUENT runs a pressure recovery along the blade. As the final grid was run, there was even less pressure recovery along the blade, which is attributed to small passage area height (Figure A.11). Figure A.10 shows the lower pressure recovery along the blade due to 3D effects by comparing a 3D FLUENT pressure profile with the 2D profiles generated from MISES and 2D FLUENT.

Unlike the 2D results, a 3D laminar model converged, and running this grid with laminar and different turbulent models show results within 5% of each other, as shown in Figure A.11. These results indicate that the small passage area height quenches out the turbulent effects downstream [31], which means that either laminar or turbulent modeling can be used in 3D with the same accuracy. Furthermore, it is evident that the 3D laminar case best fits experimental data from Figure A.12,

which displays initial experimental data plotted against the 3D runs. Therefore, for later grid geometries and working fluids, a 3D laminar case was used in modeling.

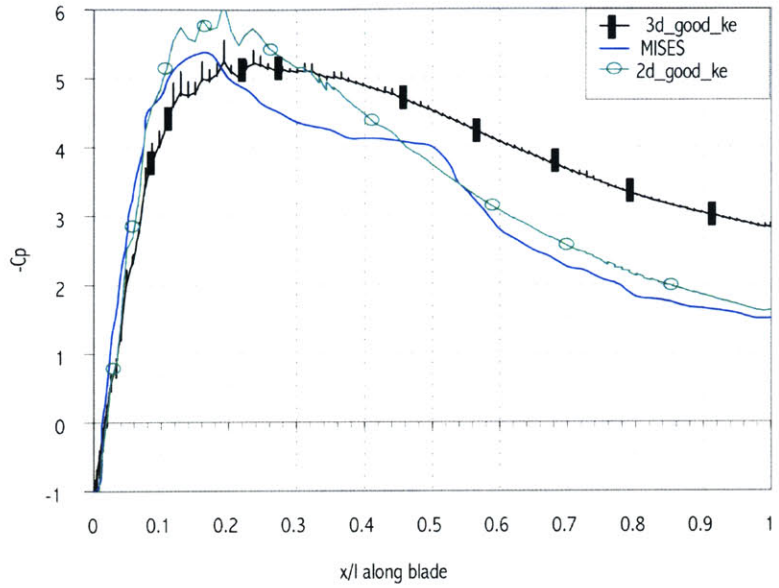


**Figure A.10 FLUENT $C_p$ Profiles for different runs, showing a lower pressure recovery for a 3D case compared to 2D case and MISES**

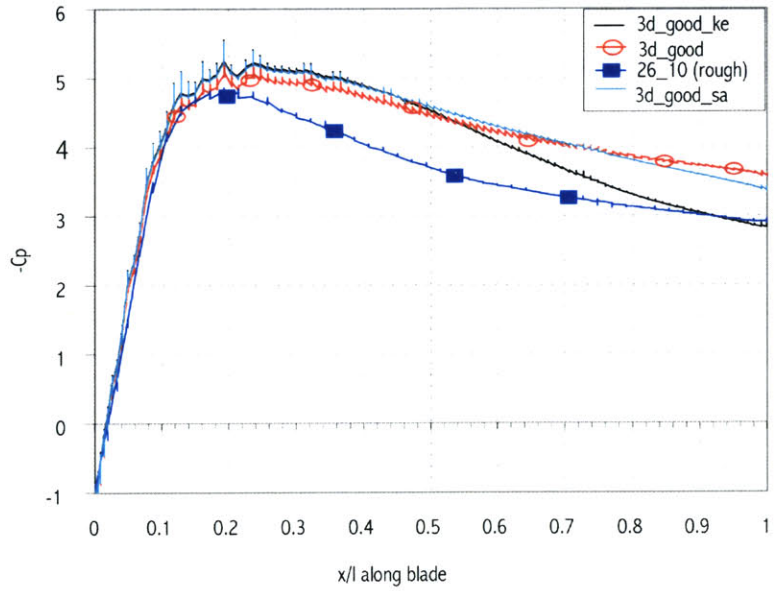


**Figure A.11 Fluent $C_p$ Profiles for different 3D Stage 2 runs, showing agreement with each other**

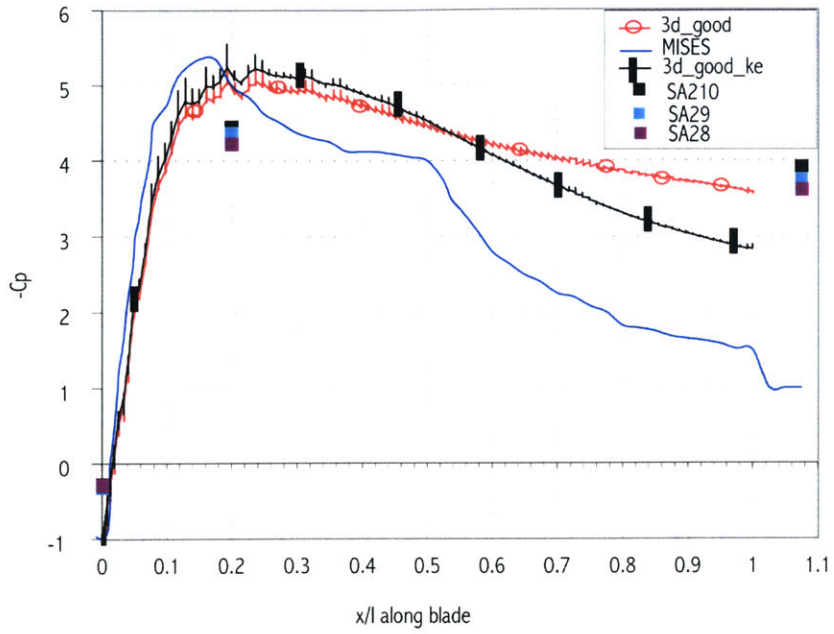


**Figure A.12 Fluent $C_p$ Profiles of 3D runs compared to MISES and initial experimental data. Note that the 3D laminar case best matches experimental data the best**

With a 3D model validated, the effects of the 3rd dimension on the pressure profile can be studied. These 3D characteristics can then be coupled with experimental and theoretical results to further explore cavitation. Figure A.13 depicts pressure profiles along the blade in the spanwise dimension. From the figure, it is evident that the point of minimum pressure occurs along the middle of the blade.

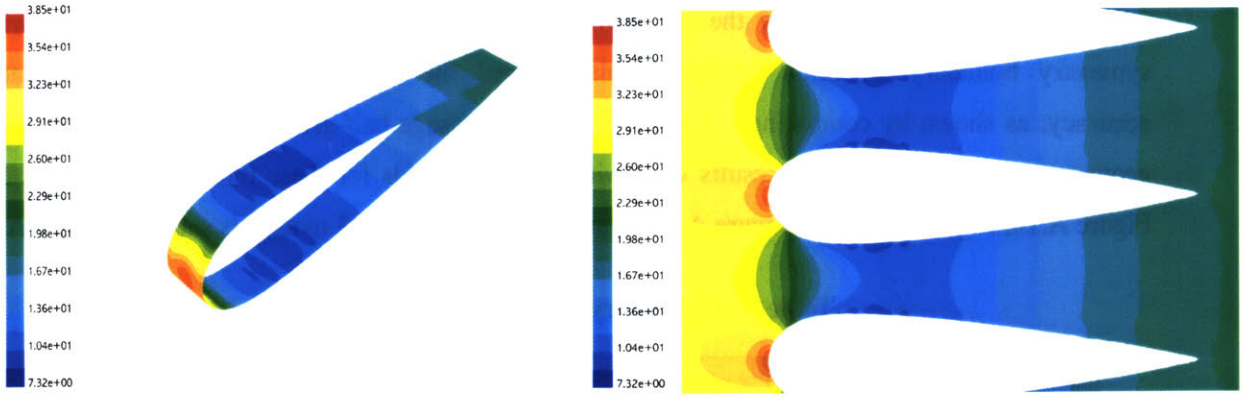


**Figure A.13 Static Pressure profiles along the blade of a 3D case. Note that point of minimum pressure occurs along the middle of the blade**

### A.4.3 CONCLUSIONS

Stage 2 of FLUENT modeling examined 3D effects on the pressure profiles showing that the point of minimum pressure occurs along the center of the blade. It also validated FLUENT as a 3D solver by comparing results with data. These comparisons showed that the 3D laminar case was the best since the small passage area quenches out significant turbulent effects in the modeling. This stage of modeling also determined the grid resolution to use for future grids. Further runs were constructed using different geometries and working fluids to compare to experimental data.

## A.5 STAGE 3: OTHER GEOMETRIES AND FLUIDS

Stage 2 of FLUENT modeling allowed for a viable grid generation scheme to produce accurately resolved grids for stage 3 of modeling. In order to resolve the top and bottom endwalls further, more cells were placed near the walls. These results were compared to experimental data in order to show that FLUENT is viable as a cavitation design tool. Ethanol and water were run with three different cascade geometries. Each model run simulated specific experimental conditions. This section presents the models and displays modeling results. Further comparisons with experimental data are presented in Chapter 5.

## A.5.1 MODELING SCENARIOS

Three grids were generated corresponding to the three different cascade geometries. In order to reduce computational time, only the top halves of the symmetric cascades were modeled, with a symmetry boundary condition imposed. This reduced the amount of cells, without impacting accuracy, as shown by comparing a symmetric 3 blade passage half-grid design with the full cascade geometry modeled in Stage 2. Results were within 0.12%. Grids for these three runs are depicted in Figure A.14, Figure A.15, and Figure A.16. A summary of the stage 3 models is shown in Table A.3.

**Table A.3 Summary of Stage 3 FLUENT runs**

| Run name | working fluid | # of cells | 2D/3D | Model | inlet p (psi) | inlet v (m/s) |
|---|---|---|---|---|---|---|
| 3d_sym_a_w | water | 260400 | 3D | Laminar | 108.96 | 15.25 |
| 3d_sym_b_w | water | 536740 | 3D | Laminar | 93.30 | 18.67 |
| 3d_asym_w | water | 469220 | 3D | Laminar | 45.44 | 16.06 |
| 3d_sym_a_e | ethanol | 260400 | 3D | Laminar | 123.25 | 14.73 |
| 3d_sym_b_e | ethanol | 536740 | 3D | Laminar | 98.025 | 14.87 |
| 3d_asym_e | ethanol | 469220 | 3D | Laminar | 47.716 | 10.12 |

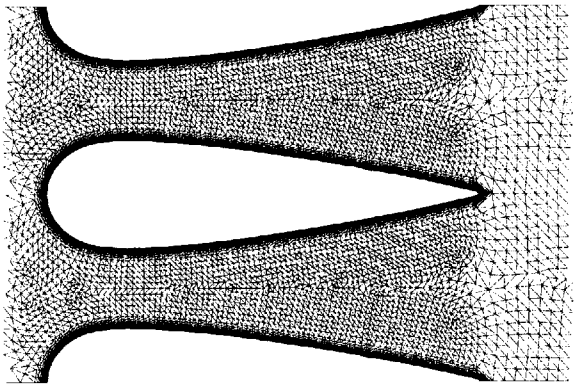

**Figure A.14 Grid of Symmetric Cascade A, with only half the cascade modeled**

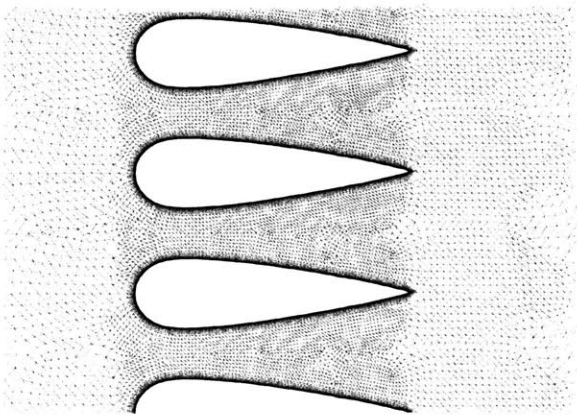

**Figure A.15 Grid of the Symmetric Cascade B, with 4 blades shown**

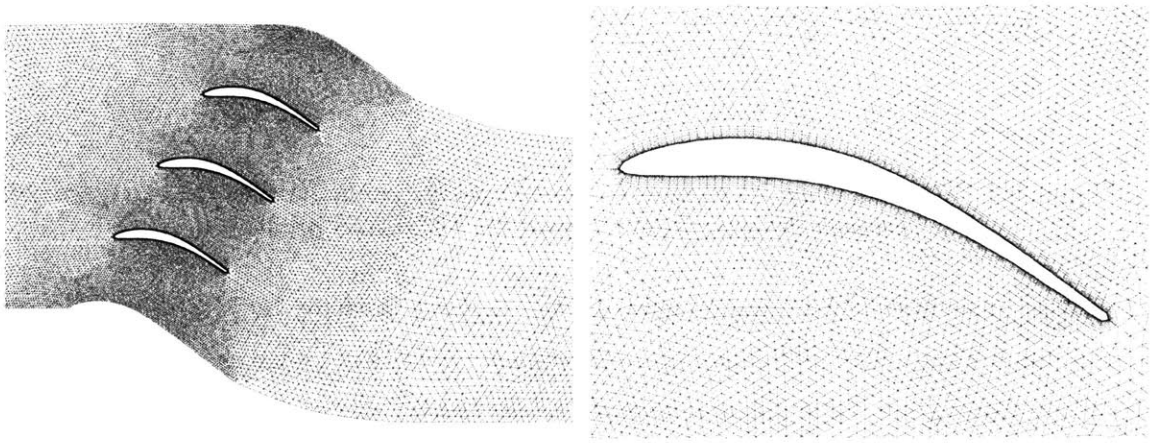

**Figure A.16 Asymmetric Grid, with the cascade and individual blade resolution shown in detail**

## A.5.2 RESULTS- WATER

As mentioned previously, the Symmetric A cascade matched the results from Stage 2, which predicts a much less pressure recovery than that predicted by MISES. The Symmetric cascade B with 9 blades showed an even lower minimum $C_p$ point, with correspondingly less pressure recovery. Therefore, adding more blades reduces the minimum point of pressure coefficient, thus making cavitation inception less likely. These results are incorporated into the numerical modeling of Section 3.5. Figure A.17 depicts the two symmetric cascade blade profiles along with the MISES predicted profile.

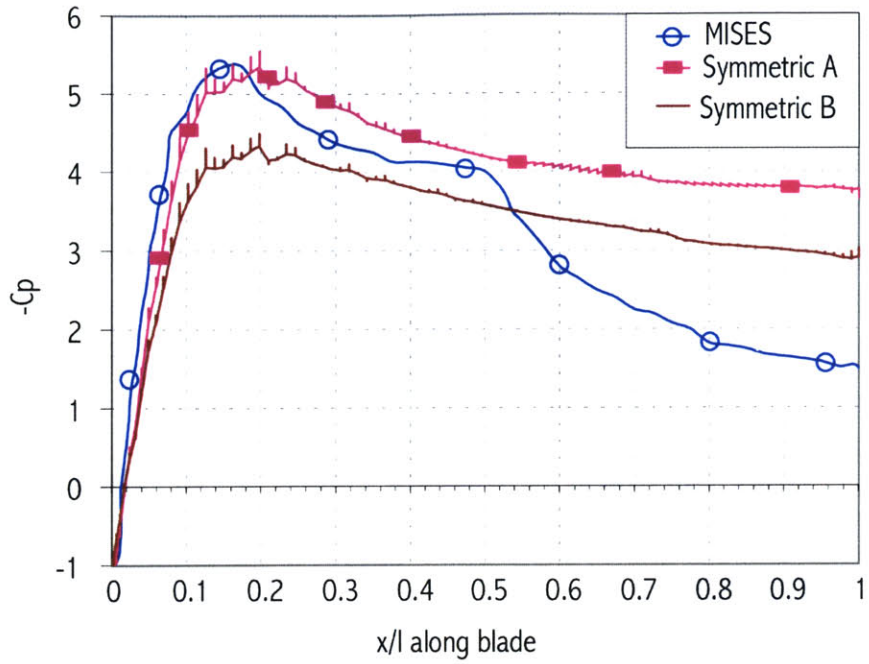


**Figure A.17 The final stage 3D FLUENT pressure profile predictions for the two symmetric cascade designs, plotted against the 2D MISES prediction**

The 3D asymmetric FLUENT solution showed major deviation from the 2D MISES pressure profile, as depicted in Figure A.18. 3D effects cause the pressure coefficient to remain negative at the end of the blade, showing very little pressure recovery on the suction side of the blade. Also, the point of minimum pressure occurs further downstream of the blade than predicted by MISES. These 3D effects and their implications on cavitation are discussed in Section 3.5.

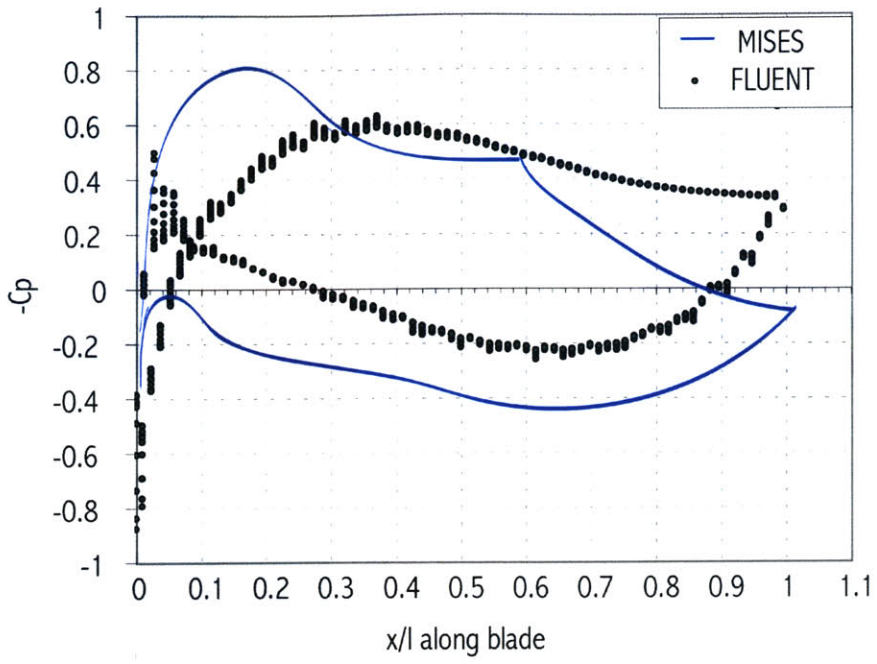


**Figure A.18 FLUENT asymmetric design pressure profile plotted against that predicted with MISES**

Figure A.19, Figure A.20, and Figure A.21 show the 3D static pressure profiles of the runs performed in stage three of the modeling. From these profiles, the dependence of pressure with distance from the top and bottom walls is shown to be small, with the lowest pressure usually occurring in the middle of the passageway.

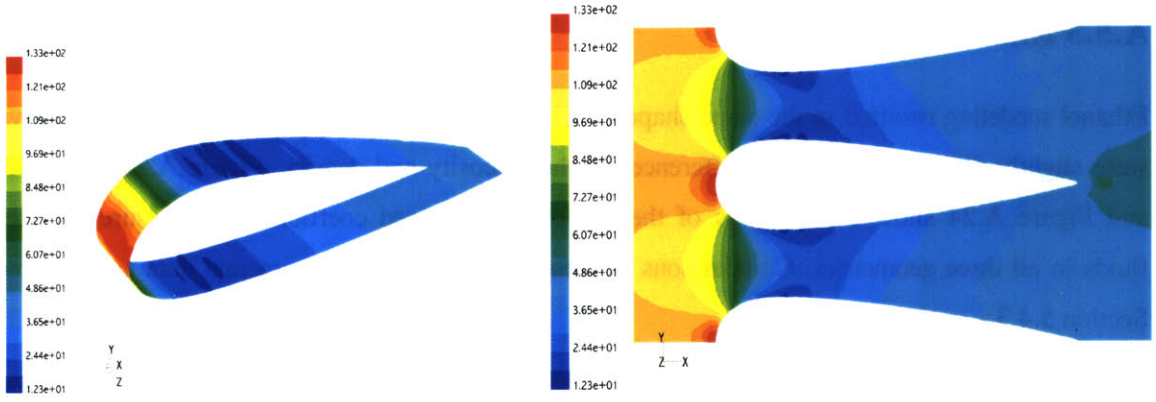


**Figure A.19 3D static pressure profiles for the symmetric cascade A**

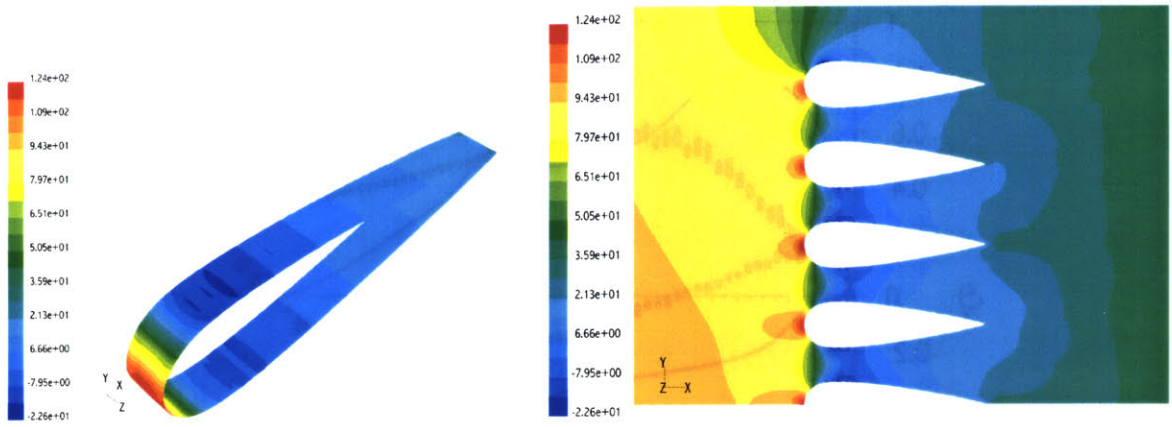


**Figure A.20 3D static pressure profiles for the symmetric cascade B**

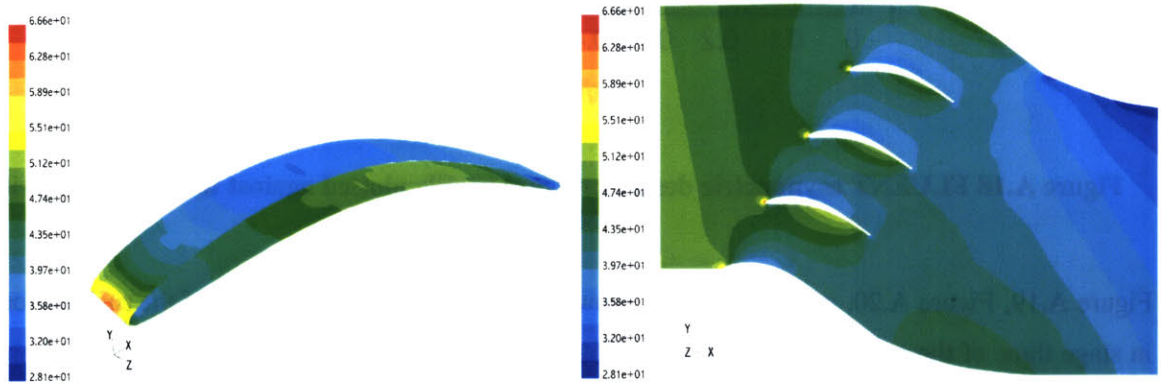


**Figure A.21 3D static pressure profiles for the asymmetric cascade**

## A.5.3 RESULTS- ETHANOL

Ethanol modeling resulted in the same shape of static pressure contours as water, although the values were slightly different due to the differences in the viscosity and density. Figure A.22, Figure A.23, and Figure A.24 show comparisons of the non-dimensionalized coefficient of pressure for the two fluids in all three geometries. Comparisons of these results against experimental data are presented in Section 5.4.3.

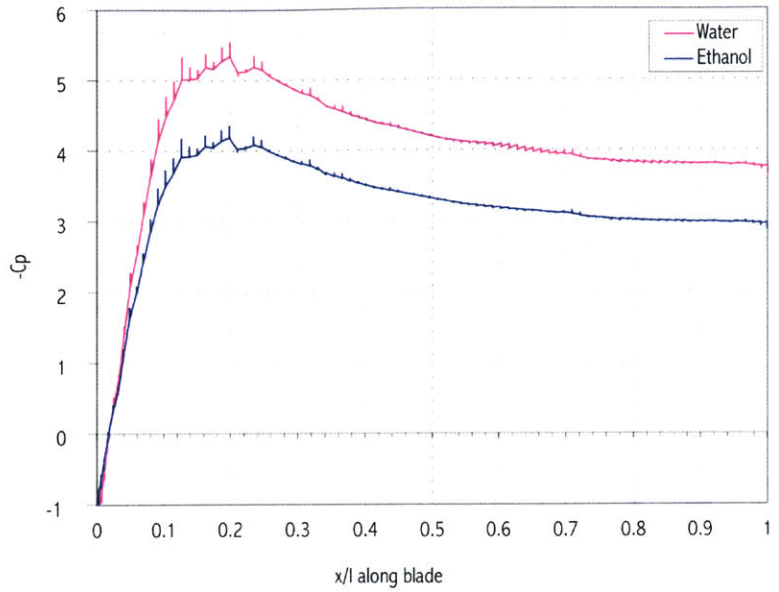


**Figure A.22 Water and Ethanol $C_p$ Comparisons for Symmetric Cascade A**

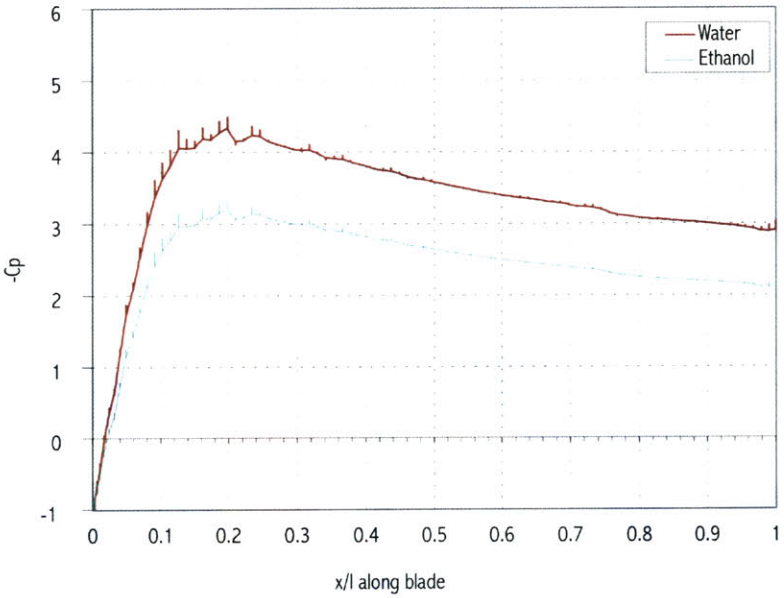


**Figure A.23 Water and Ethanol $C_p$ Comparisons for Symmetric Cascade B**

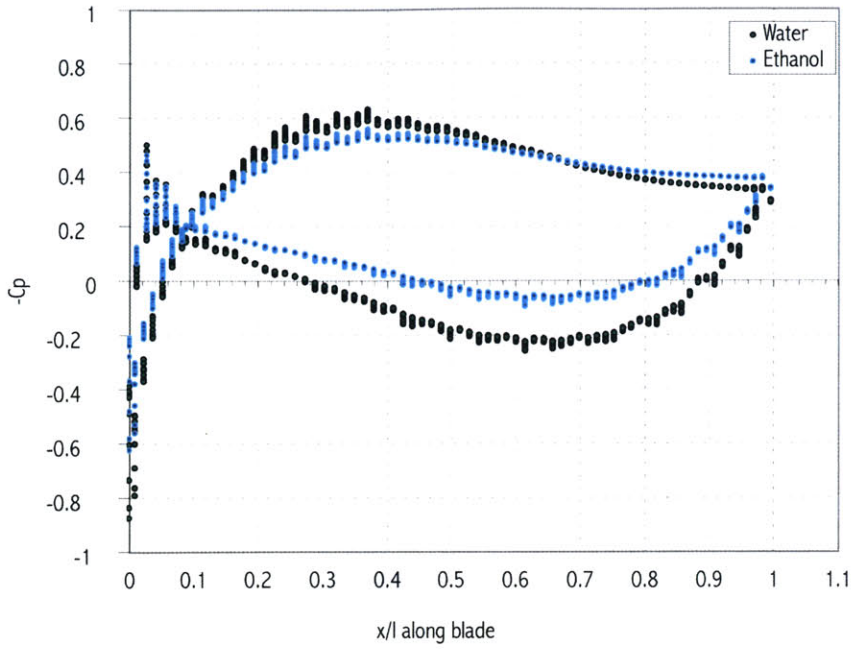


**Figure A.24 Water and Ethanol $C_p$ Comparisons for Asymmetric Cascade**

Figure A.25, FigureA.26, and FigureA.27 show the 3D static pressure profiles of the ethanol runs preformed in stage three of modeling. As with water, the dependence of pressure with distance from the top and bottom walls is shown to be slight, with the lowest pressure usually occurring in the middle of the passageway.

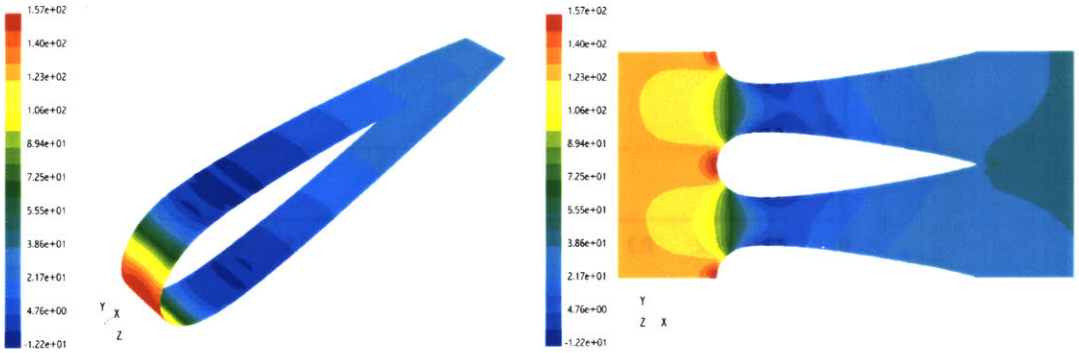


**Figure A.25 Static Pressure contours for ethanol dies for symmetric cascade A**

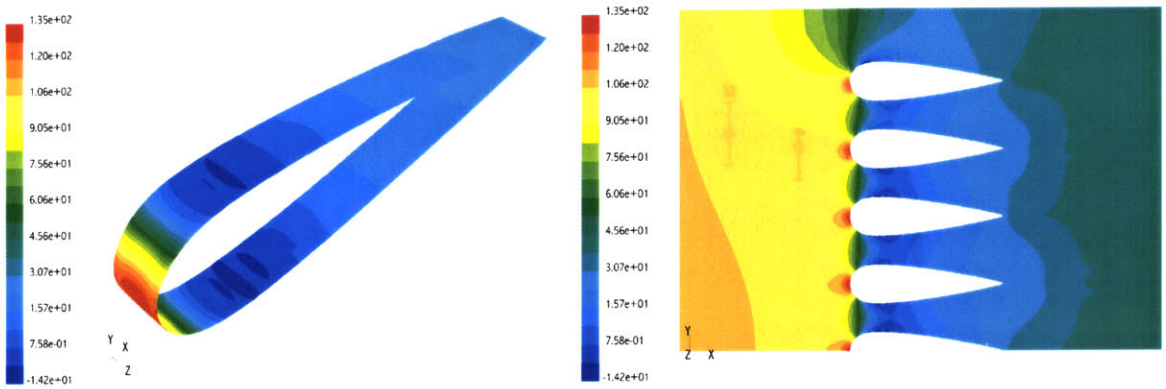


**FigureA.26 Ethanol static pressure Countours for Symmetric Cascade B**

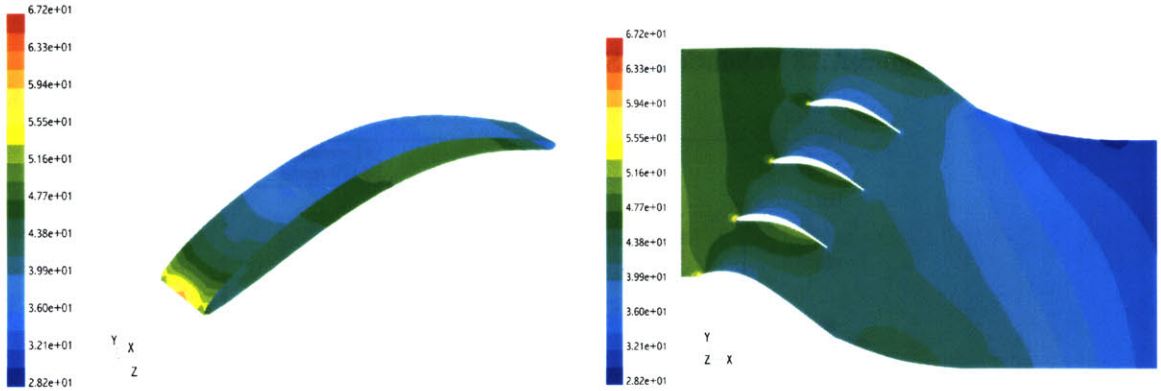


**FigureA.27 Ethanol static pressure contours for asymmetric cascade**

## A.5.3 EXPERIMENTAL VALIDATION

This section presents validation data for comparisons not showed in Chapter 5.

**Table A.4 FLUENT modeling inputs along with corresponding experimental inlet conditions for non-cavitating runs**

| Cascade Geometry | Working Fluid | Inlet pressure (psi) | | Mass Flow (g/s) | | Ave % difference |
|---|---|---|---|---|---|---|
| | | CFD | Experimental | CFD | Experimental | |
| Symmetric A | Water | | Water | 4.5% | 4.5% | 6.2% |
| | Ethanol | | Ethanol | 5.1% | 5.1% | 4.8% |
| Symmetric B | Water | | Water | 4.3% | 4.3% | 4.5% |
| | Ethanol | | Ethanol | 4.6% | 4.6% | 3.9% |

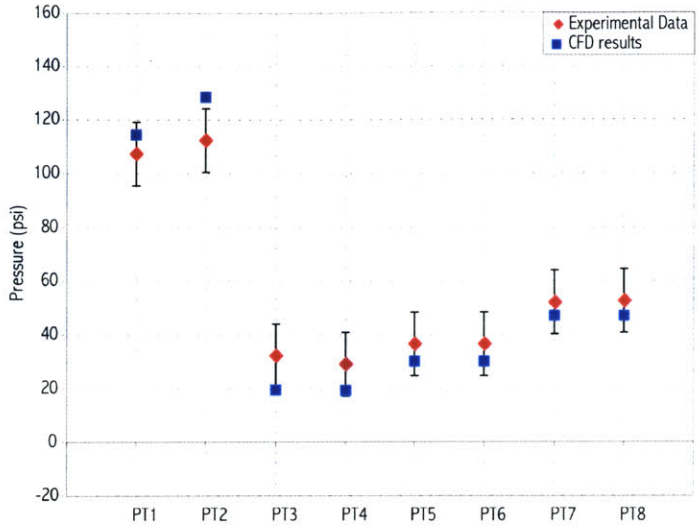


**FigureA.28 Validation of Symmetric Cascade A using ethanol**

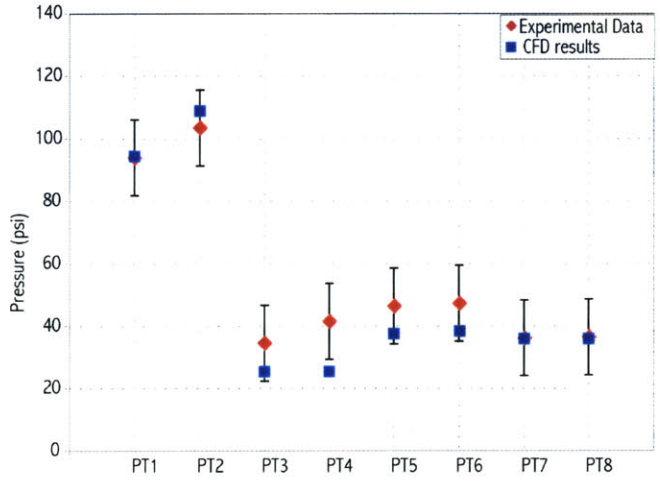


**FigureA.29Validation of symmetric cascade B using water**

## A.5.4 CONCLUSIONS

The main outcome of stage 3 of FLUENT modeling the 3D solutions of the cascade designs to compare with experimental testing. It is shown that 3D results very greatly from the MISES 2D prediction due to 3D endwall effects. From the results, more accurate predictions can be made about cavitation on a micro scale, as presented in Section 3.5. The solution can also be compared against experimental data, to prove the validity of FLUENT as a modeling tool, as presented in Chapter 5.

Finally, the effects of the 3rd dimension can be closely examined with respect to each design, to determine where cavitation inception would occur.

# APPENDIX B

## CAVITATION DEVICE FABRICATION PROCESS FLOW

This appendix contains the fabrication process flow followed in the fabrication of the cavitation device. Dr. Yoav Peles developed the process.

**Thermal Oxide & Alignment Marks**

1) RCA clean
2) Double side .3 um thermal oxide
3) HMDS
4) Spin thin photoresist
5) Expose alignment marks
6) Develop alignment marks
7) AME 5000 etch oxide from alignment marks
8) AME 5000 etch .5 um deep alignment marks

**Deep Etches (for both wafers)**

1) Flip wafer
2) HMDS
3) Spin thick photoresist
4) Expose features
5) Develop features
6) Coat other side with thin photoresist
7) BOE oxide
8) STS1 deep etch silicon

**Fusion Bond Wafers**

1) Overnight Acetone wafer dismount

2) Piranha wafers
3)
4) BOE strip oxide
5) RCA clean wafer
6) Evaligner fusion bonding
7) Annealing

**Anonic bond wafers to Pyrex**

1) Piranha wafers
2) Anonic bond wafers to Pyrex

# APPENDIX C

## MASKS USED IN FABRICATION

This appendix displays and explains the mask layers used in fabrication of the cavitation device.

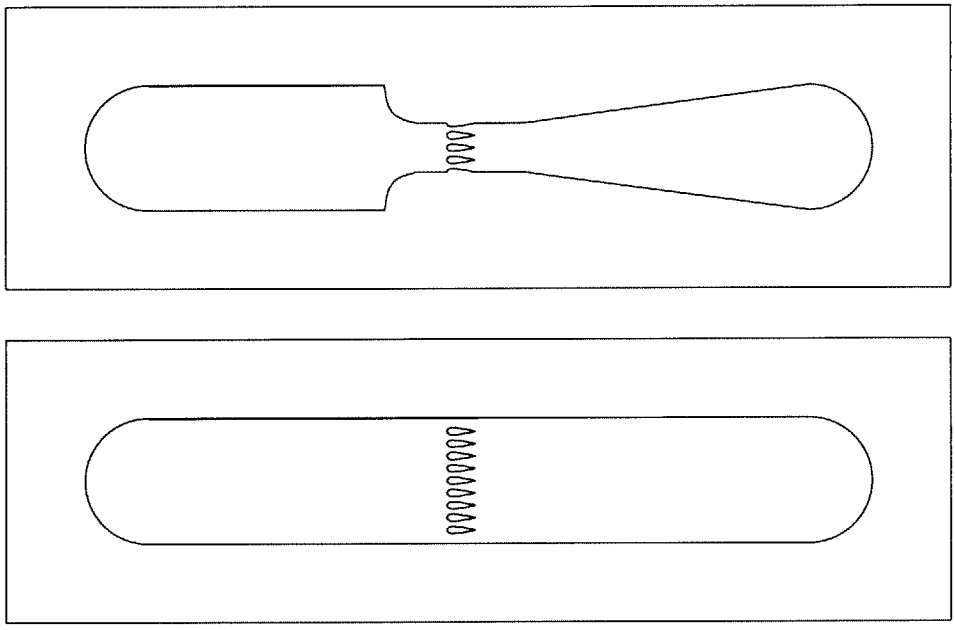

Mask #1

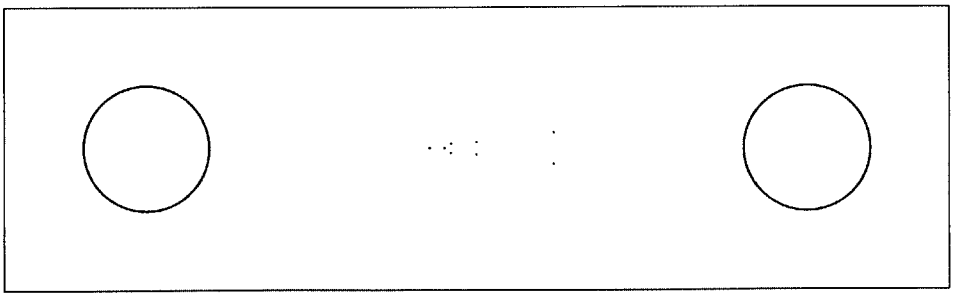

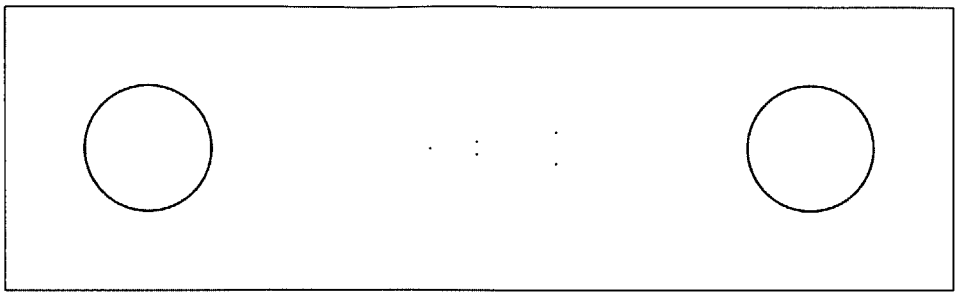

Mask #2 (build 2)

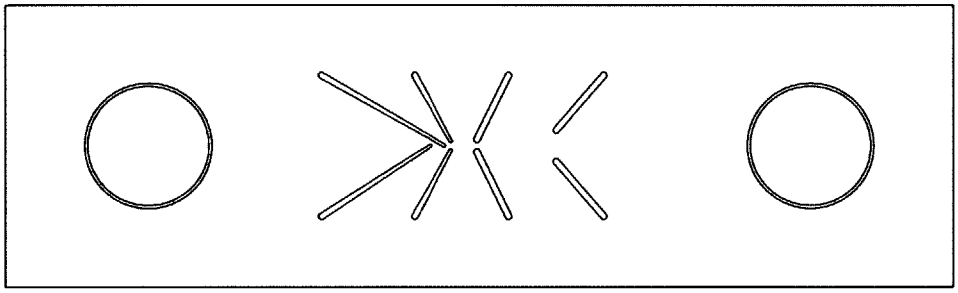

Mask #3

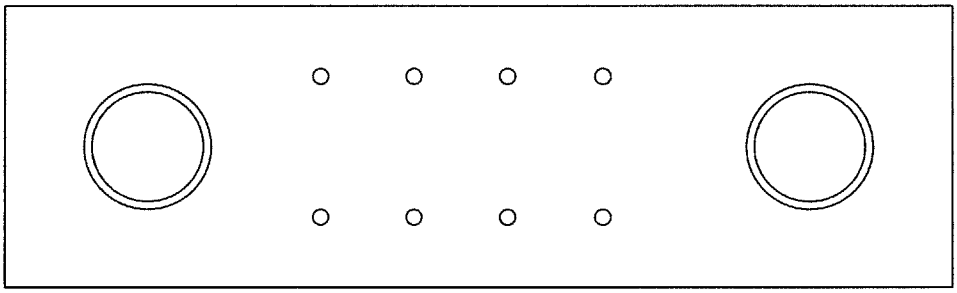

Mask #4

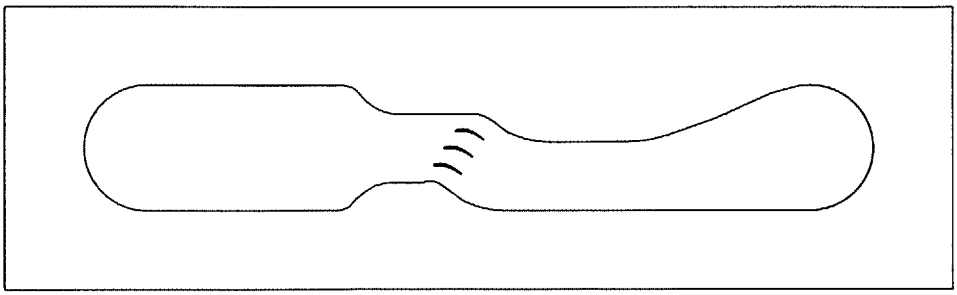

Mask #5

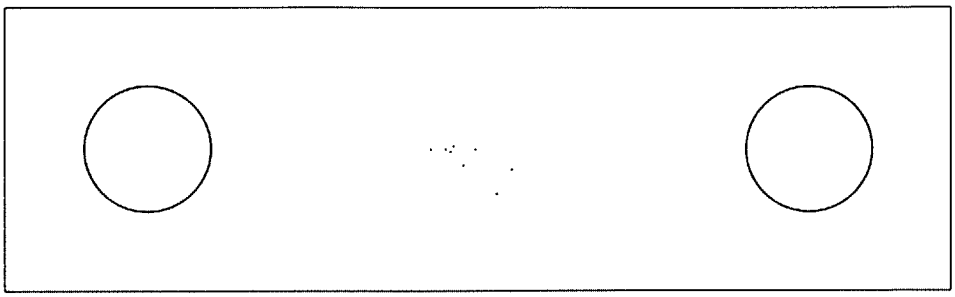

Mask #6

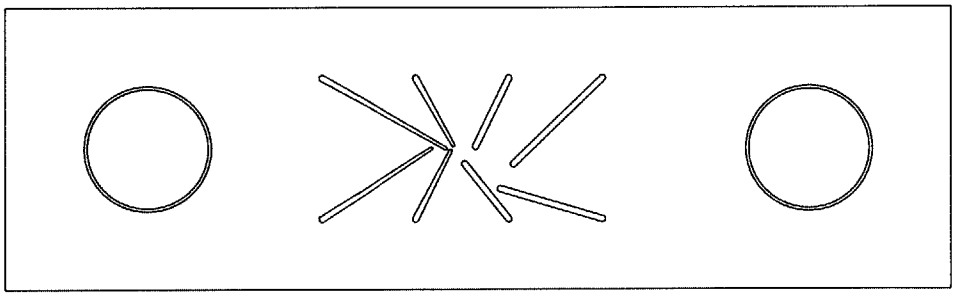

Mask #7

# APPENDIX D

## PACKAGING DRAWINGS

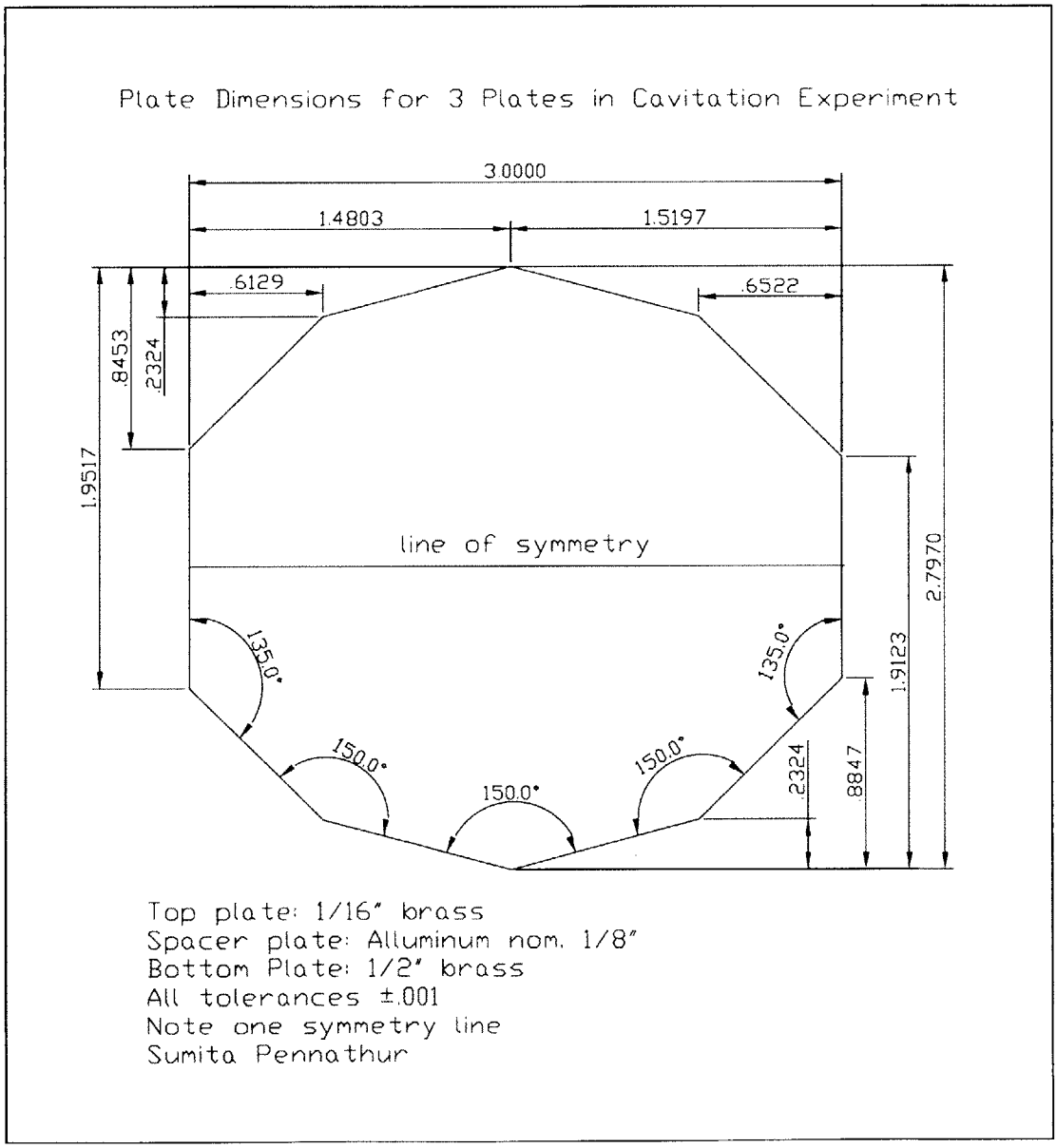

# Top Plate Cavitation Experiment

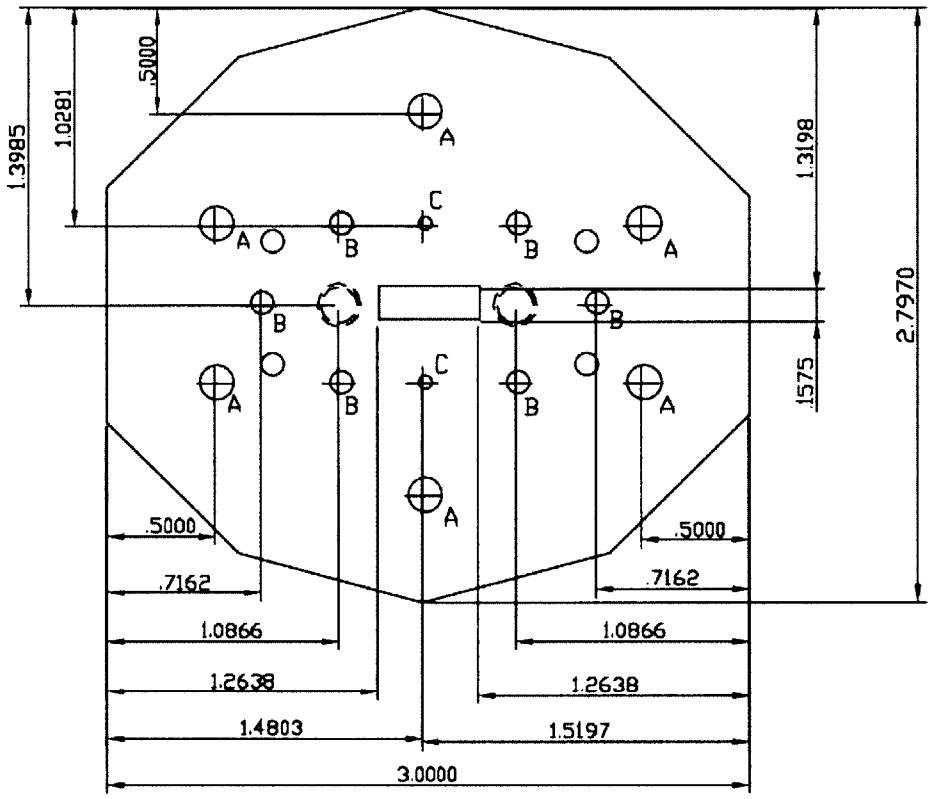


Legend for Holes

A: Clearance Holes for 8-32 Threads (6 holes)
B: Clearance Holes for 4-40 Threads (6 holes)
C: .0625 DIA Reamed Holes for Dowel Pins (2 holes)

Material: 1/16" thick brass
All tolerances are ±.001
Sumita Pennathur

Top Plate x-sec Cavitation Experiment

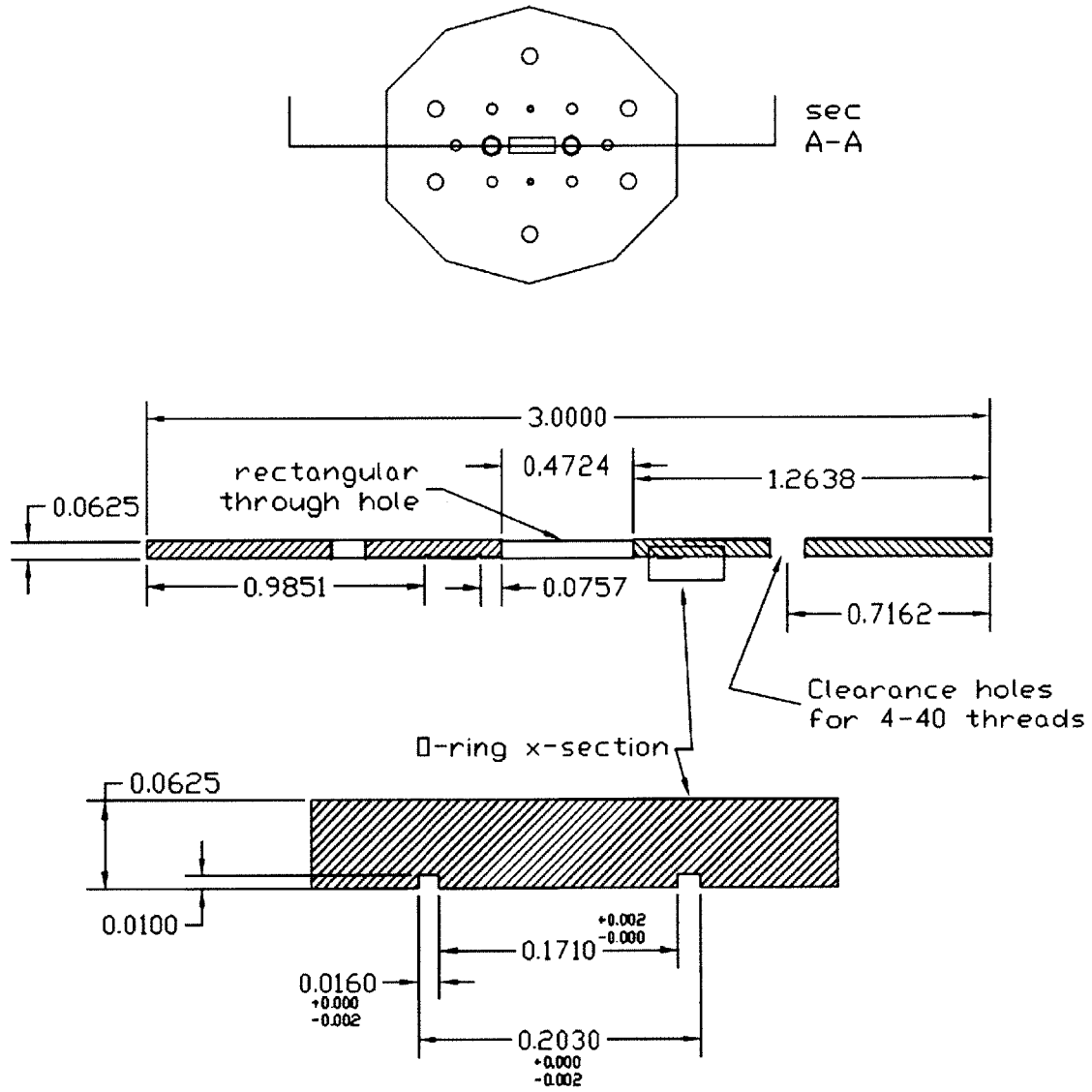


---

Material: Stainless Steel 1/16" thick
Tolerance ±0.001 unless otherwise noted

Sumita Pennathur

Spacer Plate Cavitation Experiment

Dimensions of rectangular thru hole To Be Determined

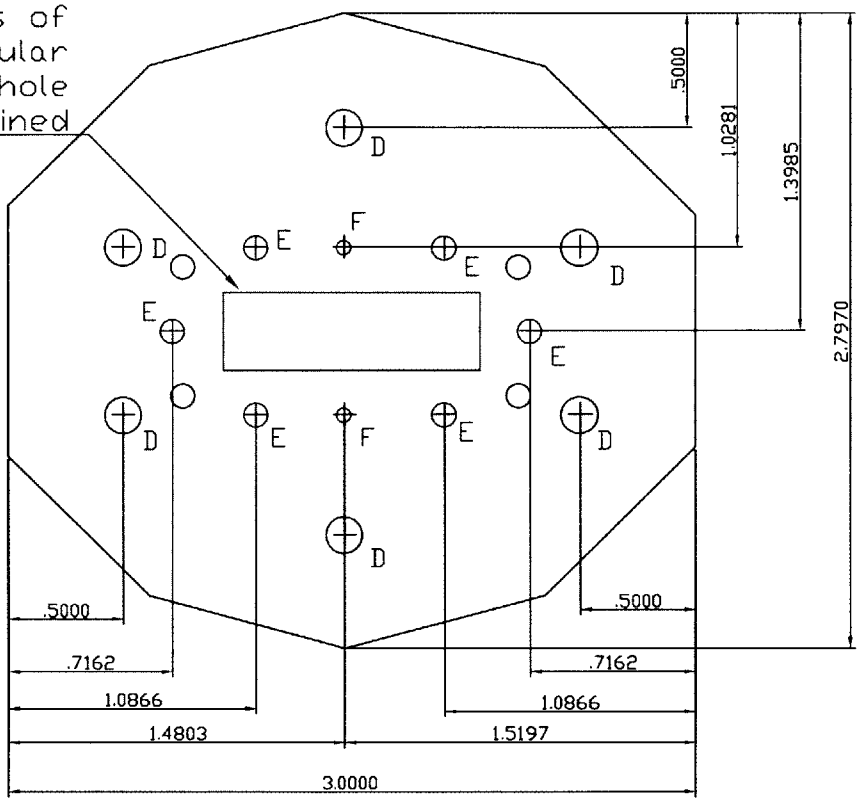


---

D: Clearance Holes for 8-32 Threads (6 holes)
E: 4-40 Threaded holes (6 holes)
F: .0625 DIA Reamed Holes for Dowel Pins (2 holes)

---

Material: Aluminum nom 1/8" (3/32")
All Tolerances are ±.001 unless otherwise noted
Sumita Pennathur

Bottom Plate Cavitation Experiment
1 of 4 pages

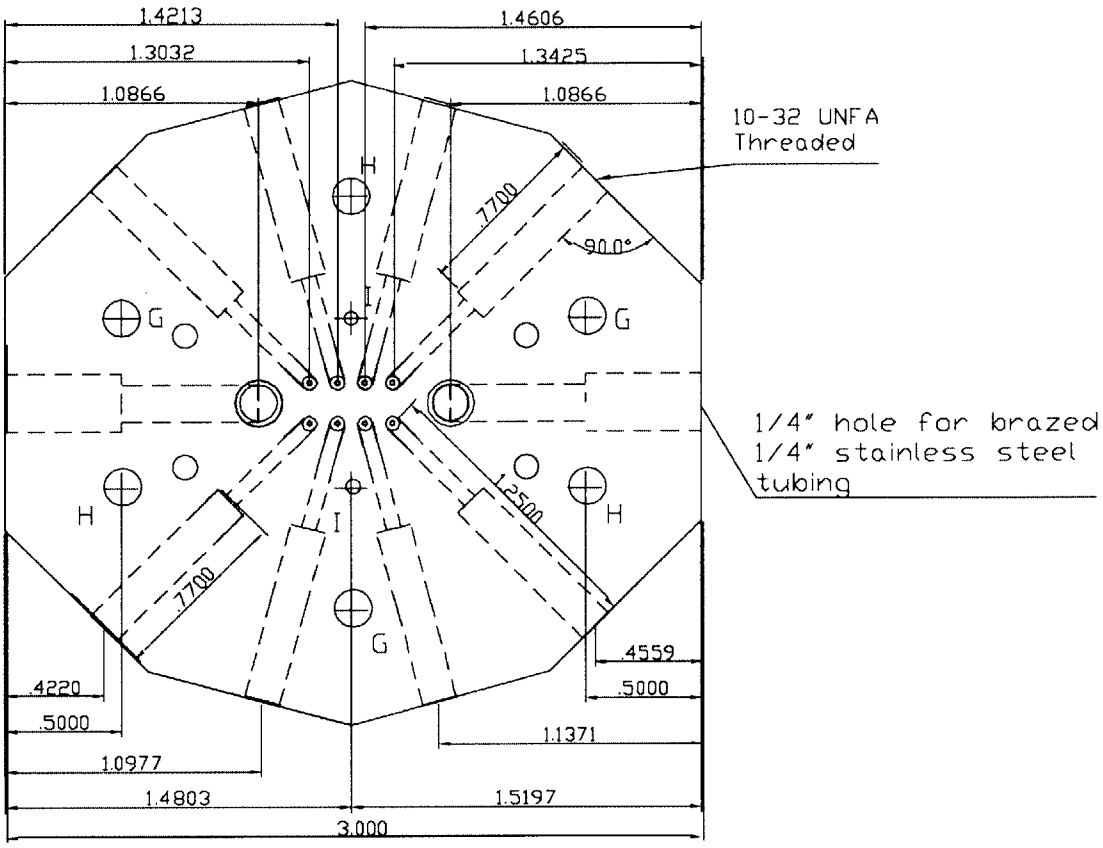


Legend for Holes
---
G: Threaded 8-32 Holes (3 holes)
H: Clearance holes for 8-32 Threads (3 holes)
I: .0625 DIA Reamed Holes for Dowel Pins (2 holes)

Material: 1/2" Brass
All tolerances ±.001 unless otherwise noted
Sumita Pennathur

Bottom Plate Cavitation Experiment
2 of 4 pages

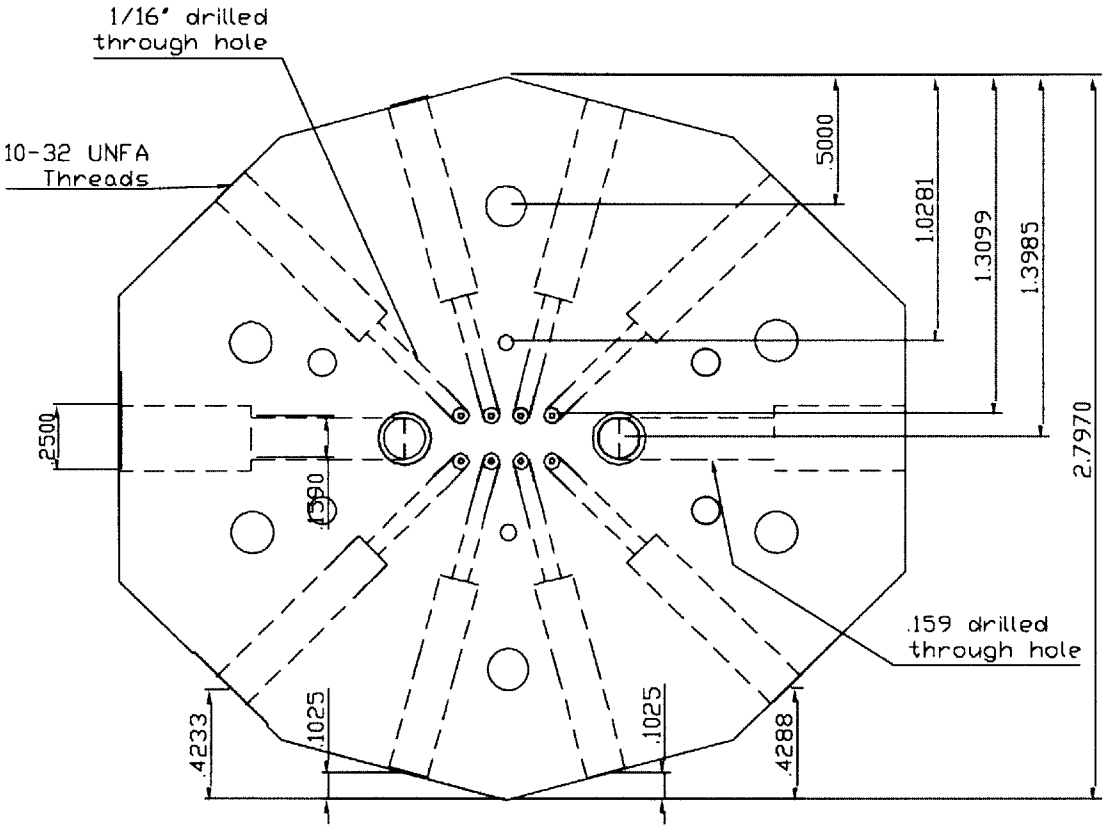


---

Holes specified on prior page
Material: 1/2" thick brass
All tolerances ±.001 unless otherwise noted
Sumita Pennathur

Bottom Plate Cavitation Experiment
Page 3 of 4

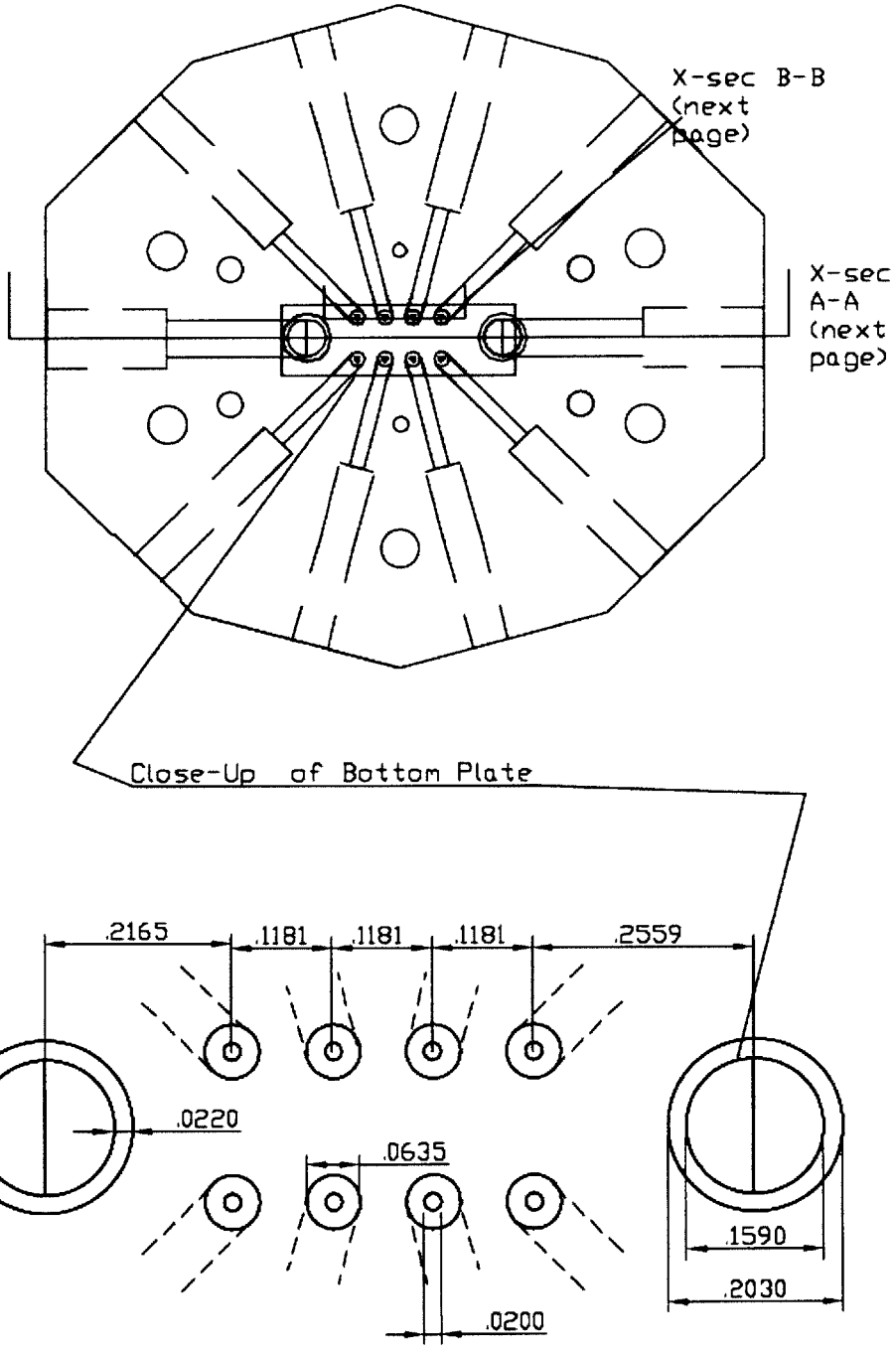

Bottom Plate Cavitation Experiment
Page 4 of 4

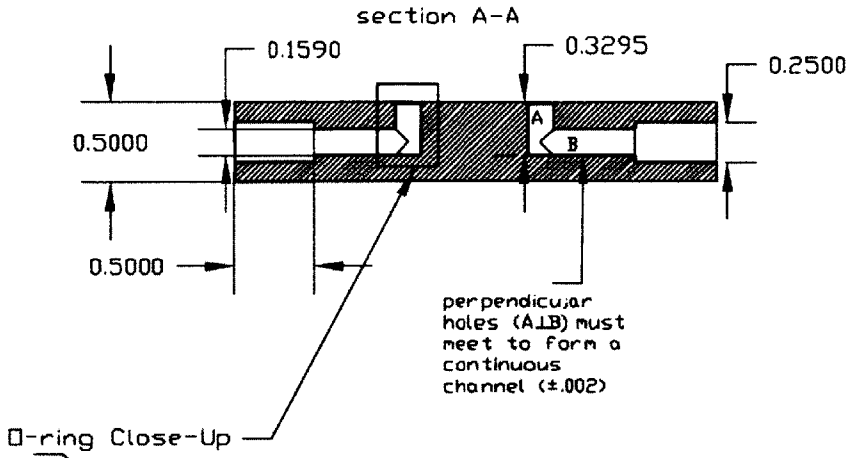


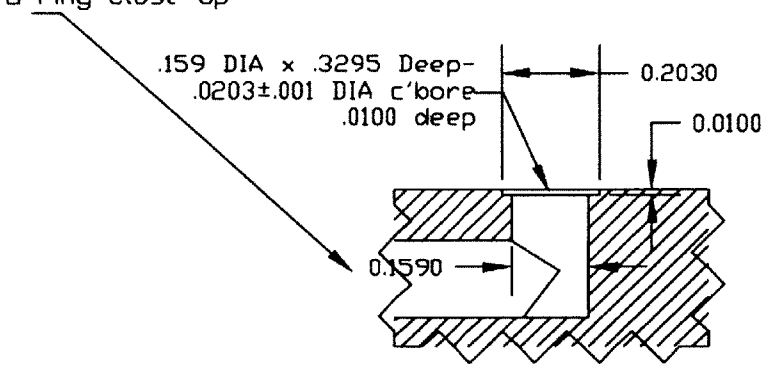


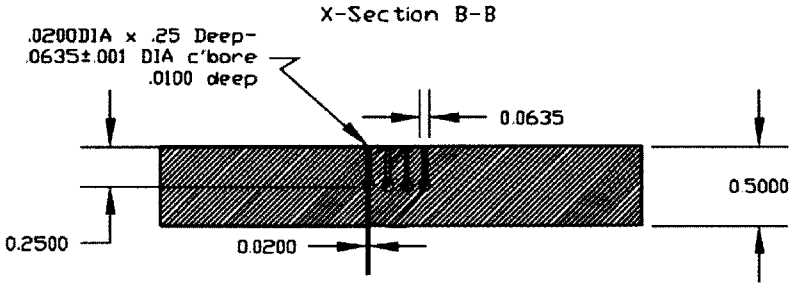


Material: 1/2" Alluminum
All tolerances ±.001 unless otherwise noted
Bottom Plae Cavtation Experiment
Sumita Pennathur

Steel Top Plate (build #2)
and further modifications

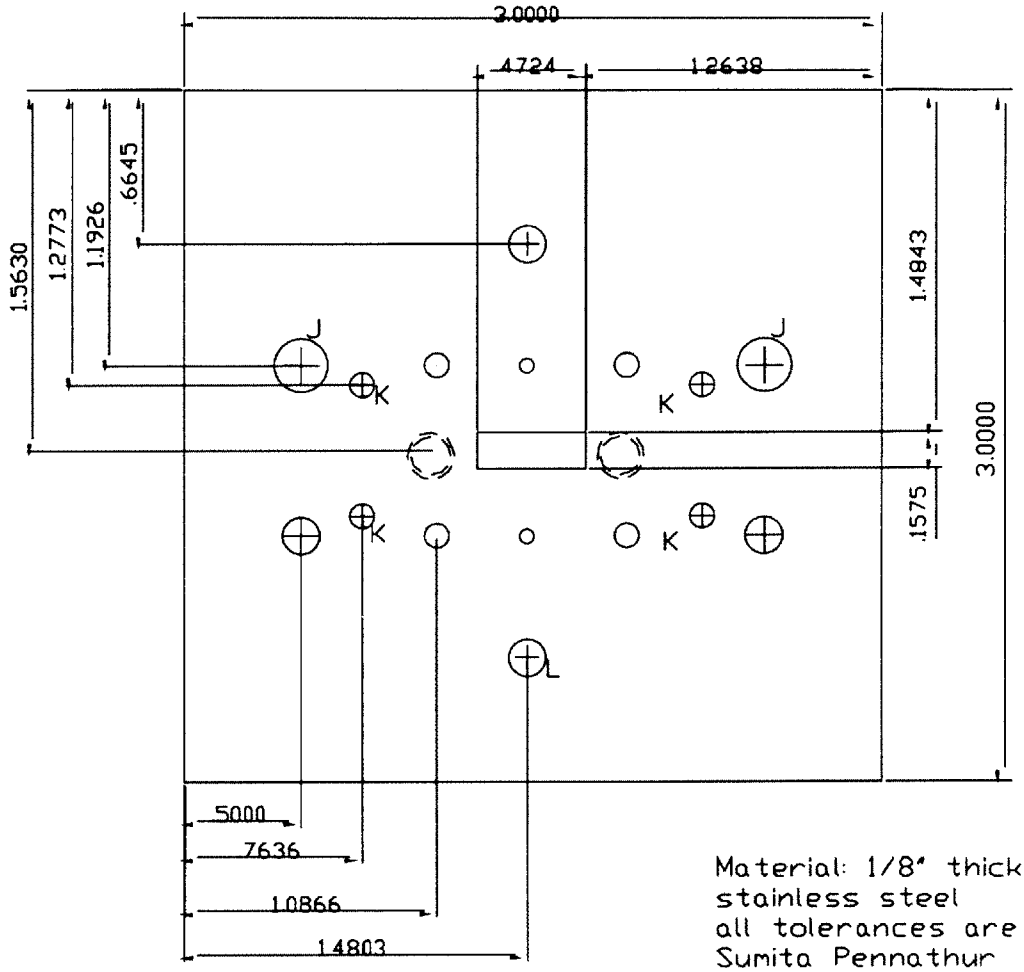


Material: 1/8" thick
stainless steel
all tolerances are ±.001
Sumita Pennathur

All holes as other plates
new legend must be applied to all plates

---

J: Clearance Holes for 1/4-20 threads
(2 holes)
K: Clearance Holes for 4-40 threads
(4 holes)
L: 10-32 clearance hole (1 hole)

# APPENDIX E

## EXPERIMENTAL CHECKLISTS

This Appendix shows copies of the checklists used in running the cavitation experiment. First, the checklist for changing dies, draining water, and filling water is presented

**Run Checklist for Turbopump Rig**:

**NOTES**: be careful with 3-way valves!!!!
Device 1 In must be ON for Device 2 In to work!

**A. SETUP**

1.Beginning Setup:
-make sure all valves are in the following position before starting any experiment:

| | |
|---|---|
| Supply Gage | OFF |
| Dump Gage | OFF |
| Supply Tank In | OFF |
| Supply Vent to ATM | closed |
| Dump Tank In | OFF |
| Dump Tank to ATM | closed |
| Device 1 In (supply tank) | OFF |
| 3-WAY (vacuum/gas) | OFF (up) |
| Device 2 In | OFF |
| DI Water Fill | OFF |
| Vacuum Gauge Valve | OFF |
| MFM valve (in back) | OFF |
| Supply Drain | closed |
| 3-WAY Device Out | OFF |
| Dump Drain | closed |
| 3-WAY Device In | OFF |
| Device 1 Ball Valve | closed |

**Initial Setup- Device 1:**
-This step allows for Device 1 to be the experiment ready to run
- Turn Device 1 Ball Valve OPEN
- Turn 3-WAY Device In to DEVICE 1

**Vacuum:**

-This step creates a vacuum for the supply tank and experiment

- Turn 3-WAY Device Out to DEVICE 2 (so that Dump tank is closed off)
- Turn ON MFM valve (in back)
- Turn ON vacuum gauge valve (in back)
- Turn ON Device 1 In
- Turn ON Supply Tank In
- Turn 3-WAY to VACUUM
- Turn ON Vacuum
- When vacuum is complete (check gauge),
- Turn OFF vacuum
- Turn OFF vacuum gauge valve
- Turn 3-WAY a little off (NOT fully off- be VERY CAREFUL)

**Fill Supply Tank and Experiment with Water**

-This step fills supply tank with water, then the experiment water (2 steps)

- Turn MFM valve OFF
- Turn Supply In OFF
- Turn DI Water Fill ON (Use Supply drain to drain)
- When supply tank is full, Turn Device 1 In OFF
- Turn MFM Valve ON
- When done (is sitegage in proper place?) Turn DI Water Fill OFF

- Calibrate MFM (since it is filled with water)

**Pressurize tanks**

-This step Pressurizes Supply and Dump tanks to proper pressure

- Turn MFM valve OFF
- Turn 3-WAY Valve all the way to GAS
- Turn Supply Gage ON
- Turn Dump Gage ON
- Turn Supply In ON
- Turn Pressure Regulator ON
- Pressurize to desired pressure (use supply vent to vent)
- Turn Regulator OFF
- Turn Supply In OFF
- Turn Dump In ON
- Turn Regulator ON
- Pressurize to desired pressure (use dump vent to vent)
- Turn Dump In OFF

**Run Experiment**

- Turn MFM Valve ON
- Turn 3-WAY Device Out to DEVICE 1
- Turn Device 1 In ON

- Running!!!

**B. Shutdown**

Drain Tank

- Turn 3-WAY Device 2 In to DEVICE 2
- OPEN Dump Drain

Purge Experiment

- CLOSE Supply Drain
- CLOSE Dump Drain
- Turn 3-WAY Device 2 Out to DEVICE 1
- Turn 3-WAY Device 2 Out to DEVICE 2
- OPEN Dump Drain
- CLOSE Dump Drain
- Turn Supply Gage OFF
- Turn Dump Gage OFF
- Turn Device 1 In ON
- Turn MFM Valve OFF
- Turn Supply Tank In ON
- Turn 3-WAY valve to Vacuum
- Turn Vacuum ON
- Turn MFM Valve ON
- Turn Supply In OFF
- Turn Dump In ON

Shutdown all valves

- Turn Vacuum OFF
- Turn Dump In OFF
- Turn MFM OFF
- Turn 3-WAY Device Out OFF
- Turn 3-WAY Device In OFF

**Changing dies:**

**NOTE:** Make SURE that you know the right orientation of the top and spacer plates in relation to the bottom plate- they CANNOT fit the other way, but it is tough to tell this from the naked eye!!

**NOTE**: Make sure dowel pins are in place before placing plates on top of each other

- Close off external connections (turn upstream ball valve off, downstream metering valve off)
- Move video equipment out of the way
- Unscrew Screws from top plate
- Remove top plate
- Put O-Rings aside into a plastic container to hold
- Remove die, place into appropriate container

- Put all bottom O-Rings into plastic container to hold
- Clean off bottom plate with your choice of solvent
- Replace O-rings with tweezers
- Place die in spacer plate, place onto bottom plate
- Put O-rings on top plate, place onto spacer plate
- Screw all screws back into place, all finger tight except for the two screws that screw into the table
- Replace video equipment

**Draining Water:**

Make sure all valves are open to allow flow through die:

- Device 1 IN → ON
- Upstream ball valve towards Device 1
- Downstream metering valve OPEN
- Device 1 OUT → ON
- All others → OFF

- ❑ Pressurize Supply Tank
  - Supply tank IN→ ON
  - Apply He pressure
- ❑ Let all remaining flow go to dump tank
  - It is very obvious when this is done, you will hear air sounds and see He flow through die on video
- ❑ Close Dump Tank Valve
  - Device 1 IN → OFF
- ❑ Close Supply tank and unpressurize
  - Supply Tank IN → OFF
  - Supply vent to atm → ON
- ❑ Drain Dump Tank
  - Dump Drain metering valve → ON
  - Make sure there is a container to catch the water
  - Put the old water into old water gallon jug
- ❑ Close Drain and Dispose of water
  - Dump Drain metering valve → OFF
  - Empty old water jug in nearest sink

**Filling Water**

- ❑ Fill Up Plastic Jug with new clean water
- ❑ Unpressurize He Tank
  - Close He Tank regulator off
  - Supply Tank → IN
  - Dump Tank → IN
  - Supply Tank vent to ATM → ON
  - Dump Tank vent to ATM → ON
- ❑ Turn Vacuum Supply ON
- ❑ Turn Dump Tank IN→ OFF
- ❑ Turn Supply Tank Vent to ATM → OFF
- ❑ Turn Device 1 OUT→ OFF
- ❑ Turn vacuum switch ON

- Monitor vacuum pressures on LabVIEW
- ❑ Turn DI water fill → ON
  - Monitor water level in plastic jug and in vacuum
  - make SURE no water goes into vacuum !!
- ❑ Turn off Vacuum Switch
- ❑ Turn off DI water fill ON→ OFF

**Initial Tests:**

- ❑ NOTE: High pressure testing first is recommended
- ❑ Pressurize both supply and dump tanks to a pressure
  - Switch to He Tank IN
  - Supply Tank → IN
  - Dump tank vent to atm → OFF
  - Dump Tank →IN
  - Device 1 out → ON
  - Turn on pressure regulator
- ❑ Check pressures on Labview
  - Make sure all pressure taps work
  - Make sure labview is on case xx
- ❑ Unpressurize
  - Turn off pressure regulator
  - Supply Tank vent to ATM→ ON
  - Dump Tank vent to ATM → ON
- ❑ First test
  - Vents to ATM→ OFF
  - Supply tank, Dump tank IN → ON
  - Pressurize supply tank and dunp tank to high pressure using regulator
  - Start recording xxx_down is name of labview file, where xxx is pressure
  - Dump tank IN→ OFF
  - Slowly vent dump tank to ATM
  - Stop as SOON as cavitation inception occurs → RECORD
    - if video recording, record timing
    - record data as xx_yy where xx is inlet pressure, yy is mass flow rate x 10
  - then release dump tank vent to atm and try to get max mass flow possible (max cavitation)→ RECORD
  - Stop recording data (put xx in place of data)
  - Turn Device 1 out → OFF & flow will stop
- ❑ Next tests
  - Turn Dump tank in → ON
  - Make sure dump tank and supply tank are at same pressure
  - Turn device 1 out → ON
  - Start recording xxx_down is name of labview file, where xxx is pressure
  - Dump tank IN→ OFF
  - Slowly vent dump tank to ATM
  - Stop as SOON as cavitation inception occurs → RECORD
    - if video recording, record timing
    - record data as xx_yy where xx is inlet pressure, yy is mass flow rate x 10
  - then release dump tank vent to atm and try to get max mass flow possible (max cavitation)→ RECORD

- Stop recording data (put xx in place of data)
- Turn Device 1 out → OFF & flow will stop

# APPENDIX F

## UNCERTAINTY ANALYSIS

### F.1 INTRODUCTION

This appendix presents a brief analysis of the uncertainty associated with the measurements and derived quantities presented in this thesis. The nomenclature used from representing the uncertainty is the fractional uncertainty, $S_x$, where $S_x$=Uncertainty in value of $x$/Indicated value of $x$. The uncertainty of the independent measurements is presented first, followed by a discussion of how these uncertainties are propagated to derived quantities.

### F.2 UNCERTAINTY OF INDEPENDENT MEASUREMENTS

#### F.2.1 PRESSURE

The pressure transducers were calibrated against pressure gauges with a stated accuracy of 0.25% full scale. For high pressure calibrations, the reference gauge was a 0-500psi gauge, so the accuracy of the reference pressure was ±1.25 psi. For the low pressure calibration, a 100 psi gauge was used, implying an accuracy of ±0.25 psi in the reference. The goal of each calibration was to determine a scale factor for the gauges which is multiplied by the difference between the gauge reading and the zero value taken prior to each run to determine the indicated pressure. For each transducer, the scale factor was within ±2% of the value indicated by the factory, and therefore it was assumed that the possible error in scale factor from run to run is ±2%, leading to a corresponding uncertainty in the pressure measurements. In addition to the error from the drift of the scale factor, there were variations in pressure measurements. For the calibrations at higher pressures, the variations in indicated pressure were within ±2 psi. For lower pressure calibration, the variations in pressure are within ±0.5 psi.

Therefore, the estimates of uncertainty for the pressure measurements were as follows:

$$S_P = \begin{cases} \pm 0.02 \pm \dfrac{2\,psi}{P} & \text{for P >100psia} \\ \pm 0.02 \pm \dfrac{0.5\,psi}{P} & \text{for P<100 psia} \end{cases}$$

### F.2.2 MASS FLOW

The liquid mass flow was measured using a factory-calibrated Micro Motion Elite CMF010 meter. They have a stated accuracy for liquid flow of:

$$S_{\dot{m}} = \pm 0.002 \pm \frac{0.0033 g/\sec}{\dot{m}}$$

The second term is the zero stability of the meter. For a typical flow rate of 1 g/s, this corresponds to an uncertainty of 0.005 g/sec, or $S_m = \pm 0.5\%$.

### F.2.3 CAVITATION ZONE LENGTH

The cavitation zone length is visually observed on a video screen and measured with respect to the blade. A conservative estimate on the accuracy of these measurements have been determined to be:

$$S_l = \pm 0.5$$

Since there is no zero stability of the observed reading, the accuracy will always remain ±0.5.

## F.3 UNCERTAINTY OF THE DERIVED QUANTITIES

The uncertainty of each of the derived quantities is propagated from the uncertainty in the independent measurements as follows. If $y$ is the quantity in question, it is written as a function of the independent measurements $x_1, x_2 \ldots, x_n$:

$$y = f(x_1, x_2, \ldots, x_n)$$

A set of influence coefficients, $C_{xi}$, are defined, which are essentially non-dimnsionalized partial derivatives of $y$ with respect to each variable:

$$C_{x_i} = \left| \frac{\partial f}{dx_i} \left( \frac{x_i}{y} \right)_0 \right|$$

where the subscript *0* refers to the indicated and calculated values at the point of interest. The value of $C_{xi}$ represents the percentage change in $y$ that would results from a one percent change in the input $x_i$. The overall fractional uncertainty $S_y$ is then:

$$S_y = \sqrt{\sum_{i=1}^{n} \left( C_{x_i} S_{x_i} \right)^2}$$

For the cases blow when $C \neq 1$, the actual calculation of the influence coefficients is done numerically, by varying each input slightly and observing the change in output.

### F.3.1 Pressure Coefficient

The pressure coefficient is determined by the following equation:

$$-C_p(s) = \frac{p_0 - p(s)}{\frac{1}{2}\rho V^2}$$

Where $p$ and $V$ are measured quantities. In this case, $C$ is not 1. Therefore, Table x.x shows an example case for the calculation of pressure coefficients. The propagated $S_{Cp} = \pm 2\%$.

**Table F.1 Example of uncertainties of pressure coefficient**

| $x_i$ | $C_{xi}$ | $S_{xi}$ |
|---|---|---|
| $p_0$ | .50 | 2% |
| $p(s)$ | .50 | 2% |
| $V$ | .50 | 1% |
| $\rho$ | 0 | 0% |
| $C_p$ | .25 | 2% |

# APPENDIX G

## COMPLETE BUILD #2 RESULTS

### G.1 HYSTERESIS RESULT EXAMPLES

| Inception Pressure | Mass Flow | Nondimensionalized zone length | Desident Pressure |
|---|---|---|---|
| 80psi | 2.5 g/s | 0.5 | 89psi |
| | | 1.0 | 95psi |
| | | 1.5 | 98psi |

| Inception Pressure | Mass Flow | Nondimensionalized zone length | Desident Pressure |
|---|---|---|---|
| 60psi | 2.5 g/s | 0.5 | 63psi |
| | | 1.0 | 65psi |
| | | 1.5 | 67psi |

| Inception Pressure | Mass Flow | Nondimensionalized zone length | Desident Pressure |
|---|---|---|---|
| 100psi | 3.0 g/s | 0.5 | 105psi |
| | | 1.0 | 123psi |
| | | 1.5 | 136psi |

| Inception Pressure | Mass Flow | Nondimensionalized zone length | Desident Pressure |
|---|---|---|---|
| 100psi | 3.5 g/s | 0.5 | 111psi |
| | | 1.0 | 125psi |
| | | 1.5 | 138psi |

| Inception Pressure | Mass Flow | Nondimensionalized zone length | Desident Pressure |
|---|---|---|---|
| 100psi | 3.6 g/s | 0.5 | 112psi |
| | | 1.0 | 125psi |
| | | 1.5 | 138psi |

## G.2 Performance Loss Curves

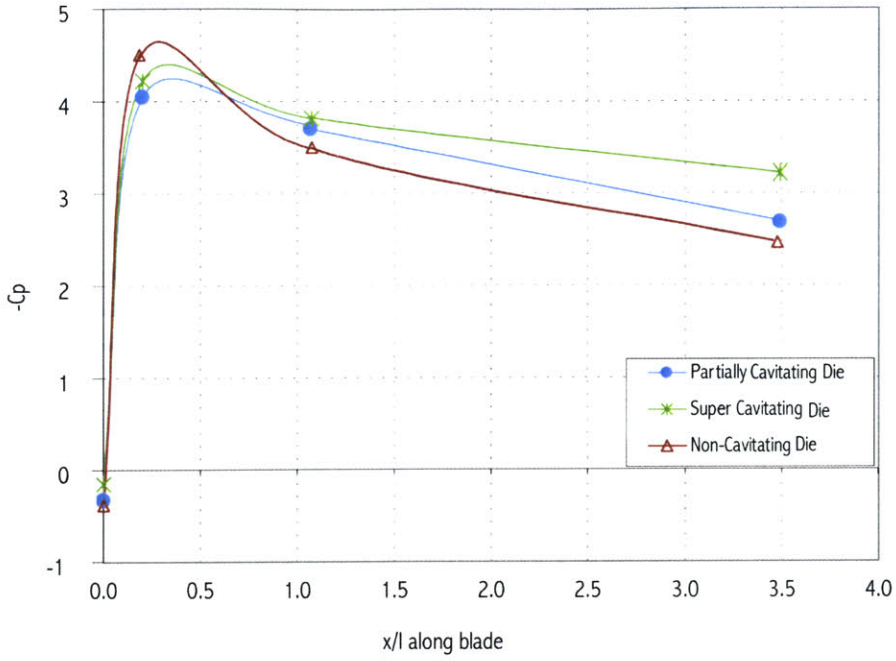


**Figure G.1 Symmetric cascade A (Die AH3) with Water**

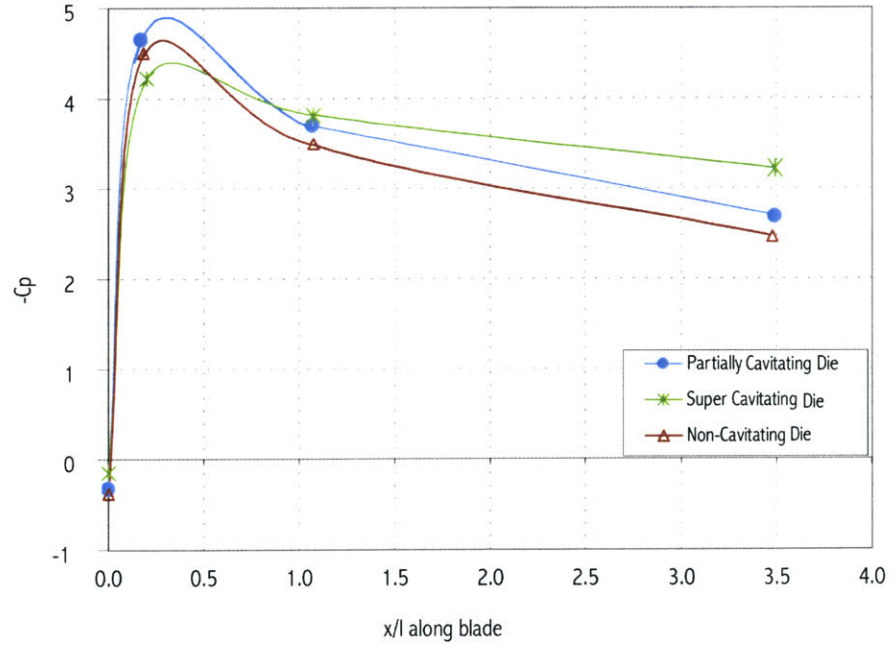


**Figure G.2 Symmetric cascade A (Die AH3) with Ethanol**

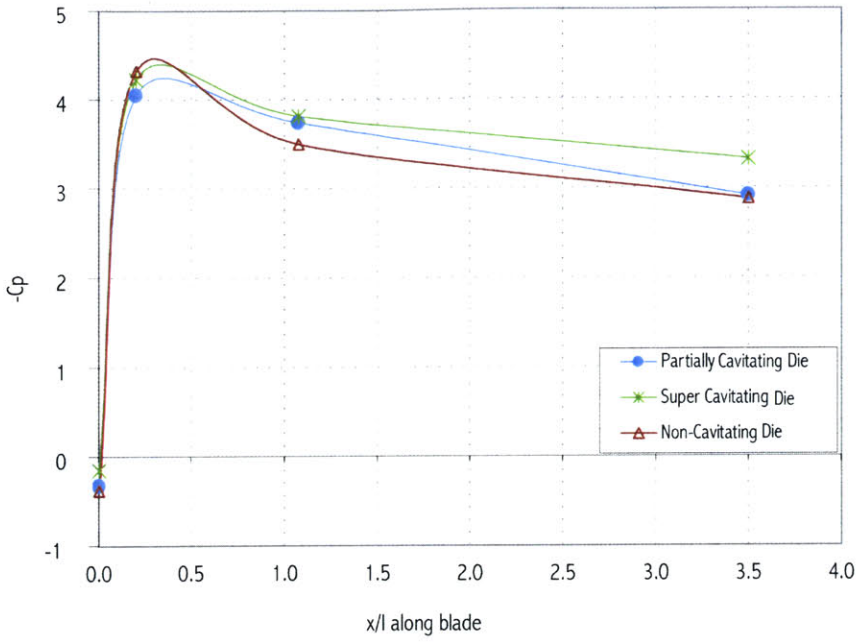


**Figure G.3 Symmetric cascade B (Die BH7) with Water**

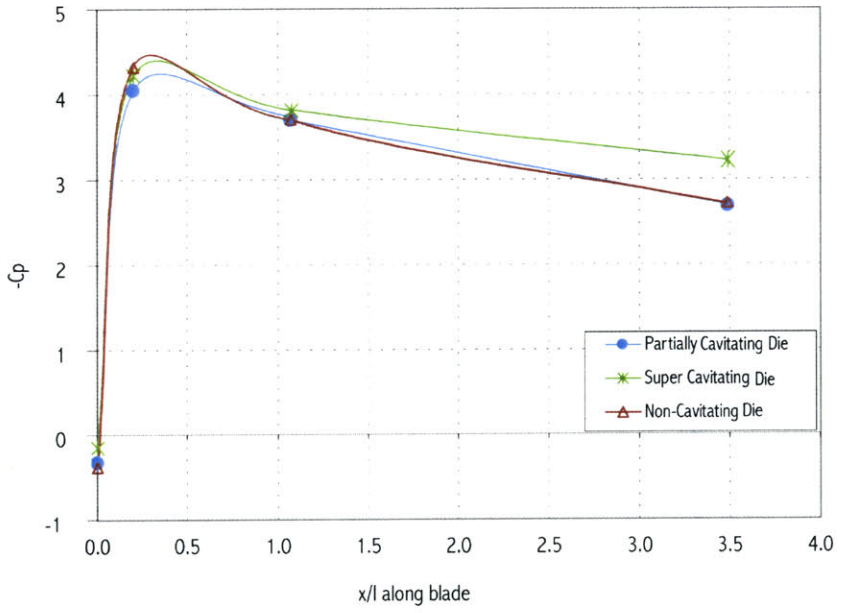


**Figure G.4 Symmetric Cascade A (Die BH7) with**

## G.3 Cavitation Zone Length - Ethanol

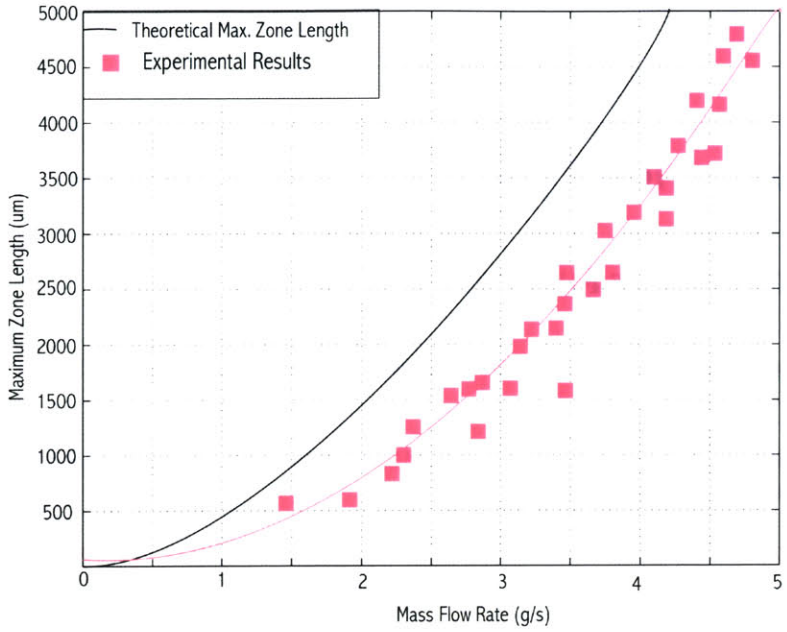


**Figure G.5 Symmetric Cascade A**

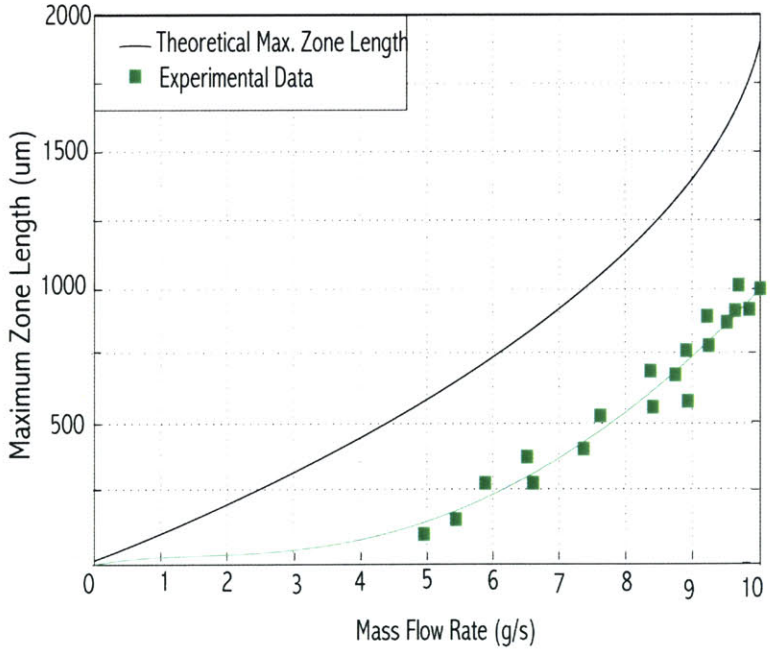


**FigureG.6 Symmetric Cascade B**

# APPENDIX H

## DATA REDUCTION CODES

### H.1 CFD TO DATA FIT FUNCTION

This code fits polynomial functions to the data points interpolating from 3D CFD results.

```
kul = [];
oldms = [1387.5690 1355.5643 1368.4236 1452.6823 1355.1614 1350.0479]';
%slopes from 1st calibration...

names = {'Pressure' 'Massflow' 'CFD' 'SymA' 'SymB' 'Lam'};


[cal51,date51] = loadcal(51);
test = cal51([20 50 79],1:8);
cal51 = cal51(1:end,:);
cidx = find(diffnext(cal51(:,11)) ~= 0);
vals1 = cal51([cidx],1:10);
pvec1 = cal51([cidx+1],11);

[cal52,date52] = loadcal(52);
cal52 = cal52(1:end,:);
cidx = find(diffnext(cal52(:,11)) ~= 0);
vals2 = cal52([cidx],1:10);
pvec2 = [cal52(cidx+1,11)];

pvec = [pvec1 ; pvec2];
vals = [vals1 ; vals2];

zidx = 125:216;

figure(2)
for i = 1:6
  meanzero(i) = mean(cal52(zidx,i));
  meanzero(i) = cal51(1,i);
  kul(i).dat = [vals(:,i)-meanzero(i)];
  [p,s] = polyfit([pvec],[kul(i).dat],1); %first order, linear fit..
  if i > 10
    figure(2)
    orient landscape
    subplot(2,2,i-4)
  else
    figure(1)
    %orient landscape
```

```
    %subplot(2,2,i)
    subplot(3,2,i)
  end
  [plotvals,delt] = polyval(p,[0;max(pvec)],s);

  pind1 = interp1(polyval(p,[-500;2000]),[-500;2000],vals1(:,i)-
meanzero(i));
  pind2 = interp1(polyval(p,[-500;2000]),[-500;2000],vals2(:,i)-
meanzero(i));
  %pind1 = 1/p(1)*(vals1(:,i)-meanzero(i));
  %pind2 = 1/p(1)*(vals2(:,i)-meanzero(i));

  %pind1 = interp1(cal6(idx([1 4]),i),pvec1([1 4]),vals1(idx,i));
  %pind2 = interp1(cal6(idx([1 4]),i),pvec1([1 4]),vals2(:,i));
  %pind2up = interp1(cal6(idx([1 4]),i),pvec1([1 4]),valsup(:,i));
  %pind2dn = interp1(cal6(idx([1 4]),i),pvec1([1 4]),valsdn(:,i));

  if 1
  plot([pvec1;pvec2],[pind1;pind2]-[pvec1;pvec2],'+-')
  %hold on
  %plot(pvec2,pind2-pvec2,'x-')
  xaxis([0 1700])
  yaxis([-20 20])
  hline(0,':')
  else
  plot([0;max(pvec)],plotvals,':')
  hold on
  plot([0;max(pvec)],[0 max(pvec)*p(1)],'--')
  plot(pvec1,vals1(:,i)-meanzero(i),'+')
  plot(pvec2,vals2(:,i)-meanzero(i),'x')
  axis([0 500 -.1 .5])
  end
  hold off
  ylabel(['Indicated-Ref. Pres. [psi]'])
  xlabel('Reference Pressure [psig]')
  mfrac = (1/p(1) - oldms(i))/oldms(i);
  tstr = sprintf('Sensor %d (%s); sf=%2.2f
(%1.1f%%)',i,names{i},1/p(1),mfrac*100);
  title(tstr)
  kul(i).p = p;
  kul(i).pvec=pvec;
  kul(i).delt=delt;
end
kulp = cat(1,kul.p);
ms2 = 1./kulp(:,1);
```

## H.2 ZONE LENGTH CORRELATION

This code creates correlations between analytical results and empirical data for zone length calculations

```
kul = [];

readerr = 10;

[cal51,date51] = loadcal(51);
cal51 = cal51(77:end,:);
cidx = find(diffnext(cal51(:,11)) ~= 0);
vals1 = cal51(cidx,1:10);
pvec1 = cal51(cidx+1,11);

[cal52,date52] = loadcal(52);
cal51 = cal52(1:end,:);
cidx = find(diffnext(cal52(:,11)) ~= 0);
vals2 = cal52(cidx,1:10);
pvec2 = cal52(cidx+1,11);

pvec = [pvec1 ; pvec2];
vals = [vals1 ; vals2];

zidx = 125:216;

figure(2)
for i = 1:8
  meanzero(i) = mean(cal52(zidx,i));
  kul(i).dat = [vals(:,i)] %-meanzero(i)];
  %[p,s] = polyfit([pvec;15],[kul(i).dat;0],1); %first order, linear fit..
  [p,s] = polyfit([pvec],[kul(i).dat],1); %first order, linear fit..

  if i > 4
    figure(2)
    orient landscape
    subplot(2,2,i-4)
  else
    figure(1)
    orient landscape
    subplot(2,2,i)
 end
  [plotvals,delt] = polyval(p,[0;max(pvec)],s);
  plot([0;max(pvec)],plotvals,':')
  hold on
  plot(pvec1,vals1(:,i),'bx')
  plot([pvec1-readerr pvec1+readerr]',vals1(:,[i i])','b-')
  %plot(pvec1+10,vals1(:,i),'.')
  plot(pvec2,vals2(:,i),'gx')
```

```
  plot([pvec2-readerr pvec2+readerr]',vals2(:,[i i])','g-')

  hold off
  ylabel(['Sensor ' n2s(i) ' (\Delta: ' n2s(p(2)/p(1)) 'psi)'])
  title(['Vo = ' n2s(p(2)) 'V; m = ' n2s(1/p(1)) 'psi/V'])
  kul(i).p = p;
  kul(i).pvec=pvec;
  axis([0 1700 -0.2 1.4])
end
```

# REFERENCES


[1] London, A.P. *Development and Test of a Microfabricated Bipropellant Rocket Engine.* Ph.D. Thesis. Massachusetts Institute of Technology. 2000.

[2] Brennan, C.E. *Cavitation and Bubble Dynamics.* Pasadena, CA: Oxford University Press, 1995.

[3] Knapp, R.T., Daily, J.W., and Hammitt, F.G. *Cavitation.* New York: McGraw-Hill Book Company, 1970.

[4] Grist, Edward. *Cavitation and the Centrifugal Pump: A Guide for Pump Users.*Philadelphia, PA: Taylor & Francis, 1999.

[5] Young, F. Ronald. *Cavitation.* New York: McGraw-Hill Book Company, 1989.

[6] Fréchette, L.G. *Development of a Microfabricated Silicon Motor-Driven Compression System.* Ph.D. Thesis. Massachusetts Institute of Technology. 2000.

[7] Protz, C.S. *Systems Analysis of a Microfabricated Storable Bipropellant Rocket Engine.* S.M. Thesis. Massachusetts Institute of Technology. 2000.

[8] Kerrebrock, J.L. *Aircraft Engines and Gas Turbines*, 2nd Ed.. Cambridge, MA: The MIT Press, 1992.

[9] London, A.P. Personal Communications. 2000

[10] Styen, L. Personal Communications. 2000.

[11] Ayon, A. Personal Communications. 2000.

[12] Epstein, A.H. Personal Communications. 2000.

[13] London, A.P. *A Systems Study of Propulsion Technologies for Orbit Attitude Control of Microspacecraft.* M.S. Thesis. Massachusetts Institute of Technology. 1996.

[14] Francis, R.J. *A Systems Study of Very Small Launch Vehicles.* M.S. Thesis. Massachusetts Institute of Technology, 1999.

[15] Al-Midani, O.M. *Preliminary Deisgn of a Liquid Bipropellant Microfabricated Rocket Engine.* M.S. Thesis. Massachusetts Institute of Technology. 1998.

[16] Holl, William J. and Trester, A.L. "Cavitation Hysteresis." *Journal of Basic Engineering,* Vol. 88 No. 1, p.199-210, March 1966.

[17] Hammitt, Frederick G. *Cavitation and Multi-Phase Plow Phenomenon.* New York: McGraw Hill, 1980.

[18] Holl, William J. and Trester, A.L. "Scale Effects on Cavitation." *Journal of Basic Engineering,* Vol. 83 No. 3, p.385-394, Spet. 1961.

[19] Drela, M and H. Youngren. *A user guide to MISES 2.3*, December 1995, Massachusetts Institute of Technology, Computational Aerospace Sciences Library.

[20] Campbell, Stephen A. *The Science and Engineering of Microelectronic Fabrication.* New York: Oxford University Press, 1996.

[21] Morel, Thomas. "Design of Two-Dimensional Wind Tunnel Contractions." *Journal of Fluids Engineeing*, Vol. 99, No. 2,p.371-377, June 1977.

[22] Senoo, Y, and Nishi, M. "Prediction of Flow Separation in a Diffuser by a Boundary Layer Calculation." *Journal of Fluids Engineering*, Vol. 99, No. 2, p.379-389, June 1977.

[23] Peles, Yoav, Personal Communication, 2000-2001

[24] Youngren, H.H. "Analysis and Design of Transonic Cascades with Splitter Vanes. Report 203, MIT Gas Turbine Laboratory, Cambridge , MA, 1991.

[25] Youngren, H.H. and Drela, M. "Viscous/Inviscid Method for Preliminary Design of Transonic Cascades. AIAA-91-2364, 1991.

[26] White, Frank M. *Viscous Fluid Flow.* Boston: McGraw Hill and Company, 1991

[27] Deux, A, and Jamonet, L, Personal Communications, 2001.

[28] Plesset, M.S. "The Dynamics of Cavitation Bubbles" *Tran. ASME, Jr. Appl. Mech,* **16**, 96-98, 1954.

[29] Poritsky, H.: "The Collapse or Growth of a Spherical Bubble or Cavity in a Viscous Fluid," *Proc. First U.S. Natl. Congress Applied Mechanics. (ASME),*pp. 813-821, 1952.

[30] MATLAB handbook

[31] Personal communication with Mark Drela, 2000

[32] Deux, A. Personal Communication re M.S. thesis in progress. Massachusetts Institute of Technology, 2000-2001.

[33] Jian, Chen-Wen. *Experimental and Theoretical Investigation of Unsteady Supercavitating Hydrofoils of Finite Span.* Ph.D. Thesis. Massachusetts Institute of Technology. 1977.

[34] Sayre, Harold Clayton. *Experimental Determination of the Effect of Cavity Gas Content on the Performance of Cavitating Hydrofoils.* M.S. Thesis. Massachusetts Institute of Technology. 1981.

[35] Marbose, Richard C. *Bubble Dynamics and Resulting Noise from Traveling Bubble Cavitation.* M.S. Thesis. Massachusetts Institute of Technology. 1982.

[36] Golden, Daniel Wilson. *A Numerical Method for Two-Dimensional, Cavitating, Lifting Flows.* M.S. Thesis. Massachusetts Institute of Technology. 1975.